Trinity 2013

– ℋ –

A thesis submitted in partial fulfilment *of*
the requirements for the degree *of*
Doctor *of* Philosophy

Visible Light Communications using Optical OFDM

Ahmad Helmi Azhar

Balliol College

Department *of* Engineering Science

University *of* Oxford

Trinity 2013

–ℋ–

A thesis submitted in partial fulfilment *of*
the requirements for the degree *of*
Doctor *of* Philosophy

Visible Light Communications using Optical OFDM

Ahmad Helmi Azhar
Balliol College
Trinity 2013

A thesis submitted in partial fulfilment *of*
the requirements for the degree *of*
Doctor *of* Philosophy

Abstract

This thesis presents an investigation into designs and developments of indoor visible light communication (VLC) systems using orthogonal frequency division multiplexing (OFDM) schemes. The novel contribution of this thesis is a development of a visible light communication system that incorporates OFDM and imaging-diversity multiple-input multiple-output (MIMO) techniques, which allows robust transmissions on multiple channels at high data rates.

The characteristics of VLC systems are presented, one of which is VLC communications channel exhibits high Signal-to-Noise Ratio (SNR). The major constraint however, is the low modulation bandwidth of typical high power white LED sources.

The performance of OFDM as a modulation scheme is investigated. OFDM offers the possibility for bit and power loading to increase bandwidth efficiency, as well as a straightforward equalisation in time and frequency domains to compensate the low pass frequency response of the LED. This allows transmission rates of up to ~310Mbps at a BER of $2x10^{-3}$ on a single-channel link using 16-QAM DCO-OFDM. Further increase in data rates for this transmission is constrained by the available signal power due to a dynamic range limitation at the receiver. An increase in signal power will results in the OFDM waveform to be clipped, which incurs a clipping noise.

MIMO systems offer a linear capacity gain to a number of transmission channels in an ideal configuration. These systems mitigate the dynamic range limitation, as power is divided between multiple channels. The performance of a MIMO transmission system is investigated under the same dynamic range constraint. A 4-channel MIMO transmitter is built using four sets of transmitter components of the single-channel link. An imaging system is used to separate the received optical power onto multiple detectors, and MIMO processing relaxes the requirements for precise mechanical alignments. The experiment has shown that the imaging MIMO system further improves data rates and transmissions of up to ~1.1Gigabit/s at a BER of $2x10^{-3}$ are achieved. To the best of the author's knowledge, this is the highest reported for an indoor VLC MIMO-OFDM transmission. Also presented is an analysis of MIMO system scalability to provide room-wide coverage.

Finally, this thesis presents an extended analysis of several other optical OFDM approaches, and concludes with recommendations of future work to increase the data rates of indoor VLC systems.

This page is intentionally left blank.

Acknowledgements

I acknowledge with gratitude, my debt of thanks to **Professor Dominic O'Brien** for his supervision of my work, as well as his invaluable insight, utmost patience and relentless support for the completion of this thesis.

I would like to extend my best regards to **Grahame Faulkner** for his kind assistance and advice.

I thank members of the Oxford University Communications Research Group**,** namely **Tran Tuan-Anh, Hyunchae Chun, Dr Sujan Rajbhandari,** and **Dr Jin Xianqing.** I thank friend**s** from the University of Cambridge, especially **Nurjuanis Zara Zainuddin**, and **Benedikt von Lindeiner** for their assistance in proof-reading this thesis. Not to forget the ever-reliable **Boon Chia Weng.**

To **Rowena Abdul Razak,** thank you for being there throughout my viva.

Most importantly, I owe my deepest gratitude to my family, especially to my parents **Ir. Azhar Ali** and **Hamidah Omar** for their unconditional love and never-ending support. A special word of love goes to my sister **Siti Najihah Azhar**, and brothers **Muhammad Hisham Azhar** and **Ahmad Ismail Azhar,** for their support and constancy.

The scholarship for this work has been provided by **Biasiswa Yang di-Pertuan Agong Malaysia.**

This thesis is dedicated to my grandparents **Zaleha Zainal, Mohd Ali Noh, Mahani Siraj,** and **Omar Saim.**

Ahmad Helmi Azhar
Balliol College
Oxford
Trinity 2013

Table of Contents

List of Figures

List of Tables

List of Publications

A. H. Azhar, T. Tuan-Anh, and D. O'Brien, "Demonstration of high-speed data transmission using MIMO-OFDM visible light communications", in 2010 IEEE GLOBECOM Workshops (GC Wkshps), 2010, pp. 1052-1056. Digital Object Identifier: 10.1109/GLOCOMW.2010.5700095.

A. H. Azhar, T. Tuan-Anh, and D. O'Brien, "A Gigabit/s Indoor Wireless Transmission Using MIMO-OFDM Visible-Light Communications", in IEEE Photonic Technology Letters, Volume: 25 - Issue: 2, 2010, pp. 171-174. Digital Object Identifier: 10.1109/LPT.2012.2231857.

A. H. Azhar and D. O'Brien, " Experimental Comparisons of Optical OFDM Approaches in Visible Light Communications", in 2013 IEEE GLOBECOM Workshops (GC Wkshps), 2013 (reviewed and accepted for publication).

List of Abbreviations

SSL	Solid-state lighting
LED	Light emitting diode
VLC	Visible light communications
OW	Optical wireless
IR	Infra-red
RF	Radio frequency
RGB	Red green blue (colour)
OLED	Organic LED
IM/DD	Intensity modulation / Direct detection
FOV	Field of view
IEEE	Institute of Electrical and Electronic Engineering
Li-fi	Light Fidelity
PWM	Pulse-width modulation
SNR	Signal-to-noise ratio
MIMO	Multi-input multi-output
BER	Bit-error rate
EOE	Electrical-optical-electrical
OFDM	Orthogonal frequency division multiplexing

This page is intentionally left blank.

Chapter 1

Indoor Visible Light Communications

1.1 Motivation

Solid-state lighting (SSL) systems that use white light emitting diodes (LEDs) are predicted to progressively replace the legacy/conventional lighting installations (such as the incandescent or fluorescent lighting). This is due to their energy efficiency, long operating lifetime, and low manufacturing cost [1]. In addition to the low energy consumption, LEDs have relatively fast response times compared with traditional alternatives, allowing high switching rates that are imperceptible to the human eye. This offers the potential for high-speed data transmission and illumination using the visible light channel.

Visible light communications (VLC) is defined as communication using the visible light region of the optical spectrum in the frequency range of 750THz to 428THz (~400nm to 700nm wavelength) as a medium for data transmission [1]. The main property of VLC that is distinctive from other optical wireless (OW) systems such as infra-red (IR) communications, is its ability to provide illumination as well as communication.

In recent years, demands for wireless communication bandwidth have increased dramatically due to the way people communicate and socialise using mobile devices. The radio frequency (RF) spectrum is becoming more congested, highly regulated, and expensive to license [2]. Based on current spectrum allocations, spectrum availability will soon face a shortage as the demand for data

spectrum is projected to overtake advances in spectral efficiency [3]. As an alternative, OW systems such as VLC use the optical spectrum. This presents a potential solution for the radio frequency spectrum shortage.

The optical spectrum offers a bandwidth that many orders of magnitude higher than the bandwidth of the RF spectrum. The optical channel is localised and contained in a room/enclosed area as the optical beam does not penetrate walls. This provides a higher degree of privacy and security against eavesdropping than RF alternatives. In addition to privacy and security, this feature prevents interference between links operating in different rooms [4].

Furthermore, optical communications permit operations in areas where establishing RF communications is difficult. For example, the optical channel is robust against electro-magnetic interference. This allows application in environments with congested RF-based systems and in an environment where radio-frequency is discouraged such as operations in the area of aircraft cabin, hospitals and establishing underwater/deep-sea communications [5].

VLC systems have lenient eye safety regulations, compared with IR systems. This is because the visible light LED creates a divergent pattern from an extended source, compared with typical IR point sources [6, 7]. In addition, the visibility in VLC allows natural aversion responses such as the blink reflex and pupil contraction to prevent eye damage.

1.2 Indoor VLC system overview

An indoor visible light communication system consists of a transmitter, a propagation channel, and a receiver. A VLC link may operate in two main configurations; a line-of-sight (LOS) link or a diffuse

link. Figure 1 shows two types of VLC configurations. Extensive work has been conducted in characterising the VLC channel [8-10].

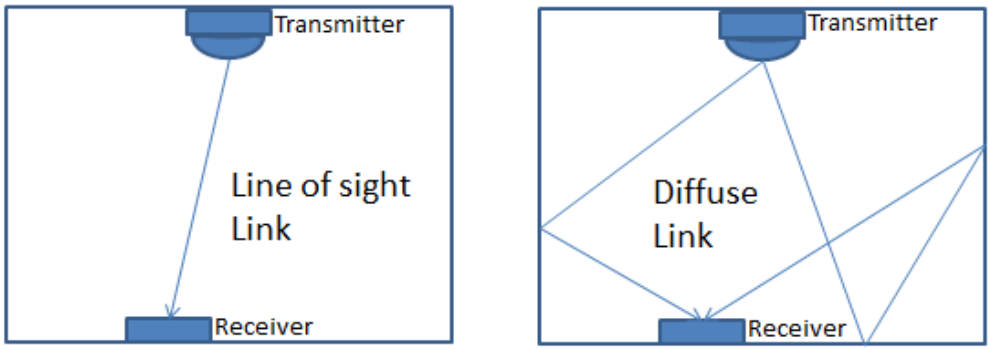

Figure 1. VLC link configurations in an indoor environment.

Information transmitted in the diffuse link relies on the diffuse reflectivity of walls and surfaces in the indoor environment to provide coverage that is robust to shadowing/blockage. However, the various possible paths have different propagation distances, leading to multipath dispersion. In addition, the available signal power is greatly reduced due to the reflection losses at walls and other surfaces [11].

LOS links are typically robust to multipath dispersion and reflective losses. However, this configuration is susceptible to the effect of shadowing or blockage. In a general VLC system configuration, multiple transmitters incorporating indoor lighting infrastructures are typically used to meet indoor illumination requirements. This alleviates shadowing and offers a wide field-of-view (FOV) to provide broad area coverage [8, 12].

1.2.1 Transmitter

Early work on indoor VLC systems was driven by the availability of highly efficient InGaN-based blue-phosphor LEDs. These consist of a blue emitter (blue LED chip) that excites a phosphor

coating. This coating emits a yellow light, which mixes with the blue LED emission to produce white light. This offers a simple and low cost transmitter for indoor VLC systems [7-9, 12].

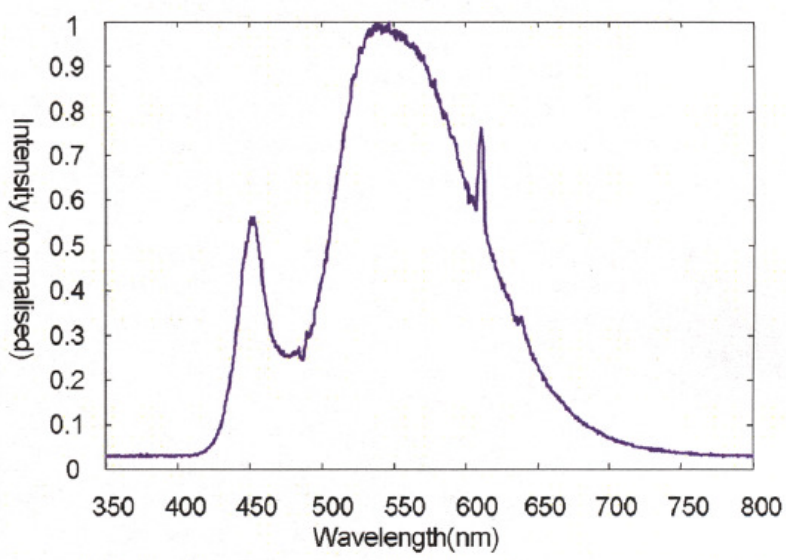

Figure 2. Emission spectrum distribution of a blue-phosphor LED [12].

Figure 2 shows the measured emission spectral power distribution for a blue-phosphor LED (Luxeon Star-C [13]) taken from the datasheet. It can be seen from Figure 2 that the primary component from the blue emitter peaks at ~450nm and a secondary phosphorescence spectrum has a shifted peak at ~550nm. In comparison with emitters capable of high-speed modulation, the blue-phosphor LED has a very large surface emitting area, and thus exhibits high capacitance. This limits the modulation bandwidth of the blue emission. In addition, the secondary phosphorescence component has a long decay time as compared to the primary blue component, which further limits the overall bandwidth of the white emission output [14]. Several bandwidth measurements conducted show that a conventional single chip blue-phosphor LED has a typical white emission bandwidth of ~2MHz [8, 12, 15].

It is also possible to use Red-Green-Blue (RGB) LEDs to generate white light. An RGB LED consists of three red, green, and blue emitters closely placed in a single package, and emission from all three is combined to form white light [9, 16]. Figure 3 shows the emission spectrum of a typical RGB LED.

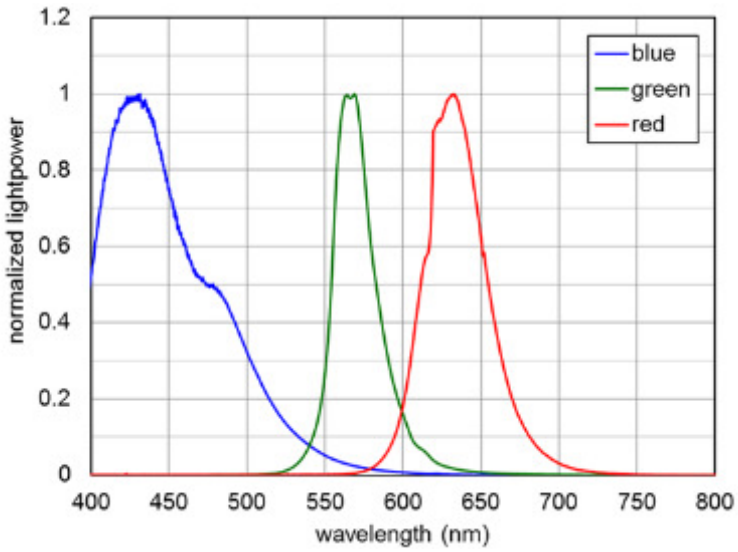

Figure 3. Emission spectrum of a typical RGB LED [17].

The RGB LED offers the possibility for wavelength-division multiplexing (WDM), in which each wavelength (colour) carries independent data in a single transmission. However, this introduces complexity in the infrastructure design and a need for colour balancing [12, 18].

Organic LEDs (OLEDs) have attracted the attention of the VLC research community as a potential transmitter due to its flexible, flat and large emitting surface area. However, at present the modulation bandwidth of OLEDs is much lower than a normal LED. Typically, bandwidths of ~0.1MHz have been measured [19-21].

1.2.2 Propagation channel

In a practical VLC configuration, multiple LED sources are used to provide the required illumination level for typical room coverage. An illumination level of 400-1000*lux* is considered acceptable for typical work environments [22].

Several models of the optical channel and illumination layout have been developed [8, 23-25], and work conducted in [8] and [23] suggest that a very high signal-to-noise ratio (SNR) of up to and more than 60dB is available at the required illumination level. The channel response obtained, combining both responses from LOS and diffuse paths has a bandwidth in the range of ~100MHz in a typical room [8, 23].

VLC systems use a non-coherent intensity modulated direct detection (IM/DD) scheme, which detects the spatially-averaged time-varying intensity of the transmitted optical signal. This removes any phase components, as well as fading and multipath interference as the detector is unable to respond to the frequency of the optical carrier.

1.2.3 Receiver

A basic IM/DD receiver consists of an optical concentrator, a photo-detector and a signal amplifier. The optical concentrator is used to increase the effective collection area of the photo-detector. This is to maximise the power received on the photo-detector surface [4]. The photo-detector generates photo-current from the received optical signal, which is then passed to the amplifier for signal amplification. The photo-detector used in optical wireless communications is typically a positive-intrinsic-negative (p-i-n) silicon photodiode due to its low-cost and low-capacitance [4]. Typical

receivers used in VLC systems have a bandwidth of 40MHz to 90MHz, and collection areas of order $1cm^2$ [26-28].

A more complex receiver configuration that is possibly used in VLC systems is where multi-element photo-detectors are used to detect signals from a single or multiple sources. An example of such a configuration is an angle-diversity receiver. This has multiple detectors, each of which is fitted with its own concentrator [29]. This gives the receiver a wider FOV whilst maintaining a large collection area.

Another example of a multi-detector receiver is an imaging-diversity receiver [30]. The detectors share a single imaging lens that focuses the received light from multiple sources onto multiple detector cells, which can be detected separately. Imaging-diversity receivers have the advantage of a smaller receiver size compared with angle-diversity designs, as detectors can be arranged in a planar grid, and there is no need for a concentrator on each detector.

Figure 4 shows several types of VLC receiver configurations. Figure 4(a) shows a basic single-element receiver, Figure 4(b) shows the angle diversity receiver [4, 29] and Figure 4(c) shows the imaging receiver [4, 30, 31].

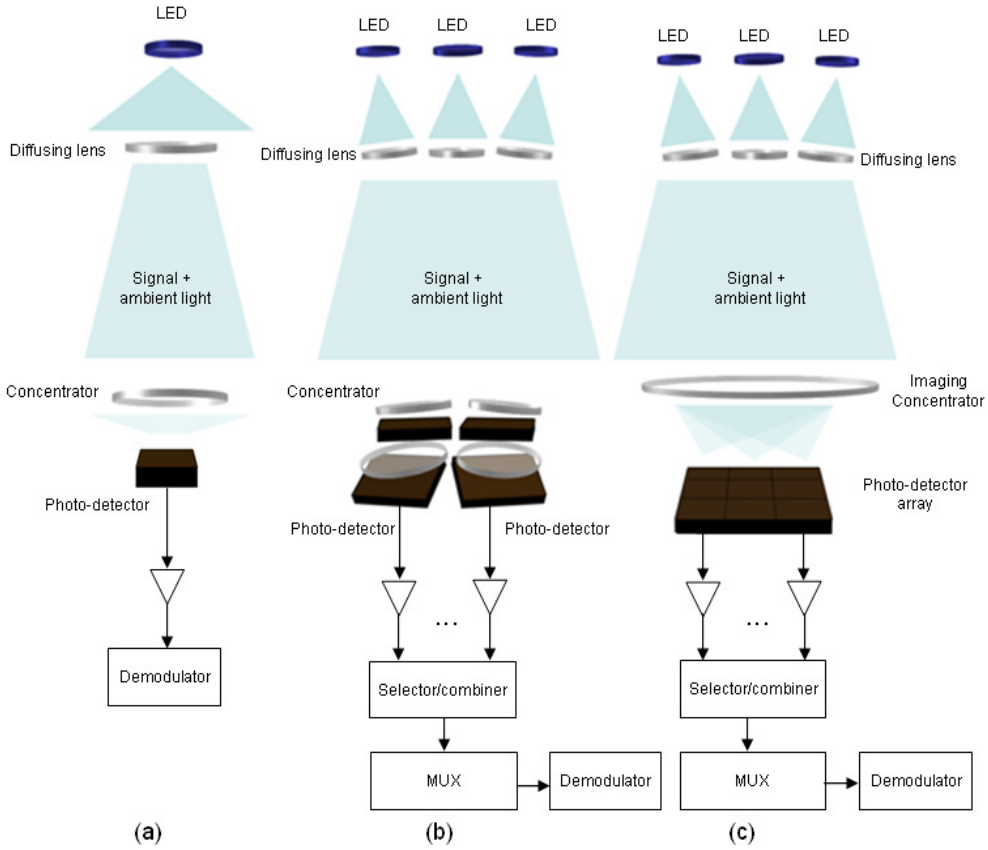

Figure 4. Several potential receiver configurations: (a) Single-detector receiver (b) Angle-diversity receiver (c) Imaging-diversity receiver.

1.2.4 Industry standards and other applications

The Visible Light Communications Consortium (VLCC) was established in Japan in 2003, pioneering work related to commercial and standardisation issues of VLC [32]. The Wireless World Research Forum advanced the interest in the field by providing future research directions among industry and academia [33]. The development of services and protocols within standards by the Institute of Electrical and Electronics Engineers (IEEE) is structured by the formation of Task group 7 (IG-VLC) under the 15th working group of the IEEE 802 (IEEE 802.15.7) [34]. More recently, indoor visible light communication systems have adopted the term Li-Fi, as a label for

wireless systems using light instead of radio frequency [35]. The Li-Fi Consortium has been established as an interest group to promote developments of Li-Fi technology [36]. Apart from wireless indoor applications, there are many other applications of VLC currently under investigation, such as communications in Intelligent Transport Systems, Indoor positioning, and Visible Light ID [1, 7, 12].

1.3 Research challenges

The main objective of this research is to increase data rates for indoor wireless communications using VLC. The current technology for indoor wireless RF using the IEEE 802.11n standard provides theoretical transmission bit-rates of up to 600Mbps [37], and the forthcoming generation IEEE 802.11ac standard provides theoretical indoor transmission bit-rates of up to 1.3Gbps [38]. Theoretical modeling has demonstrated the possibility for VLC transmission of more than gigabit/s bit-rates under room illumination requirements. However, practical implementations of a high speed VLC transmission are mainly constrained by low bandwidth of LED devices. Several methods have been introduced to achieve this, and these are discussed in Section 1.4.

Apart from increasing the transmission bit-rates of VLC systems, there are other challenges faced by the VLC research community and some are described here in brief. Preliminary reviews on other technical challenges of the indoor VLC system have been discussed by O'Brien *et al.* [12] and Grubor *et al.* [8].

One such a challenge is the provision of uplink. As VLC utilises the lighting system to provide communication, downlink broadcasting from the lighting terminal to the user is straightforward. On the other hand, the provision of an uplink from the user back to the lighting terminal requires

another transmission system from the user back to the lighting terminal. The data rate requirements for this link however, can be relatively lower than the downlink, thus several low-rate communication methods have been demonstrated. Novel uplink systems such as an IR uplink [12, 39] and a retro-reflecting link [12, 39] have been proposed as a potential solution. The retro-reflecting link returns a portion of the transmitted light back to the terminal, carrying uplink information modulated at the users end. Another viable solution is to integrate VLC with an existing RF platform, thus using the VLC channel for downlink and RF channel for uplink [39]. This reduces the load on the shared RF channel thus increasing overall transmission performance.

Another challenge is the ability to provide dimming or brightness control [40, 41]. The brightness level can be controlled in two ways. First, since brightness is proportional to the dc-bias current of the LED, a straightforward way is by adjusting the dc-bias current of the LED [42]. Secondly, the brightness level can be controlled using pulse-width modulation (PWM), in which case the dc-bias current is kept constant and dimming is performed by adjusting the duty-cycle *i.e.* the width of the signal pulse [43, 44]. PWM offers a wide dimming range and a linear relationship between the light output and the duty cycle, making it a preferred solution [42]. However, both methods results in a change in the emitted light colour, the so called chromaticity shift problem [45]. The PWM method is more robust to chromaticity shift than the LED dc-bias current method, and this effect is more severe in RGB LED than blue-phosphor LED systems.

1.4 Improving data rates

The bandwidth of a VLC communications system is a function of the transmitter, receiver and the optical channel bandwidth. The receiver and optical channel have a relatively higher bandwidth than

the transmitter; therefore the end-to-end VLC electrical-optical-electrical (EOE) channel is limited by the low bandwidth of the LED. Nevertheless, the VLC channel exhibits high SNR at the required indoor illumination level. The VLC channel can therefore be characterised as a high-SNR and bandwidth-limited channel.

A straightforward method to increase LED bandwidth is to use a blue transmission filter at the receiver to block the slow phosphor component. Bandwidth measurements of a blue-phosphor LED reported in [22] show that using a blue transmission filter increases the bandwidth from ~2MHz to ~20MHz. However, blocking the phosphor component results in a penalty of a reduction in the overall received signal power.

Several other methods have been introduced to use the SNR advantage to overcome bandwidth limitations of the LED. These include: analogue equalisation, higher-order modulation and multi-input multi-output (MIMO) transmission. These methods are discussed in the following sections.

1.4.1 Analogue equalisation

Analogue equalisation techniques can be implemented at the transmitter or receiver front-end. A post-equalisation method using a simple first order low-pass filter at the receiver was used to increase transmission bit-rates from 40Mbps to 100Mbps at a BER of $1x10^{-9}$ [28].

Work demonstrated in [26] shows that it is possible to use a pre-amplifier circuit at the transmitter to increase the bandwidth of a blue-phosphor LED up to ~30MHz, at the cost of a reduction in the modulation depth *i.e.* the ratio of signal power over the overall transmitted optical power. This demonstration achieved transmission bit-rates of up to 513Mbps using OFDM.

A transmitter using a multiple resonance pre-equalisation technique has demonstrated a bandwidth of up to ~25MHz [27]. This transmitter uses multiple LEDs that are closely arranged together in an array and each is driven to resonate at a particular frequency thus allowing the overall bandwidth of the transmitter to be increased.

The key advantage of analogue equalisation schemes is its simplicity. It is suited to modulation schemes that do not require digital signal processing, such as on-off keying. For systems with more complex signal processing, equalisation can be incorporated as part of the signal processing scheme, and analogue equaliser is often unnecessary.

1.4.2 Higher-order modulation

The VLC channel exhibits a high-SNR and low-bandwidth characteristics. Because of this, high spectral efficiency modulation formats are suitable candidates for applications in VLC systems. For single-carrier formats, VLC transmission using pulse amplitude modulation (*M*-PAM) [46] and carrier-less amplitude and phase (*M*-CAP) [47] schemes have been demonstrated. However, to counteract the effect of low channel bandwidth, simulations conducted in [46] show that the complexity required to implement time-domain equalisation filter in single-carrier schemes increases rapidly as data rates increases.

Multi-carrier modulation schemes offer several advantages over single-carrier modulation schemes. One such advantage, multi-carrier schemes typically offer the possibility to perform equalisation both in the time and frequency domains [48]. This allows the response of a communication channel to be compensated in a straightforward way. In addition to this, bit-loading approach by transmitting more bits in a frequency band that has a higher SNR, improves the spectral efficiency of multi-

carrier schemes [49]. Multi-carrier schemes are used extensively in RF-based wireless systems due to their inherent robustness to inter-symbol interference (ISI), caused by channel dispersion [50].

One such multi-carrier scheme, orthogonal frequency-division multiplexing (OFDM) transmits multiple subcarriers that are overlapped with each other orthogonally, by using an inverse fast Fourier transform (IFFT) algorithm [8, 51-54]. This provides a straightforward frequency-selective feature, where each subcarrier at various frequencies can be independently modulated in the digital domain.

With this, OFDM offers the possibility for frequency-domain equalisation that removes the complexity of an analogue equalisation filter. Any phase variation with frequency due to channel characteristics can be corrected in the digital domain with little or no cost [54]. In addition, a frequency-selective bit and power loading approach in OFDM can also be implemented to increase bandwidth efficiency [55, 56].

The frequency-selective characteristic is also suitable for a multiple access system, where users can select a particular signal band in a single multiplex channel [6].

Further to this, OFDM is immune to ISI as compared with the single-carrier alternative. This ISI may exist in the VLC channel due to multi-path propagations from multiple LED sources. This is because the period for each frame can be made longer than the channel delay spread [54]. In addition, a form of guard interval, termed the cyclic-prefix, can be added to the OFDM waveform to further mitigate multipath delays.

Practical considerations for indoor OFDM systems are discussed in [53]. While OFDM offers many advantages for indoor VLC systems, it has a number of disadvantages. OFDM requires a large linear

operational dynamic range, because the signal exhibits a Gaussian distribution with a high peak-to-average power ratio (PAPR). Due to the high PAPR, a system with a limited linear dynamic range results in clipping of the peak amplitudes of the OFDM signal, which introduces additional clipping noise [57]. For applications in VLC systems, the typically nonlinear LED electrical-optical response must be taken into consideration [58]. Several methods to overcome this have been considered, such as systematic clipping and filtering [26, 59], power back-off to avoid saturation, and a predistorter to compensate for the nonlinear response of the LED [60].

Further to this, the OFDM scheme in general is highly sensitive to frequency and phase offsets from impairments in the channel, for instance, phase noise which may arise from analogue-to-digital converter (ADC) as a function of signalling frequency at the receiver [53].

OFDM has found numerous applications in VLC systems [8, 51-54]. State-of-the-art VLC systems using OFDM have recently demonstrated transmission bit-rates of up to 1Gbps on a single-input single-output (SISO) system using a blue-phosphor LED transmitter [61] and bit-rates of up to 3Gbps is achieved on another system using a single Gallium Nitride micro-LED [62]. A VLC transmission using an RGB LED demonstrated data rates up to 3.4Gbps using the OFDM scheme, and these data transmission bit-rates are the highest achieved in VLC systems [63].

Several optical wireless approaches to OFDM have been developed for the application in VLC systems, and these will be introduced in the next section.

1.4.3 Optical OFDM approaches

In IM/DD communications systems, data is carried on the intensity of the transmitted optical signal. This requires a signal that is real and positive (unipolar). However, conventional RF-based OFDM generation produces a signal that is complex and bipolar.

To achieve a real output of the IFFT, an optical OFDM symbol is made up of two parts: the first part consists of a set of active frequency subcarriers, and the second part is a Hermitian copy of the first. The Hermitian copy ensures time-domain output signals of the IFFT are always real, although each data subcarrier may carry a complex data symbol [54].

To ensure a unipolar signal, a straightforward approach is to add a dc-bias current to the signal to make it positive. This is known as the dc-offset optical OFDM (DCO-OFDM) scheme. However, the addition of a constant dc-bias current results in a high-power requirement [54]. Nevertheless, for indoor VLC systems that are designed for lighting applications, this power constraint is not very significant as the constant dc-bias current is regardless required to provide a constant level of room illumination.

Several other approaches to offer a power efficient OFDM schemes have been introduced. One approach to achieve a unipolar signal is by clipping the signal at zero, and only the positive real parts are sent for transmission. This is possible because the OFDM signal is generated in such a way that the positive part is an anti-symmetrical copy of the negative part. This scheme is termed asymmetrically clipped optical OFDM (ACO-OFDM) [64].

The ACO-OFDM scheme offers higher power efficiency as compared to DCO-OFDM for a given bit-error rate (BER) and data rate [64]. However, because the odd components are left unloaded, the bandwidth efficiency of the ACO-OFDM is almost half ($\frac{N}{2N-1}$, where N in this case is the number of active ACO-OFDM subcarrier) of the DCO-OFDM counterpart.

Several other power-efficient schemes have been demonstrated: advanced receiver ACO-OFDM [65] and unipolar OFDM [66]. These advanced methods have higher performance compared with the conventional ACO-OFDM scheme according to theoretical studies. The advanced receiver ACO-OFDM design in [65] shows an improvement, by approximately halving the noise variance by using maximum likelihood detection at the receiver. Unipolar OFDM (U-OFDM) [66] transmits the positive and negative halves of the DCO-OFDM signal in two separate parts in series, and uses a similar receiver design as the advanced receiver ACO-OFDM scheme to reduce noise variance.

1.4.4 MIMO transmission

The availability of a large number of independent sources gives rise to the possibility for MIMO transmissions to further increase data rates. This offers either a linear capacity gain with the increase in the number of channels in an ideal crosstalk-free configuration. Figure 5 shows an example of an array of LED sources, showing the potential for MIMO transmitters .

Figure 5. An example of an array of LED sources that is potentially used in VLC systems to provide sufficient illumination for an indoor work environment [67]. This array of LEDs provides independent channels, which can be utilised in MIMO transmission paths.

In an ideal system, these parallel transmissions are independent of one another and free from inter-channel crosstalk. Such a system can be obtained by channel tracking and precise mechanical alignment [68]. In this case, received beams are aligned so that each detector receives only a beam from a specific transmitter. However, for a system with terminal mobility, maintaining such an alignment without inter-channel crosstalk is difficult, and a system with mechanical tracking [68] as a potential solution is complex and costly.

A MIMO system allows a certain level of inter-channel crosstalk, for which the channels are later separated in the electronic domain using MIMO channel matrix inversion or equivalent processing at the receiver [69]. This provides a higher tolerance to misalignments. In a MIMO system, each detector at the receiver may detect signals from multiple transmitters, where inter-channel crosstalk

between transmitter beams exists. This crosstalk between transmitters is recorded for a particular transmitter-receiver configuration, and this is termed the channel matrix.

A linear form of MIMO transmitter-receiver relationship in a noise-free system can be defined as $Y = HX$, where Y is a matrix of received signals, X is a matrix of transmitted signals and H is the channel matrix. With a pre-obtained value of H, multiplying the inverse of H with the received signal Y gives the estimate of the transmitted signal X. For this to be possible, the crosstalk between channels must exist at a level where the channel matrix is maintained at full rank, which is a requirement for matrix inversion to be performed [69]. Advanced MIMO detection techniques such lattice reduction (LR) and iterative method such as V-BLAST use channel-state information to perform pre-coding at the transmitter to improve the overall MIMO performances [70, 71].

In RF MIMO-systems, a full rank matrix is obtained from rich scattering and fading that exists in the channel. In optical wireless systems, such systems normally use a non-coherent IM/DD, which has different characteristics from coherent indoor RF channel.

Several approaches to MIMO optical wireless have been developed, and this will be presented in the following section.

1.4.5 Optical MIMO approaches

In contrast with the RF system, channel diversity from fading or rich scattering is not attainable in IM/DD systems. In the optical case, the spatial-domain is used to create channel diversity.

Several spatial-domain methods have been demonstrated to obtain a full rank channel matrix in the optical wireless channel. Imaging diversity systems as demonstrated in [30] use the optical geometry

for channel decorrelation and spatial diversity systems as demonstrated in [69] decorrelate the channels using various LOS intensities, and a combination of both approaches as demonstrated in [20]. Figure 6 shows a schematic of spatial-domain optical MIMO systems.

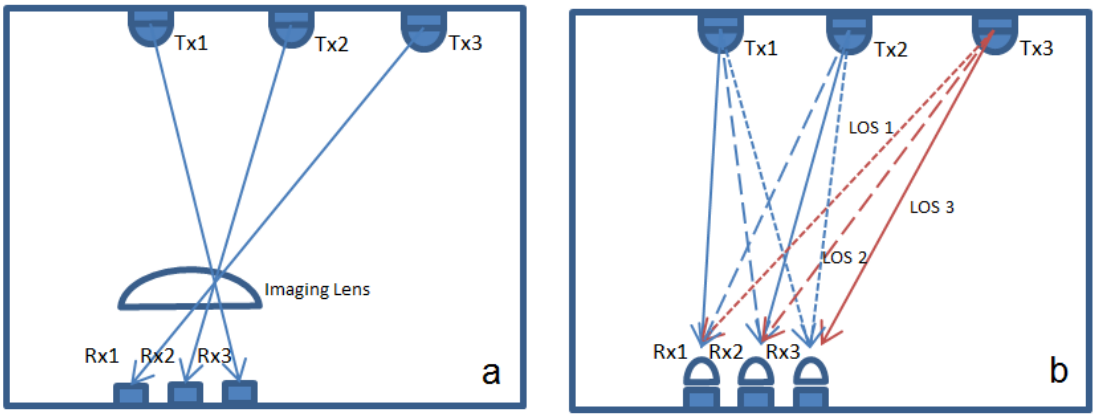

Figure 6. (a) Imaging diversity configurations showing channel diversity/decorrelation is obtained using imaging optics. (b) Spatial diversity configurations showing channel diversity is obtain from various LOS path lengths giving various received intensities at the receiver.

In spatial diversity systems, a full rank matrix is obtained from different intensities received at the receiver because of the difference in LOS propagation paths. A non-imaging multiplexing system in [69] uses this spatial diversity method to decorrelate parallel channels with a known channel matrix at the receiver. The method is constrained by the symmetry in the transmitter-receiver arrangement. This causes the channel matrix to be singular *i.e.* not full rank, hence matrix inversion cannot be performed [8].

Another approach to spatial diversity is demonstrated in [72]. In this method, each transmitter is indexed based on the intensity detected at the receiver. Only one transmitter is active at any given instant, and each transmitter represents a specific binary number. This method can operate with a

minimum of a single detector. However, this method only gives a $|\log2(N)|$ gains compared with a single channel (where N is the number of transmitters).

Imaging diversity systems offer several advantages over spatial-diversity systems. The imaging system is immune to alignment symmetry with a linear capacity gain with the number of channels, that is the minimum of the number of transmitters/receivers used [69]. In this system, beams of multiple transmitters are imaged onto separate detectors at the receiver using an imaging lens. This helps to ensure that the channel matrix is of full rank, and that no two or more beams fall onto the same detector. In this sense, channel decorrelation at the receiver is primarily achieved using the imaging lens and the remaining crosstalk is further decorrelated using MIMO processing.

1.5 Thesis overview

In summary, the primary aim of this research is to address the challenge of increasing data rates for indoor VLC transmission systems. The VLC channel exhibits high SNR, but high data rates is primarily constrained by the low modulation bandwidth of typical white LED sources. A key question that facilitates the investigations reported in this thesis is how to optimise spectral efficiency of the VLC channel bandwidth using the available SNR. The investigations conducted in this thesis are presented as follows:

Chapter 2 presents an investigation into VLC channel characteristics and constraints. Chapter 3 presents an investigation into single-channel OFDM transmissions and the performance of OFDM equalisation modules in improving data rates. Chapter 4 presents an investigation into imaging MIMO method to further improve data rates. Chapter 5 presents an extended investigation into

several OFDM approaches. Finally, Chapter 6 presents thesis conclusions and recommendations on areas of future work to improve data rates.

Based on these investigations conducted, the main contribution of this thesis is a novel imaging MIMO-OFDM system as a solution to improve data rates of VLC systems. This system optimises channel spectral efficiency using the OFDM modulation scheme, and increases the overall channel capacity using the multi-channel MIMO transmission. The imaging MIMO-OFDM system demonstrates transmissions at data rates of up to ~1.1Gbps at a target BER of $2x10^{-3}$. To the author's knowledge, this data rate is the highest reported for an indoor VLC MIMO-OFDM transmission.

Chapter 2

Indoor VLC Channel Characterisation

2.1 Introduction

In order to proceed with investigating methods to improve data rates, characterisation of indoor VLC channels is required. This chapter presents an investigation into the characteristics and constraints of these channels. For this investigation, a VLC electrical-optical-electrical (EOE) channel model is introduced and an experimental indoor VLC system is built. From this approach, basic illumination and communication properties of VLC systems are derived, by means of measurements and calculations.

First, an analysis of the illumination characteristics of VLC systems is presented. In this analysis, the illumination profile of an LED used in this VLC system is measured and characterised. Based on this illumination profile, a simulation of a room-wide VLC configuration is conducted to demonstrate the feasibility of implementing a practical VLC system using this LED to meet room-wide indoor illumination requirements.

An analysis of blue optical transmission filter selection is also presented. The characteristics of typical blue optical transmission filters are specified, and the effect on SNR and bandwidth is investigated. A blue optical transmission filter that gives the best SNR in the system under consideration is then selected.

The final part of this chapter presents an analysis of the dynamic range of VLC systems, which can be a limitation in the high SNR condition presents in typical VLC channels. This section presents the analysis of this limitation for the VLC system in consideration.

2.2 VLC channel model

In this section, the electrical-optical-electrical VLC channel is introduced. The characteristics of the transmitter and receiver are specified and a transmission channel model is presented.

2.2.1 Transmitter electrical-optical response

The electrical signal is converted into an optical intensity using an LED. Figure 7 shows an electrical-optical response plotted as a DC-bias current versus luminous flux in *lumen* of a typical high power LED (Luxeon Star-C LXHL-MW1B) [13]. This LED has been used in several VLC demonstrations [15, 28].

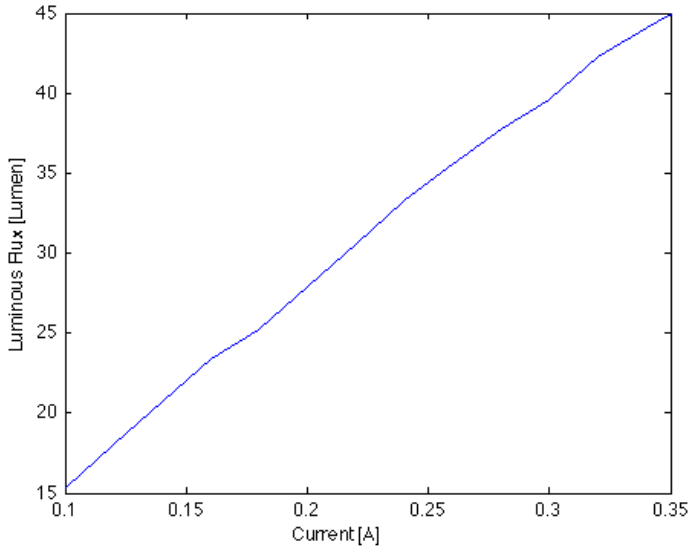

Figure 7. Current versus luminous flux of a typical LED (Luxeon Star-C LXHL-MW1B) for a current range of 0.1A – 0.35A [13].

Communication systems using OFDM require a large linear operational range; therefore it is important to select a signal biasing point within the linear range of the LED response. Studies on LED linearity have been conducted in [58].

The LED transmitted power in the visible light region, P_t is given by

$$P_t = \int_{400nm}^{750nm} P(\lambda) d\lambda \tag{1}$$

where $P(\lambda)$ is the power spectral distribution of the LED in Watts per unit wavelength.

The luminous flux, F in lumen is given by

$$F = \gamma \int_{400nm}^{750nm} V(\lambda) P(\lambda) d\lambda \tag{2}$$

where $V(\lambda)$ is the luminosity function and γ is the maximum luminous efficacy of 683 lm/W for a monochromatic green wavelength at λ= 555nm .

A typical LED package is manufactured for lighting and illumination applications. Most of the manufacturer's datasheets only provide information on LED photometric characteristics rather than radiometric units as required for a link budget. Hence the transmitted power from the LED is calculated using

$$P_t = \xi F \tag{3}$$

where ξ is a conversion parameter (in optical Watts per lumen). The luminous flux F can be calculated using the information obtained from the LED datasheet

$$F = I_v \Omega, \tag{4}$$

$$\Omega = 2\pi(1 - \cos\Phi_{1/2}) \tag{5}$$

where I_v is the luminous intensity in candela, Ω is the solid angle in Steradians and $\Phi_{1/2}$ is the transmitter semi-angle [4]. The conversion parameter ξ is given by

$$\xi = \frac{1}{\gamma \int V(\lambda) P_{1watt}(\lambda) d\lambda} \tag{6}$$

where $P_{1watt}(\lambda)$ is the LED spectral distribution normalised to a total power (optical) of 1 Watt.

2.2.2 Illumination model

Illuminance, E measured in lux, is the level of illumination on a surface, and is an important parameter for indoor lighting systems. A typical room has an average illumination level of 1000*lux*, which is considered suitable for work environments [73].

The illumination level at the receiver plane, E_R is given by

$$E_R = I_v \frac{R_o(\phi)}{d^2} \cos\psi \tag{7}$$

where d is the distance of the receiver from the transmitter, $R_o(\phi)$ is the transmitter radiant intensity profile and ψ is the incident angle at the receiver plane. The LED is assumed to emit a beam with a Lambertian intensity profile, defined as

$$R_o(\phi) = \left[\frac{(m+1)}{2\pi}\right]\cos^m \phi \tag{8}$$

where ϕ is transmitter transmit angle and the Lambertian order m is given by

$$m = \frac{-\ln 2}{\ln(\cos \Phi_{1/2})}. \tag{9}$$

2.2.3 Propagation channel

Indoor optical propagation can take two forms, a direct LOS or diffuse path. The received power P_r is related to the transmitted power by

$$P_r(\lambda) = \sum_{1}^{LED} P_t(\lambda) H(0)_{los} + \int_{walls} P_t(\lambda) dH(0)_{diffuse} \tag{10}$$

where P_t is the transmitted power in the visible light spectrum. $H(0)_{LOS}$ is the DC channel gain of the optical line of sight (LOS) propagation path and $H(0)_{diffuse}$ is the DC channel gain of the diffuse propagation path. The DC channel gain, $H(0)$ is proportional to the average optical power received at the receiver and this is directly related to the illumination level at the receiver plane. The frequency response of the VLC channel is relatively flat near DC, because there is only a single dominant, or a small group of propagation paths.

The channel consists of a number of line of sight paths together with a diffuse channel formed by the light from the source reflecting of multiple surfaces within the room. This characterises the channel impulse response. The DC channel response combining both responses from LOS and diffuse links has a bandwidth in the range of ~100MHz for a typical room [8, 23].

The DC channel gain of the signal for the LOS optical path is described as

$$H(0)_{LOS} = \begin{cases} \frac{A}{d^2} R_o(\phi) T(\lambda,\psi) g(\psi), & 0 \le \varphi \le \varphi_C \\ 0, & \varphi > \varphi_C \end{cases} \quad (11)$$

where A is the effective receiver detection area, $T(\lambda,\psi)$ is the overall transmittance of any optical filter and $g(\psi)$ is the optical concentrator gain at the receiver.

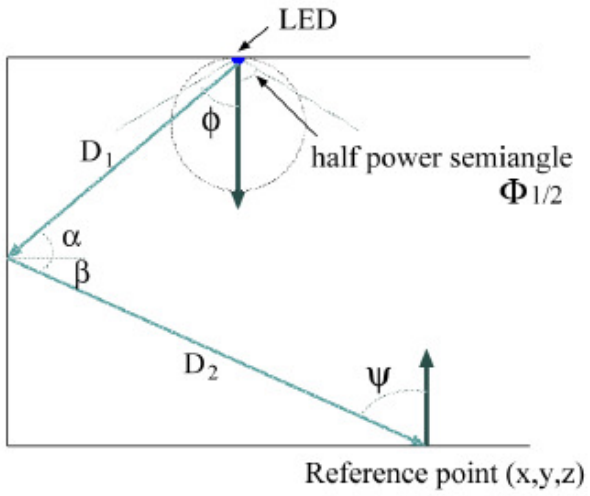

Figure 8. Parameters for diffuse propagation [24].

For a diffuse path, the propagation parameters are shown in Figure 8. The first reflectance of the diffuse path is described as

$$dH(0)_{diffuse} = \begin{cases} \left[\frac{(m+1)}{2\pi^2 D_1^2 D_2^2} A\rho dA_{wall} \right] \cos^m \phi \cos(\alpha) \cos(\beta) T(\lambda,\psi) g(\psi), & 0 \le \varphi \le \varphi_C \\ 0, & \varphi > \varphi_C \end{cases} \quad (12)$$

where ρ is the reflectivity of the wall, dA_{wall} is the area of the reflecting wall surface, α and D_1 are the wall incident angle and path length, and β and D_2 are the wall reflectance angle and the path length respectively.

2.2.4 Ambient light

In a practical VLC configuration, the LED transmitters are typically designed as the main source of room illumination. However, a significant amount of ambient illumination may also present. This may be from existing legacy lighting sources such as incandescent or fluorescent lighting, as well as other devices such as computer and television screens. In addition to this, natural ambient illumination from sunlight may also be present. Figure 9 shows the emission spectra of radiation sources for a typical indoor environment [4].

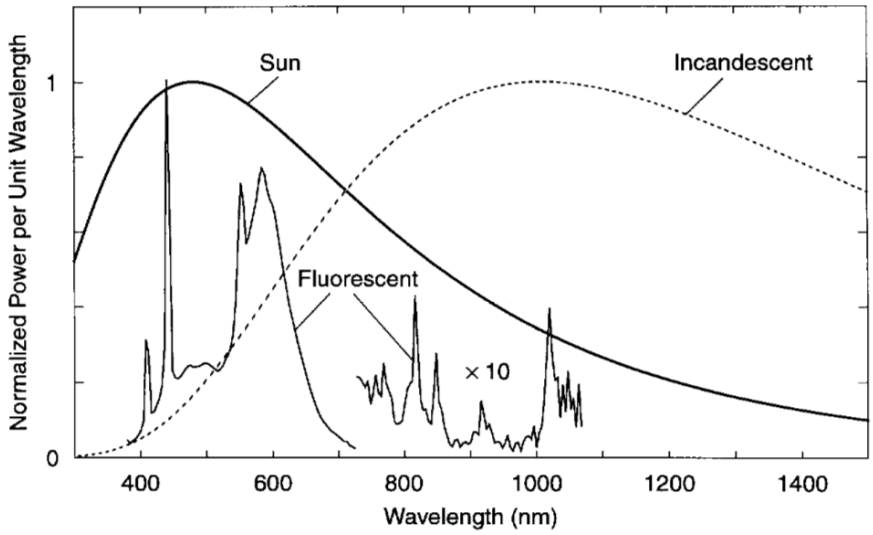

Figure 9. Common radiation sources for a typical indoor environment [4].

The presence of the ambient noise causes unwanted DC/low frequency photocurrent at the receiver. This increases shot noise at the receiver, and the unwanted DC component of the signal may also causes the receiver to saturate. As a solution to this, an optical transmission filter at a receiver is normally used in optical wireless systems to block the unwanted ambient illumination. This will be discussed in the following section.

2.2.5 Receiver model

A typical receiver for optical wireless systems consists of an optical filter, a concentrator and a photo-detector. Figure 10 shows a schematic of a typical receiver.

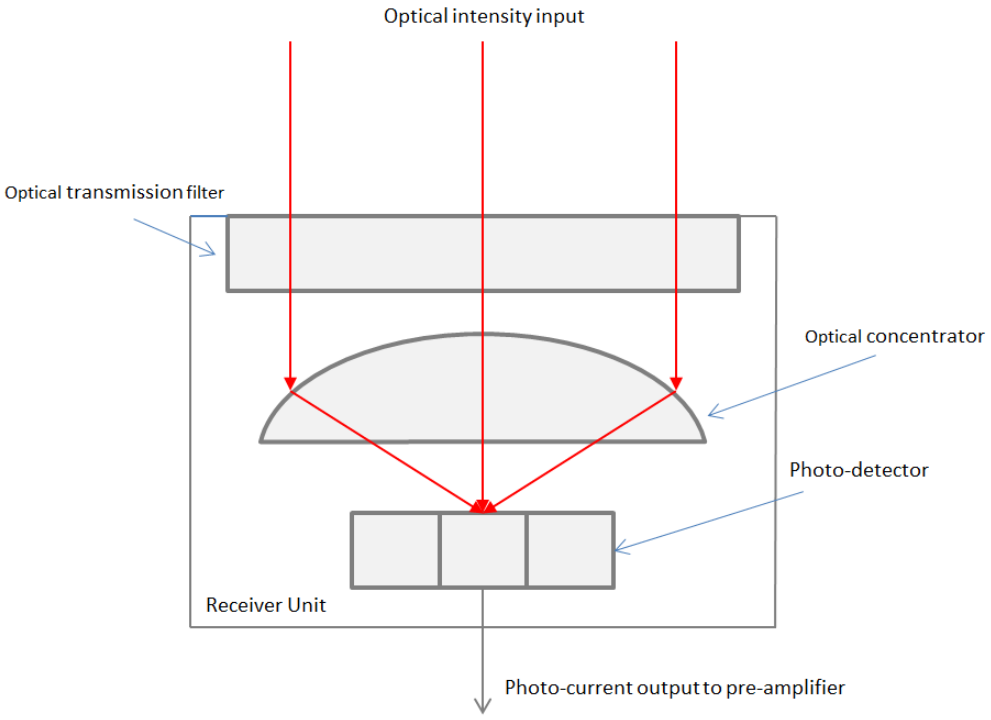

Figure 10. Schematic of a typical receiver.

The optical transmission filter is generally used in optical systems to attenuate unwanted noise from out-of-band ambient light [4]. There are three types of transmission filter that are typically used in

optical wireless channel. High-pass transmission filters pass through spectrum beyond a certain wavelength, are typically used to block the visible light region in IR communications. In the specific case of VLC systems, low-pass or band-pass blue optical transmission filters are typically used. In addition to blocking the unwanted out-of-band spectrum, these filters are also designed to block the secondary phosphorescent component which has a slower response [26, 28]. In comparison with the low-pass filter, the band-pass filter passes through only a narrow spectral bandwidth at the blue peak emission of a blue-phosphor LED. This blocks a higher proportion of the secondary phosphorescent component at the cost of a lower received signal. Details of blue transmission filter selection and different types of filtering cases will be discussed in Section 2.5.

A typical transmission filter response can be fitted to a k-th order Butterworth response

$$T(\lambda,\psi) \approx \frac{T_0(\psi)}{1+\left(\frac{\lambda-\lambda_c(\psi)}{\frac{1}{2}\Delta\lambda}\right)^{2k}} \tag{13}$$

where T_0 is the peak transmittance, λ_c is the filter band centre wavelength, and $\Delta\lambda$ is the Butterworth filter bandwidth [4].

Figure 11 shows an example of a low-pass filter response (Melles-Griot MG520-A [66]) that can be typically used with blue-phosphor LED sources. Also plotted is the response of a 9th-order Butterworth fitting of the transmission filter response showing that there is a good agreement between the two cases. Table 3 shows the filter specifications.

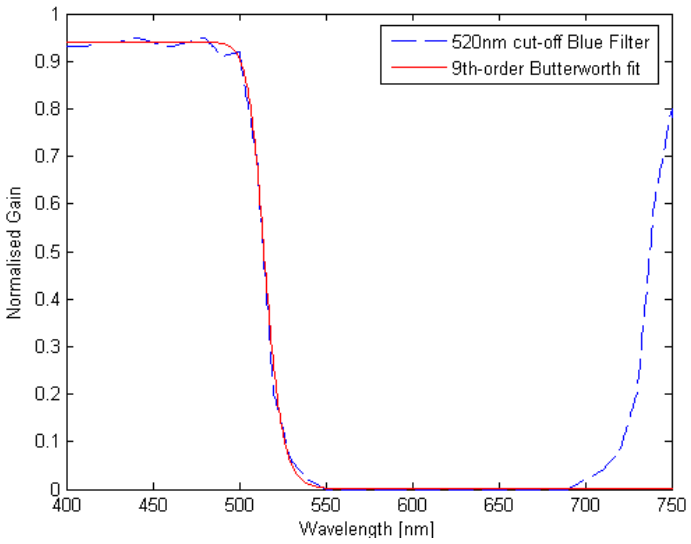

Figure 11. A 520nm low-pass dichroic filter response and a 9th-order Butterworth fitting.

Table 1. Blue filter Melles-Griot MG520-A specifications

Parameter	**Description**
Type/Model No.	Low pass/MG520-A
Butterworth order, k	9
Peak transmittance	0.94
Cut-off/Centre wavelength, λ_c	520nm
Receiver incident angle, θ	90º
Bandwidth	180nm

To reduce detrimental colour shifts due to angular incidence of the incoming beam [4], the filter is placed in front of the optical concentrator, where light has not been focussed to high angles by the optical concentrator. The concentrator increases the amount of received optical power by providing a large area of collection for incident light, and then concentrating it onto a small photo-detector. The limit of the concentration is governed by the conservation of radiance [4]. The maximum collection gain, g_{max} (defined by the ratio of collection area to detection area) is given by

$$g_{\max} = \frac{n^2}{\sin^2 \theta} \tag{14}$$

where n is the refractive index of the concentrator and θ is the semi-angle field-of-view (FOV).

2.2.6 Receiver optical-electrical response

A photo-detector converts the optical power to a photocurrent. The photocurrent, i from the photo-detector is given by

$$i = \int_{400nm}^{750nm} P_r(\lambda) R(\lambda) d\lambda \tag{15}$$

where $R(\lambda)$ is the responsivity of the photo-detector at a specific wavelength, λ. Figure 12 shows the normalised responsivity curve across the visible wavelength for the silicon photo-detector used in the system under consideration [74].

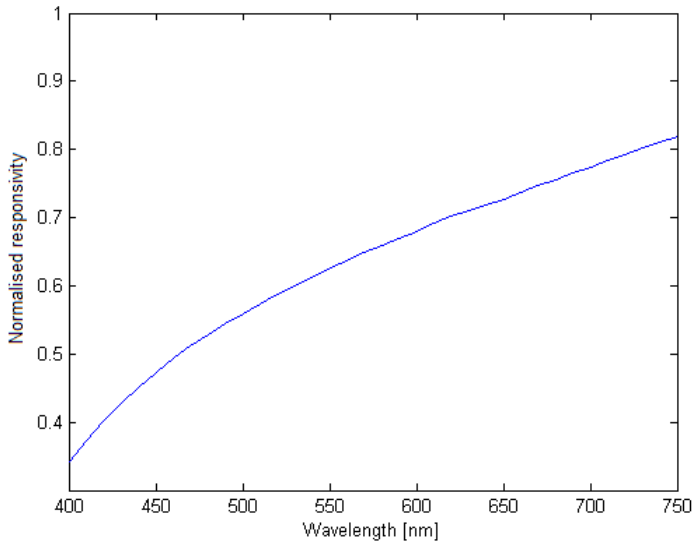

Figure 12. A responsivity curve for a typical silicon photodetector normalised to a peak responsivity of 0.543A/W [74].

In general VLC applications, the average optical power received at the receiver is approximately constant due to DC-bias that is added to ensure a constant room illumination level. Because of this, the average photo-current output of the receiver is constant. The receiver's output photo-current i, is a sum of the standing DC photo-current, i_{dc} and the small signal current, i_{sig} where

$$i = i_{dc} + i_{sig} \quad (16)$$

The modulation depth of the signal is defined as the peak-to-peak amplitude ratio between i and i_{sig}.

2.2.7 SNR estimation

In an additive white Gaussian noise (AWGN) channel, the received noise is modelled as additive, Gaussian and the noise power is evenly distributed across the electrical frequency spectrum. The two dominant sources of noise considered in this model are shot noise from the photo-detection, and amplifier noise. Therefore, the total noise variance (A^2) is expressed as

$$\sigma_{total}^2 = \sigma_{shot}^2 + \sigma_{amp}^2 \quad (17)$$

The shot noise is a function of the total photo-current generated at the receiver. This consists of the photo-current generated from the desired intensity modulated signal, the standing DC photo-current, as well as the unwanted ambient light. The shot noise is given by

$$\sigma_{shot}^2 = 2qiB + 2qi_{ambient}B \quad (18)$$

where $i_{ambient}$ is the photocurrent generated from the ambient light, B is the noise bandwidth, and q is the electron charge. The amplifier noise accounts for thermal and shot noise in the preamplifier. The amplifier noise is given by

$$\sigma_{amp}^2 = N_{amp}^2 B \tag{19}$$

where N_{amp}^2 is the preamplifier noise density in W/Hz. The ratio of signal power, P_{sig} to the total noise variance, σ_{total}^2 *i.e.* the signal-to-noise ratio (SNR) is given by

$$SNR = \frac{P_{sig}}{\sigma_{total}^2} \tag{20}$$

By inserting Equation (18) and (20) into (23), the SNR is given by

$$SNR = \frac{i_{sig}^{\ 2}}{2qiB + 2qi_{ambient}B + N_{amp}^2 B}. \tag{21}$$

Now that the VLC channel model has been described, the following discussions introduce a VLC system testbed that is used in conducting the experimental investigations.

2.3 System Overview

In this section, an overview of the indoor VLC system testbed developed for this investigation is described. Figure 13 shows the block diagram of the components of the testbed.

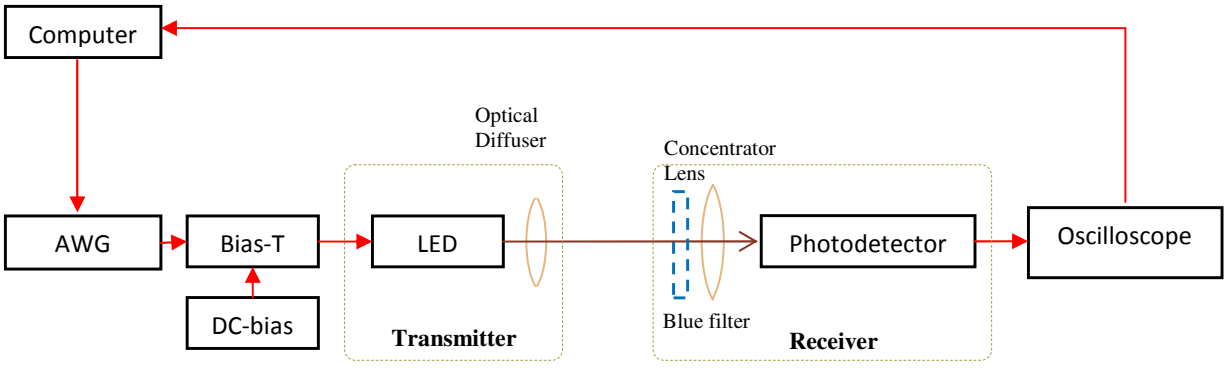

Figure 13. Schematic of an indoor VLC system.

The transmitter consists of an off-the-shelf Luxeon Star-C LXHL-MW1B white high power LED, fitted with an optical diffuser FRAEN FHS-HMB1-LL01-z as shown in Figure 14(a). The optical diffuser has a 5° half-power semi-angle, $\Phi_{1/2}$, which is selected to provide high illumination level at the receiver plane at the cost of a narrow FOV. The LED is driven by a 135mA DC-bias current and the bias current is combined with an electrical output of an arbitrary waveform generator (AWG) Agilent 81150A using a bias-T. The input to the AWG is controlled by a computer. The optical signal from the LED is then transmitted across an LOS channel and is collected by a receiver.

The receiver consists of an aspherical concentrator lens, a silicon photodetector and a transimpedance amplifier. This receiver setup is shown in Figure 14(b). To ensure a high area of light collection area at the receiver, the concentrator lens has a diameter of 4.5cm and *f*-number = 1. For experiments using the blue channel, a dichroic blue filter is placed in front of the concentrator lens (see Figure 13). The receiver is an existing 3x3 multi-element silicon photodetector array as used and described in [75]. Each element of the photodetector is 2.7mm x 2.7mm, and has a capacitance of 9pF at the bias point. The transimpedance amplifier/detector combination has a bandwidth of ~40MHz. A multiplexer is used to switch the received signal to an oscilloscope Agilent DSO5054A for analogue-to-digital (ADC) conversion, and signals are post-processed using MATLAB software.

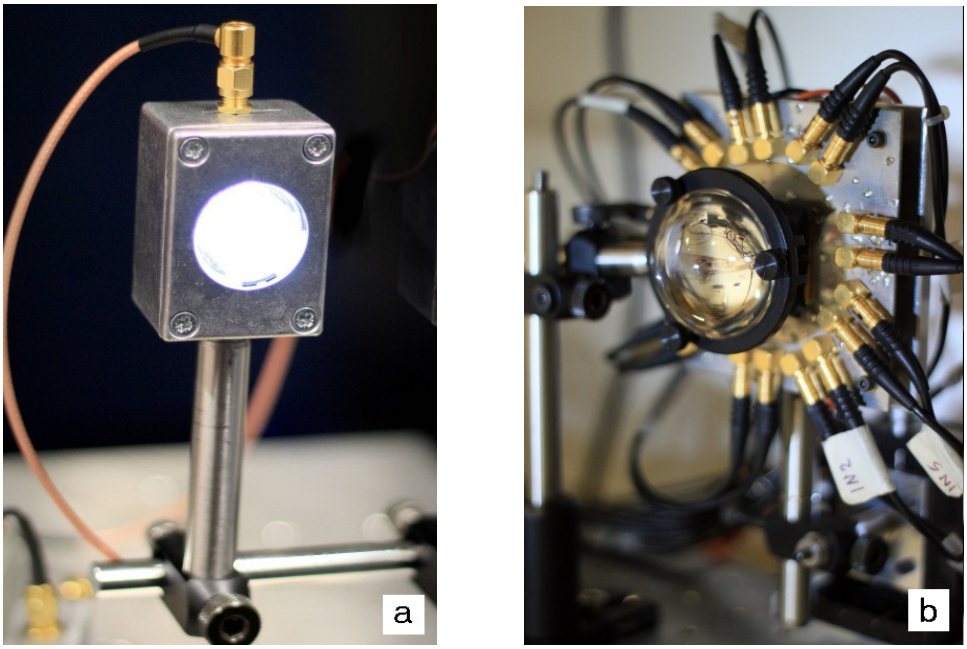

Figure 14. Photographs of SISO transmitter (a) and receiver (b) set up.

2.4 Illumination characteristics measurements

This section presents measurements of the emission spectrum and illumination characteristics of the single-channel system described in Section 2.3. These will be used in a subsequent channel and room illumination simulations.

2.4.1 LED spectral emission profile

The emission spectrum of the LED transmitter is measured using a spectrometer (Ocean Optics SD2000). Based on this emission spectrum, the LED conversion parameter ξ from lumen to watts is obtained to calculate the transmitted optical power. This spectral emission profile is also required for transmission filter design, which is discussed in the following Section 2.5.

The measurement is conducted using the system setup described in Section 2.3, and replacing the receiver with the spectrometer to conduct the measurement. An iris is used at the LED to re-adjust the power level to ensure the spectrometer is not saturated. The measurement is conducted using the following procedure:

1. The spectrometer is first calibrated by measuring the ambient illumination level by switching off the LED transmitter. This ambient illumination level is subtracted from illumination level of subsequent measurements.
2. The LED transmitter is turned on and the LED emission spectral distribution is measured.

Figure 15 shows the measured emission spectral power distribution of the Luxeon Star-C LED normalised to 1-Watt optical power, and the CIE 1931 photopic luminosity function normalised to the peak spectral power distribution. It can be seen that the white LED emission spectrum peaks at two points: 450nm of the blue source emitter, and at 560nm, a component resulting from the phosphor coating on the blue LED chip.

Based on this measurement, the conversion parameter $\xi = 0.0024\text{W}/lm$ for the Luxeon Star-C LED is obtained using Equation (6). With this, the transmitted optical power is calculated. Referring to the electrical-optical response of the LED in Figure 7 in Section 2.2.1, at a 0.135A bias current, the Luxeon Star-C LED has 18*lm* optical intensity. This gives a transmitted optical power of 43 mW.

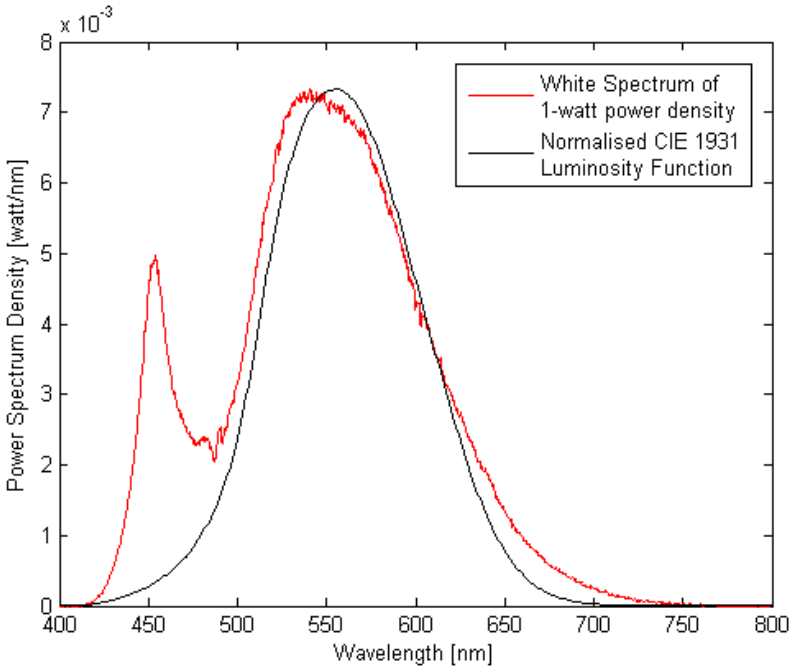

Figure 15. Emission spectrum of the LED (LUXEON STAR-C) measured using a spectrometer (Ocean Optics SD2000) normalised to 1-watt optical power and CIE 1931 standard luminosity function curve with the peak response that is normalised to the peak spectral power distribution.

2.4.2 Illumination level measurements

In this section, the illuminance characteristics of the LED (Luxeon-Star C) are investigated. The aim of this section is to make measurements which validate the illumination model described in Section 2.2.

First, the electrical-optical response of the LED device is obtained by measuring illumination level versus the LED bias-current. A lux meter (SEKONIC L-508) is used to measure the illumination level. This level is measured at a 1m distance between the transmitter and meter while varying the LED bias current from 0.1A to 0.2A. The bias current versus illumination level is recorded as shown in Figure 16. This measurement is compared with the illuminance model described in the Section

2.1.2, based on electrical-optical response (ampere to lumen) in Figure 7. Figure 16 also shows a modelled illuminance versus DC bias current.

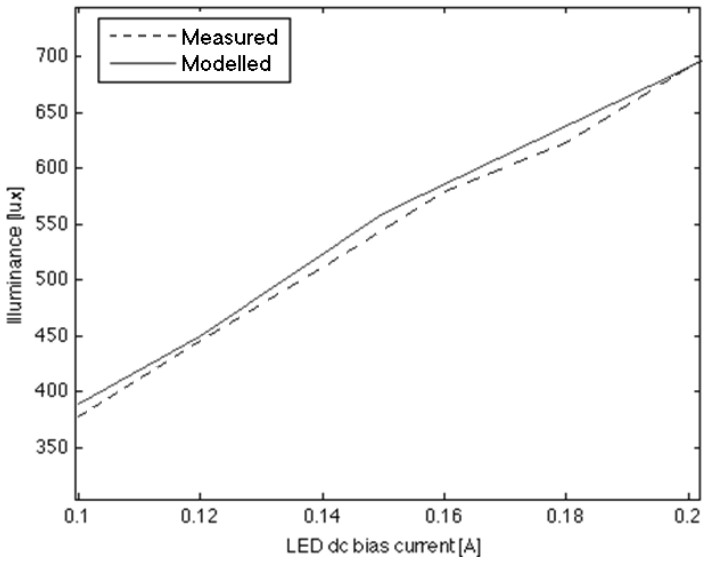

Figure 16. Illuminance versus DC bias current at fixed 1m range.

It can be seen from these results that the measurement closely matches the modelled results.

Next, the Lambertian emission profile of the LED is validated by experimental measurements. Two sets of range and angular measurements were conducted.

First, the illumination level is measured while varying the distance between the LED transmitter and the lux meter from 0.5m to 1.5m, at a fixed bias current of 0.135A.

For the angular emission profile, the illumination level versus angle is measured by displacing the LED source horizontally from 0m to 0.07m from the centre axis at a 1m range at with a fixed 0.135A bias current.

Figure 17 shows measured and modelled illuminance versus range and Figure 18 shows measured and modelled illuminance versus angle. Table 2 summarises parameters used in the model.

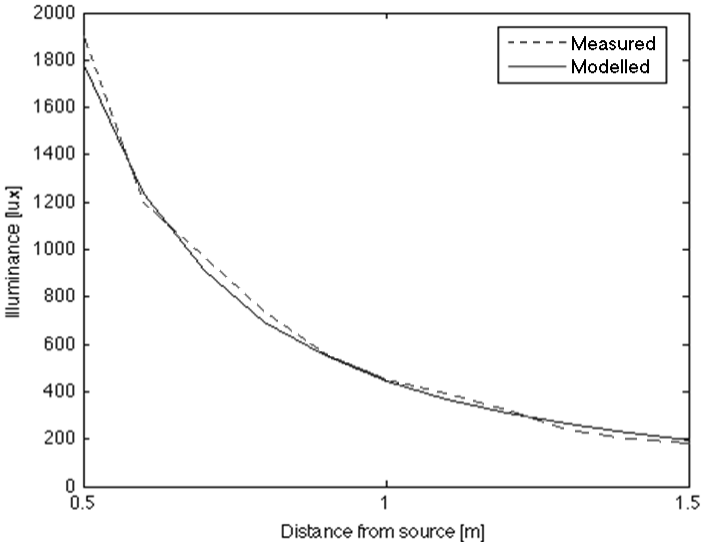

Figure 17. Illuminance versus range at 0.135A DC bias current.

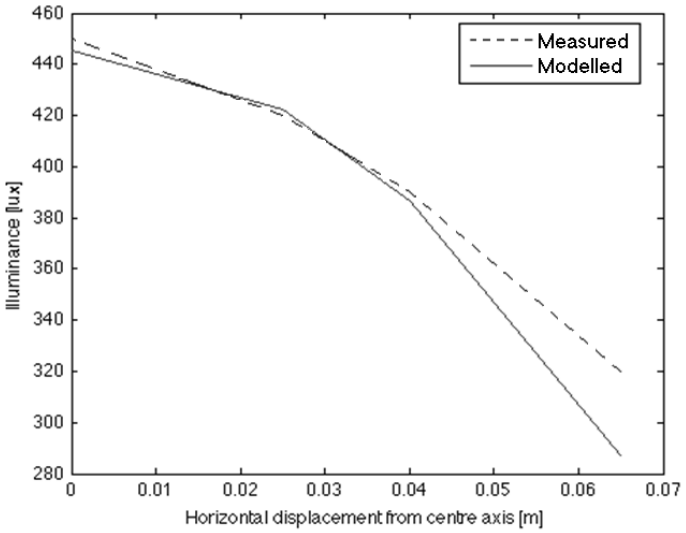

Figure 18. Illuminance versus horizontal displacement at 1m range using 0.135A DC bias current.

Table 2. Parameters for Lambertian radiant intensity model

Parameters	**Description**
Bias Current	0.135A
Luminous Flux, *F*	18 Lumen
Half-power semi-angle, $\Phi_{1/2}$	5º
Receiver incident angle, ψ	90º

It can be seen from these results that the measurement closely matches the modelled results of this specific LED. This model will be used in next section for simulation of a VLC system configuration that provides room-wide illumination coverage.

2.4.3 Simulation of room-wide illumination

The aim of this section is to present a VLC system model for a typical room, which considers room-wide coverage whilst meeting indoor illumination requirements using Luxeon Star-C LEDs. The room considered is 5m x 5m x 3m in size as shown in Figure 19, and is similar to the room described in [11] and [8]. According to illumination standards, the minimum illumination on a work plane is 500*lux* [73] and for purposes such as drawing and writing, a minimum level of illumination between 700*lux* to 1000*lux* is considered acceptable.

s

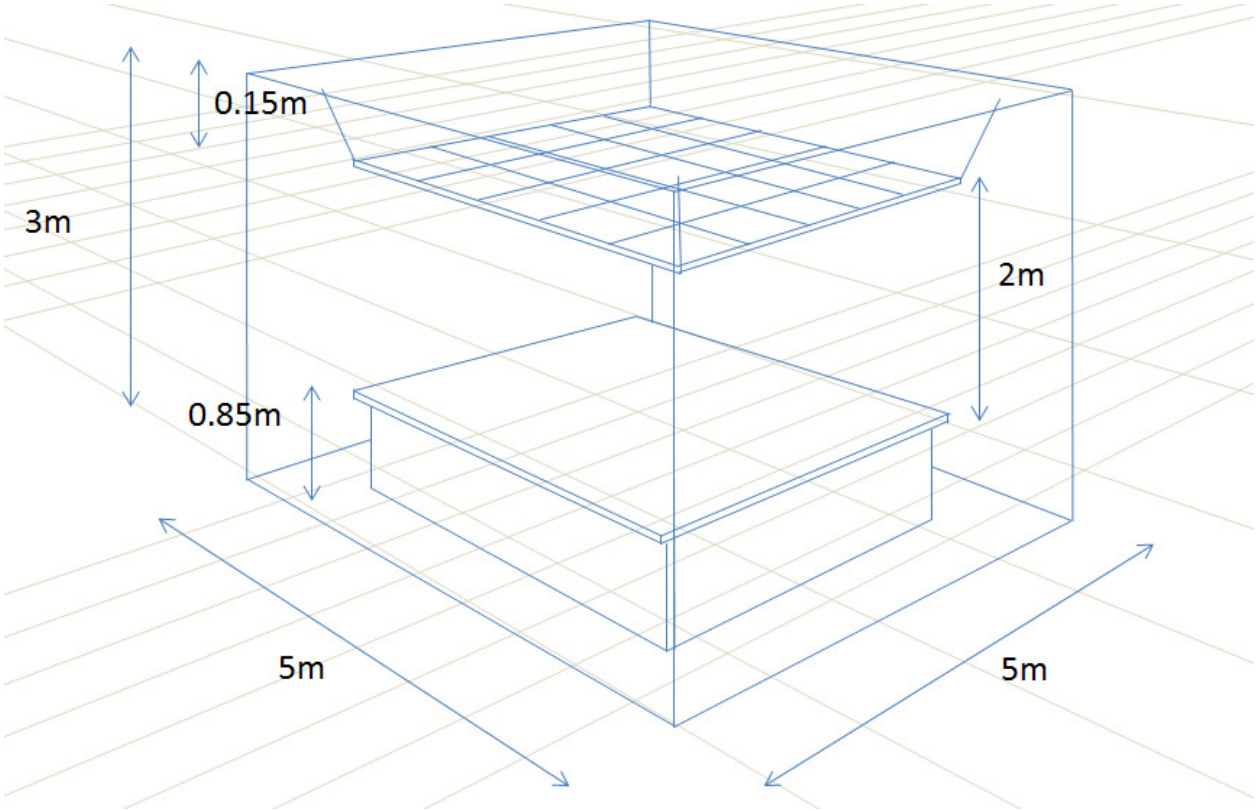

Figure 19. Schematic of a typical room.

In the model, the room is illuminated using a single LED panel. This consists of an array of LEDs and is attached to the ceiling. This functions as the communication transmitter, as well as providing illumination. The illumination level and channel gain for the LOS and diffuse components are as described in Section 2.2.2 and Section 2.2.3.

The aim of this configuration is to provide a uniform illumination level of 1000*lux* on the table's surface plane. In the simulation, a total of 900 LEDs in a 30x30 squared array is used. The receiver is designed to operate on a desk surface plane, which is 2m below from the transmitter. Table 3 shows the parameters used in the simulation.

Table 3. Room illumination specifications

Parameters	Description
Room size (width x length x height)	5m x 5m x 3m
Distance from LED panel to receiving plane.	2m
Semiangle of half power	5 degrees
LED Panel Size (width x length)	4m x 4m
Number of LED units	900 (30 x 30 LEDs)
Luminous Flux	18 Lumen for each LED
Bias Current	0.135A
Wall reflectivity, ρ	0.8

Figure 20 shows simulation of the illumination level on the desk plane: Figure 20a shows the illumination level from the LOS component and Figure 20b shows the contribution from the diffuse component.

It can be seen from the simulation that a total illumination level of 1000*lux* is achievable on the table surface. This simulation performs as a basis for a parallel transmission investigation that is presented in Chapter 5, where an experimental transmission is demonstrated, which is built on a subset of this configuration consisting of 4 Luxeon Star-C LED transmitters.

It can also be seen that the contribution from the diffuse component is relatively small as compared with the LOS component. This is in agreement with several reported simulation results [8, 10, 76]. Therefore, in subsequent chapters, the discussion and analysis are restricted to the LOS components.

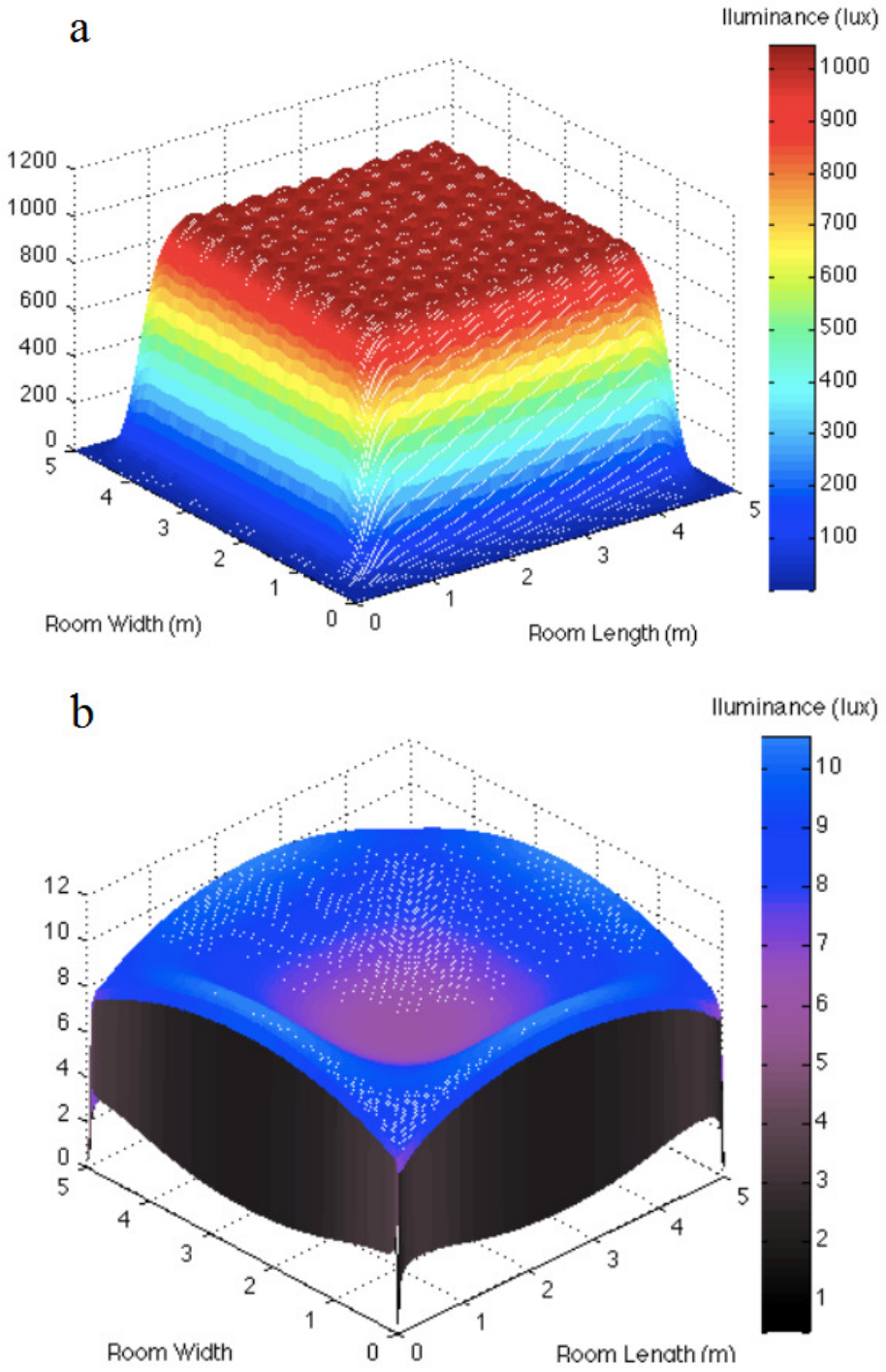

Figure 20. (a) Overall room illuminance and (b) contribution from the diffuse component.

2.5 Transmission filter selection

This section presents an investigation into optical transmission filter selection at the receiver.

There are two competing factors to consider for transmission filter selection: the available signal power and the bandwidth of the EOE channel frequency response after filtering. A blue transmission filter improves the overall bandwidth of the LED frequency response by blocking out phosphorescent components that have a slower response. In addition, this reduces the shot noise due to the photo-current generated from the 'out-of-band' standing DC component and ambient illumination. However, filtering out the phosphorescent component blocks low electrical frequency signal components from the phosphorescent emission that could significantly add to the electrical SNR. Thus, the spectral bandwidth of the filter needs to be efficiently selected to give the best compromise between bandwidth and the electrical SNR.

Several high-speed transmission systems using a blue transmission filter have been demonstrated [26, 28, 61], but the question of the optimum filtering spectral bandwidth has not been addressed.

Two types of blue transmission filters are used for this investigation: a wide-band low-pass filter, and a narrow-band band-pass filter. These filters are selected to represent two cases of filtering that allow different portions of phosphorescent components to pass through. A wide-band filter allows a high level of signal as well as a high level of phosphor component to pass through. A narrow-band filter allows only a narrow emission spectral centred at the peak of the blue spectrum, thus blocking most of the phosphorescent component. Table 4 and Table 5 list down the filter specifications.

Table 4. 520nm low-pass blue transmission filter parameters.

Parameter	Description
Type/Model No.	Low pass/Melles-Griot MG520-A
Peak transmittance	0.94
Cut-off/Centre wavelength, λ_c	520nm
Spectral Bandwidth	180nm

Table 5. 450nm band-pass blue transmission filter parameters [14].

Parameter	Description
Type	Band pass
Peak transmittance	0.70
Centre wavelength, λ_c	450nm
Spectral Bandwidth	40nm

Two measurements are made for each filter: the electrical frequency response and the power spectral distribution. In addition, the unfiltered white LED emission is measured as a reference case.

2.5.1 Frequency response experiments

In this experiment, three cases are examined: 1) no filter, 2) wide-band low-pass filter, and 3) narrow-band band-pass filter. The experiment was conducted using the following procedure:

1. The experiment was performed using the apparatus described in Section 2.3. First, the frequency response measurement of the white emission is conducted where no optical transmission filter is used.
2. The frequency response is measured by sending a train of sine waves sent at 200 different frequencies ranging from 0.1MHz to 100MHz.

3. The range between the LED and receiver, *R* is set to 1m and the peak-to-peak sinusoid drive voltage is set at 0.5V. This ensures that the signal received at the receiver is not saturated *i.e.* clipped.
4. At each frequency point, the averaged signal amplitude is recorded.
5. Step 1-4 are then repeated using the low-pass and band-pass blue filter.

Figure 21 shows a plot of a normalised channel frequency response for the white channel and two blue channels using the two blue optical filters. The electrical -3dB bandwidth of the LED is 2.5MHz, 4.6MHz and 7MHz, for the white light, low-pass and band-pass blue filter responses respectively.

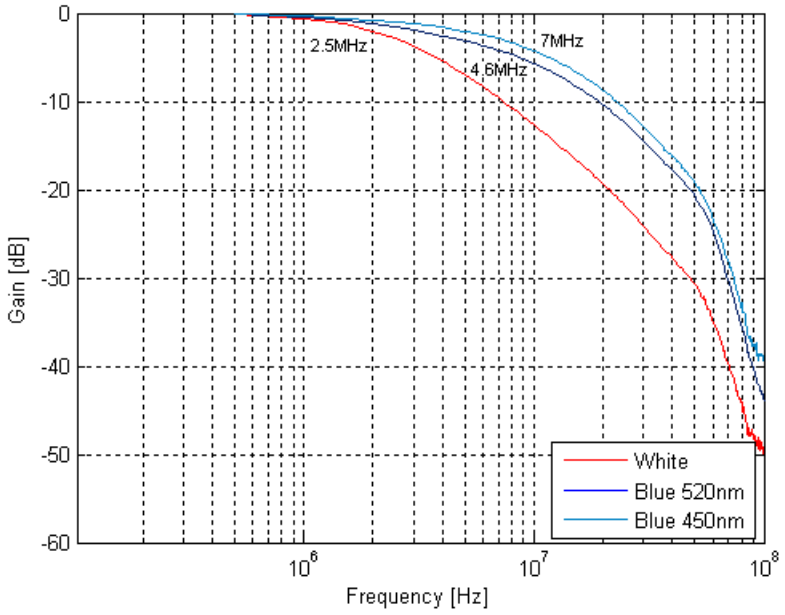

Figure 21. Measured channel frequency response curves for LUXEON-STAR C blue-phosphor LED. The red line shows the measured frequency response of a white emission with a bandwidth, f_{-3dB} of 2.5MHz. The blue lines show the measured blue emission frequency response with a bandwidth f_{-3dB} of 4.6MHz and 7MHz, using the low-pass and band-pass blue transmission filters.

It can be seen from Figure 21 that the white channel has the lowest bandwidth and a higher roll-off factor as compared with the two blue channels. For the blue channel cases, the band-pass filter response (see Blue 450nm in Figure 21) has a higher bandwidth than the low-pass filter response (see Blue 520nm in Figure 21). This is explained by the decreasing phosphorescent components in the respective cases, which an increasingly higher bandwidth.

Further to this, the frequency response at high frequencies is also affected by the bandwidth of the receiver, which has a bandwidth of approximately 40MHz [75]. It can be seen from the measurements that for all three cases, the roll-off factor increases beyond this frequency.

2.5.2 Power spectral distribution measurements

The power spectral distribution measurements were conducted using the same procedure as described in Section 2.4, using transmission filters described in Section 2.5.1. The measured spectral power distribution is fitted to the *k*th-order Butterworth filter response as described in Section 2.2.5. The parameters obtained from this fitting are used in a subsequent SNR simulation in Section 2.5.3.

Figure 22 and Figure 23 show measured and modelled spectral power distributions of the low-pass and the band-pass filter. It can be seen from Figure 22 and Figure 23 that 25% and 8% of the white emission power passes through for the low-pass filter case and for the band-pass filter case respectively. The *k*th-order Butterworth filter responses for both cases are plotted, and the modelled emission spectral responses are included for comparison. Table 6 summarises the parameters taken from the *k*th-order Butterworth fitting for the low-pass and band-pass transmission filter.

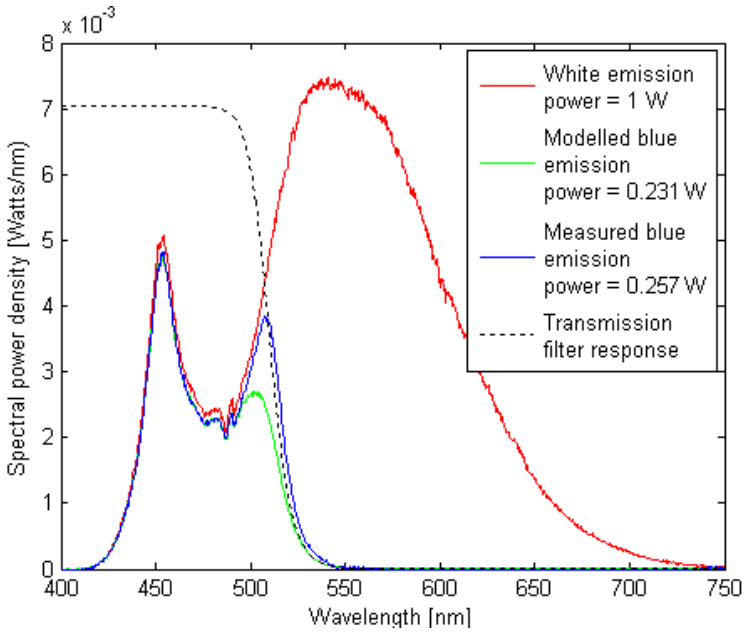

Figure 22. Measured and simulated blue low-pass 520nm transmission filter emission spectral power distribution for Luxeon Star-C LED. The blue emission power after filtering is ~25% of the white emission power. The dotted line presents the *k*th-order Butterworth fitting of the transmission filter response.

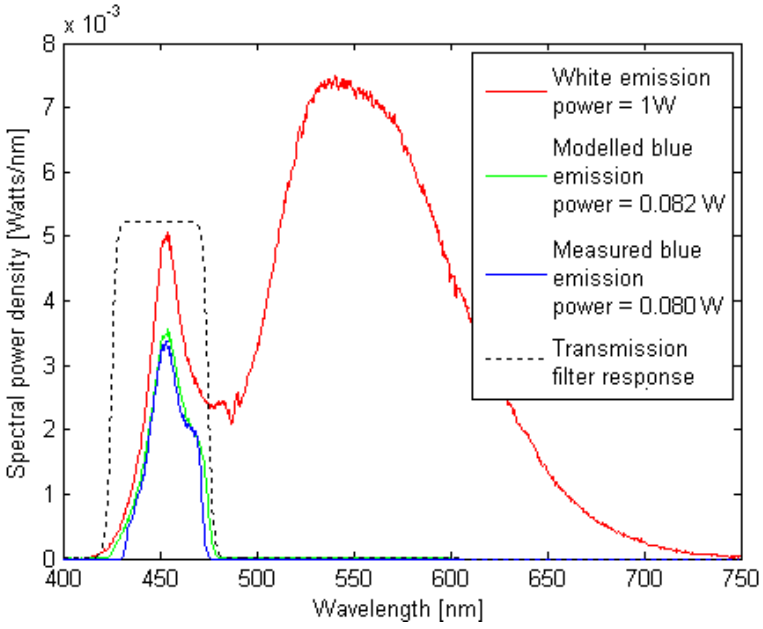

Figure 23. Measured and simulated blue band-pass 450nm transmission filter emission spectral power distribution for Luxeon Star-C LED. The blue emission power after filtering is ~8% of the white emission power. The dotted line presents the *k*th-order Butterworth fitting of the transmission filter response.

Table 6. Blue filter parameters for the *k*-th order Butterworth fitting

Parameter	Description	
	Low-pass (MG520-A)	Band-pass
Butterworth order, k	9	9
Peak Transmittance, T_0	0.94	0.70
Cut-off/Centre wavelength, λ_c	520nm (low-pass cut-off)	450nm (band-pass centre wavelength)
Receiver incident angle, θ	90°	90°
Bandwidth	180nm	40nm

It can be seen from Table 6 that the peak transmittance of the two blue transmission filters are not the same. Because of this, a fair comparison from experimental measurements cannot be obtained, thus a simulation based on the filter model is conducted for the channel SNR analysis in the following Section 2.5.3.

From these measurements, it can be shown that despite a higher bandwidth is obtained by limiting the phosphorescent component of the LED emission, which also decreases the available power at the receiver. In the following section, SNR at various frequencies across the modulation bandwidth is calculated.

2.5.3 Channel SNR calculation

The SNR at various frequencies is obtained using calculation described in 2.2.7, taking into account the channel frequency response, received power and noise. In addition, the average SNR for a specific modulation bandwidth is also calculated for all the three filter cases.

For a fair comparison between the two blue filter cases, a simulation is conducted where the filter loss is ignored *i.e.* the peak transmittance = 1 (100%) for both cases. In this simulation, the transmitted power for all cases is fixed and the illumination at the receiver plane (before filtering) is 460*lux*. Noise is simulated using Equation (18) and Equation (19) in Section 2.2.7, which includes shot noise and amplifier noise. The SNR calculation is conducted with the following procedure:

1. From 460*lux* illumination level, the conversion parameter ξ after filtering is calculated for all three respective filtering cases using Equation (6) in Section 2.2.1. From this, the optical power for the respective cases is calculated.
2. Using Equation (15) in Section 2.2.6, photocurrents generated at DC for respective cases are calculated. This photo-current is distributed across 100 frequency bands from 0.1MHz to 50MHz bandwidth. Each band has a frequency spacing of 0.5MHz.
3. Assuming that $i_{sig} = i$, the photo-current as a function of frequency is obtained by multiplying the generated photo-current in each band with the normalised frequency response $H(f)$ taken from Figure 21 for the respective filtering cases.
4. The SNR as a function of frequency is calculated for each band based on Equation (21) in Section 2.2.7.

Figure 24 shows the result of the channel SNR calculation for the white and two blue channels and Table 7 shows the simulation parameters and the calculated signal power and photo-current for respective filtering cases.

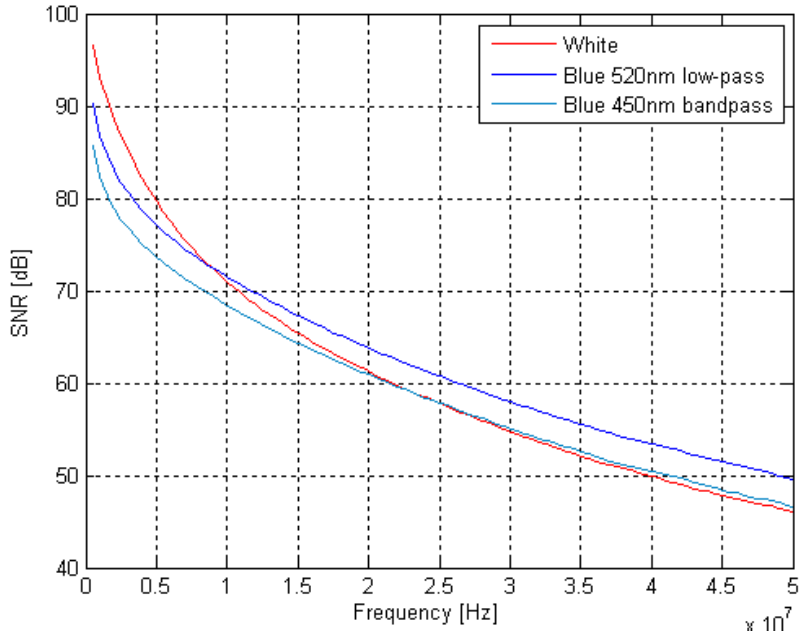

Figure 24. Simulated SNR versus modulation frequency.

At low frequencies, the highest SNR for the white channel and two blue low-pass and band-pass channels is 96dB, 91db and 85dB respectively. At 50MHz, the SNR for white, low-pass and band-pass blue channels is 46.5dB, 50dB and 47dB respectively. It can be seen that the band-pass blue channel has the worst SNR performance because of the small available signal power due to the narrow spectral filter response. The SNR dynamic range for white is ~50dB and for low-pass and band-pass blue filter cases are ~40dB.

It can be seen that the white channel has higher SNR compared to the low-pass blue channel for the frequency band below 8MHz. For frequencies higher than 8MHz, the low-pass blue channel has higher SNR values compared to the white channel. This is due to the low bandwidth and high roll-off of the white channel.

Table 7. SNR simulation parameters and the calculated signal power and photo-current for respective filtering cases.

Parameter	Description
Collection area, A	0.0025m^2
Amplifier Noise Density, N_{amp}	5e-12 A/√Hz
Noise bandwidth, B	50MHz (100 point spacing with ΔB = 0.5MHz)
White Channel	
White optical power	2.2mW
White photo-current	0.7358mA
Blue 520nm-lowpass Channel	
Blue 520nm optical power	0.60mW
Blue 520nm photo-current	0.1681mA
Blue 450m-bandpass Channel	
Blue 450nm optical power	0.23mW
Blue 450nm photo-current	0.0594mA

In order to simulate a system in which a flat-band equalisation is performed, the signal power acrosss all frequencies is flattened *i.e.* averaged and equalised across a specific modulation bandwidth. With this equalised signal power, a flat/averaged SNR across all frequencies within a speficic modulation bandwidth is obtained. This averaged SNR versus modulation bandwidth is calculated for the respective filtering cases for a set of modulation bandwidths up to 50MHz.

Figure 25 shows the average SNR versus modulation bandwidth. It can be seen that the average SNR of the white channel is higher than the average SNR of the two blue channels up to ~20MHz modulation bandwidth. Beyond this point, the low-pass blue channel has a greater average SNR. It can be seen from Figure 25 that the power advantage of the white emission profile outweighs the bandwidth advantage of blue filtering in giving a higher overall SNR for low modulation bandwidth.

However, as modulation bandwidth increases, the high bandwidth advantage of using the low-pass blue transmission filter outweighs the power advantage of the white emission.

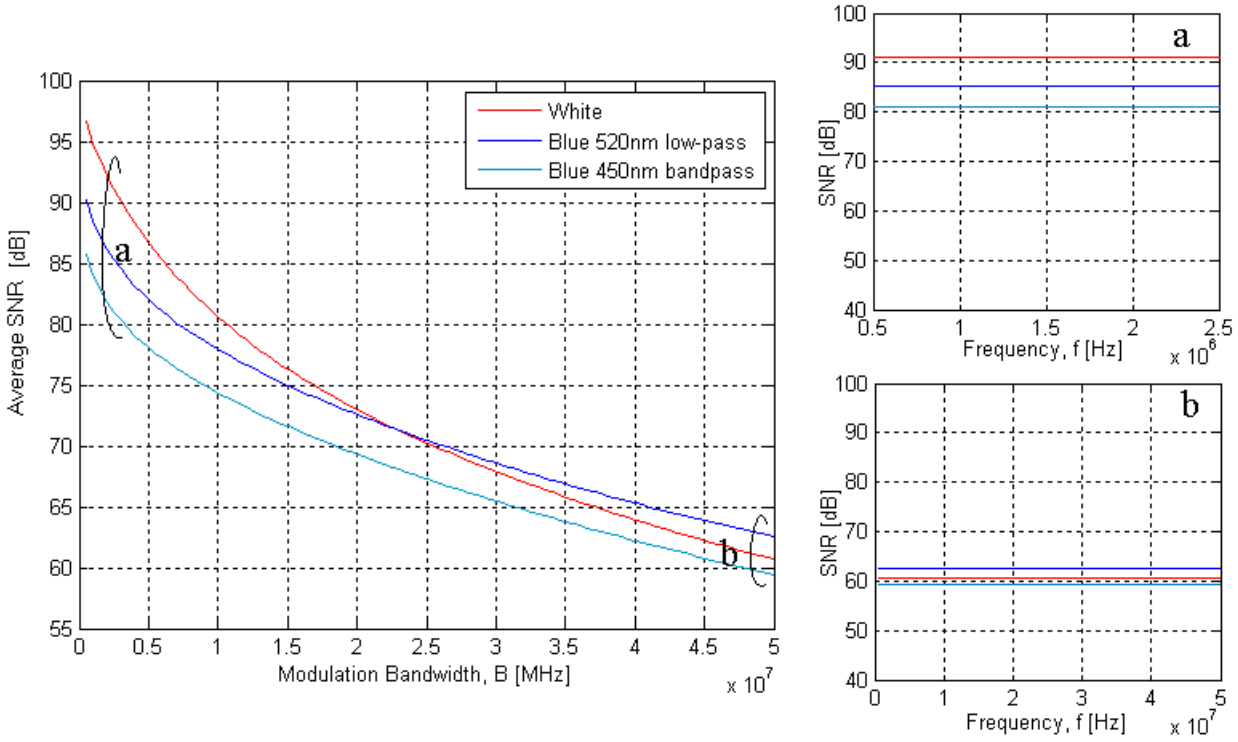

Figure 25. Average SNR versus modulation bandwidth. The insets show the corresponding cross-section of the flat SNR versus frequency curve at instance a) 2.5MHz and b) 50MHz.

For the case of designing VLC systems that is optimised for high bit-rate transmissions, a typically large modulation bandwidth is required to optimise capacity. The low-pass wide-band filter exhibits the highest SNR for high modulation bandwidth of up to 50MHz, thus it is the best candidate between the three cases in improving the overall transmission bit-rates.

Based on simulations and measurements conducted in this section, the VLC system exhibits a channel with high available SNR. However, for practical systems with high channel SNR, the overall

channel SNR dynamic range is typically constrained by the dynamic range of the transmitter and receiver. In the following section, the overall dynamic range of the system is investigated.

2.6 System dynamic range measurement

To evaluate this, this section presents measurements of the dynamic range of the VLC system described in Section 2.3. The experiment is conducted using the apparatus described in Section 2.4.1, where the distance between transmitter and receiver is set at 1m and the bias current is kept constant at 0.135mA. The lux level at the receiver plane is measured at 460*lux*. The dynamic range experiment is performed using the following procedure:

1. Sine waves at 1MHz are transmitted, with a peak-to-peak input voltage (drive voltage) of 0.1V.
2. The averaged peak-to-peak output voltage at the receiver is recorded and the procedure is repeated using increasing peak-to-peak input voltage up to 7V.
3. Noise variance at the receiver is recorded, when the illumination level is maintained but no active sine wave signal is sent. From this noise level, the dynamic range SNR in dB is measured.

From this experiment, it was found that the system has a linear operational range up to 0.7V input voltage, which corresponds to ~0.2V output signal amplitude. Beyond the 0.7V input, nonlinearity in a form of soft-clipping of the signal output starts to occur, and the signal output is fully clipped beyond the 1.0V input which corresponds to the 0. 24V signal output.

In order to understand the source of the nonlinearity, the experiment is repeated with decreasing levels of optical power at the receiver. This is reduced by adjusting the incident angle of the transmitted light on the receiver. This is to ensure that the electrical settings and output levels of the transmitter remain fixed.

Figure 26 shows peak-to-peak input voltage versus peak-to-peak signal output at various illumination levels at the receiver. For 50*lux* illumination level received at the receiver, the full channel electrical-optical-electrical response is not clipped for an input range between 0.1V to 7.0V. This is verification that for this particular input range, the nonlinearity in the output is caused by the receiver.

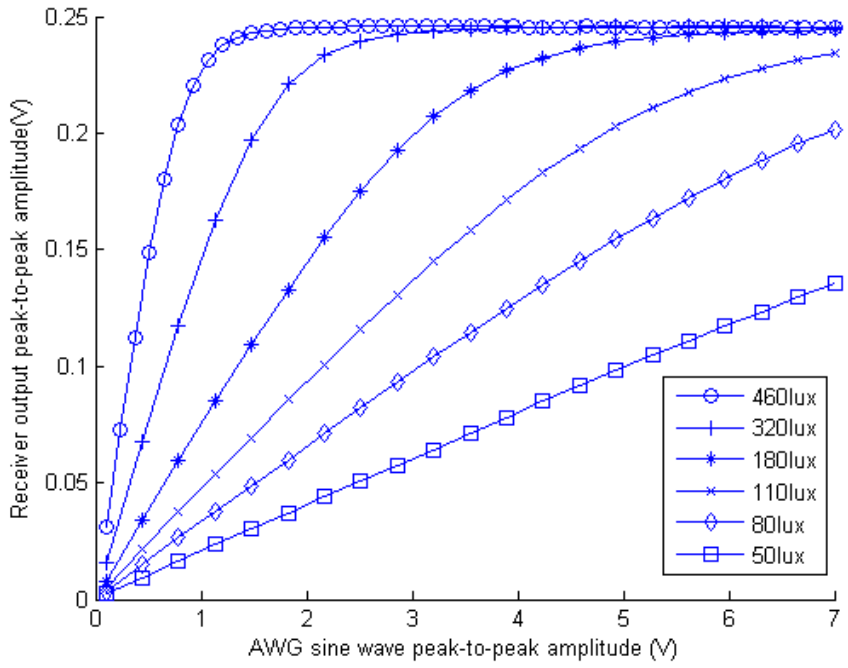

Figure 26. Receiver peak-to-peak output voltage versus sine wave peak-to-peak input voltage at various illumination levels. The saturation voltage of ~240mV which corresponds to ~20dB dynamic range shows the maximum dynamic range of the received signal at the receiver.

Further to this, it can be seen that as the illumination level at the receiver increases from 50*lux* to 460*lux*, the linear operational dynamic range of the system reduces. This is because of the receiver saturation. There have been several applications of automatic gain control (AGC) technique in receiver design [93, 94]. The AGC uses the peak/average signal to adjust the gain to ensure that the receiver is not saturated. This introduces an additional complexity in the receiver design.

2.7 Conclusions

In this chapter, an investigation into the illumination and communication properties of indoor visible light communication systems is presented. A practical VLC system is introduced and the characterisation of this system is presented.

Simulation of a VLC configuration which delivers room-wide coverage at the required indoor illumination level of 1000*lux* using Luxeon Star-C LEDs is also described. From this model it is also demonstrated that the contribution from diffuse components is relatively small in comparison with the contribution from the LOS component.

This chapter also presented an analysis of the effect of blue filtering. A higher bandwidth can be obtained by using a blue transmission filter to limit the phosphorescent component. However, this also decreases the overall received signal power. Based on an SNR analysis of three different emission spectral profiles, the low-pass optical transmission filter provides the highest SNR for systems using high modulation bandwidth, as compared with no filtering, or a typical band-pass filter.

A single-channel system with high SNR profiles is typically limited by the dynamic range of the electrical components in the system. The dynamic range of the experimental VLC system in consideration is measured. It is found that the Luxeon Star-C LED used in this system has a large linear electrical-optical operational dynamic range. However, the dynamic range of the full electrical-optical-electrical link is limited by the receiver, which has an SNR dynamic range of ~20dB.

In conclusion, VLC systems in general have a high available SNR due to indoor illumination level requirements. However, the transmission rates of typical VLC systems are limited by two factors summarised as follows:

1) Low LED bandwidth – The overall electrical-optical-electrical VLC channel bandwidth is limited by the low bandwidth of the LED.
2) Limited dynamic range – The electronics devices in the system typically operate within a linear dynamic range that is lower than the range of the available SNR.

Chapter 3

VLC Systems using OFDM

3.1 Introduction

In the previous chapter, an indoor VLC system is introduced and the characteristics and constraints of the indoor VLC channel are discussed.

In this chapter, the use of higher-order modulation as a method to overcome VLC channel constraints is investigated. As discussed in Section 1.4.2, higher-order modulation schemes offer several advantages in VLC systems. One such scheme, orthogonal frequency division multiplexing (OFDM) is selected as a modulation scheme to be investigated in this thesis because:

1- OFDM is robust against ISI caused by a dispersive channel and multi-path delays in a system with multiple transmitters.
2- The frequency selective feature allows frequency domain equalisation in the digital domain.

This chapter investigates the BER versus bit-rate performance of OFDM to for data transmission in the VLC system described in Section 2.3. The analysis begins by describing OFDM signal generation and signal decoding. An OFDM transmission system is described, and investigations on a set of equalisation methods to improve BER versus bit-rate performance are reported. Also included in this section is an experiment investigating systematic clipping as a method of bit-rate improvement is presented. Limiting cases of the range of the OFDM system in indoor environments are also reported.

3.2 OFDM background

OFDM uses the inverse fast Fourier transform (IFFT) (at the system transmitter) to transform a set of multiplexed, overlapping sub-carriers in the frequency domain to a signal of its time-domain equivalent form.

A single OFDM frame (sometimes also referred to as an OFDM symbol), carries a set of data symbols, X in the frequency-domain. The OFDM symbol is a vector which consists of a set of N subcarriers. The IFFT algorithm outputs the discrete OFDM symbol vector x in the time-domain, which is given by

$$x_m = \frac{1}{N}\sum_{k=0}^{N-1} X_k e^{\frac{j2\pi km}{N}} \quad \text{for } 0 \le m \le N-1 \tag{22}$$

where N is the size of the IFFT and X_k is the k^{th} subcarrier symbol. The corresponding FFT conversion pair to (22) is given by

$$X_k = \sum_{m=0}^{N-1} x_m e^{-\frac{j2\pi km}{N}} \quad \text{for } 0 \le k \le N-1 \tag{23}$$

Each element of the subcarrier symbol vector in (22) is given by

$$X_k = R_k e^{j\theta_k - \theta_{c-k}} K_k \tag{24}$$

where $R_k = \sqrt{x_k^2 + y_k^2}$ is the magnitude and $\theta_k = \tan^{-1}\left(\frac{y_k}{x_k}\right)$ is the angle of the k^{th} complex subcarrier constellation symbol. K_k and θ_{c-k} are the parameters used to adjust the power and phase for each subcarrier. This will be explained further in the description of a pre-equalisation process in Section 3.4.4. The subcarrier representing the DC value at $k = 0$ is left unmodulated. The

subcarrier maintains orthogonality by having an integer number of oscillating cycles in a frame of which adjacent subcarriers differ by one cycle.

The output of (22) is a complex signal and cannot be used in an IM/DD system such as the LED based VLC. Hermitian symmetry is used to achieve a real-valued IFFT output. This is a transpose-conjugate copy of the active subcarriers bin, which is added to the other half of the IFFT frame; where the elements of new IFFT input vector X_H are

$$X_H = [X_{k=0}, X_{k=1}, X_{k=2} \ldots X_{k=N-1}, X_{k=N}, X^*_{k=N-1}, X^*_{k=N-2} \ldots X^*_{k=2}, X^*_{k=1}] \qquad (25)$$

and the DC component, $X_0 = X_N = 0$. This results in a $2N$-point IFFT output of the OFDM symbol. Equation (22) is modified to

$$x_m = \frac{1}{N} \sum_{h=0}^{2N-1} X_{H,h} e^{\frac{j2\pi hm}{N}} \qquad \text{for } 0 \le m \le 2N-1 \qquad (26)$$

where h is the hth-subcarrier symbol of X_H. The OFDM symbol is a periodic function with a period, T_p given by

$$T_p = \frac{1}{\Delta f} \qquad (27)$$

where Δf , the subcarrier spacing is given by

$$\Delta f = \frac{B}{N-1} \qquad (28)$$

where B is the signal modulation bandwidth. Figure 27 shows a schematic of optical OFDM signal generation.

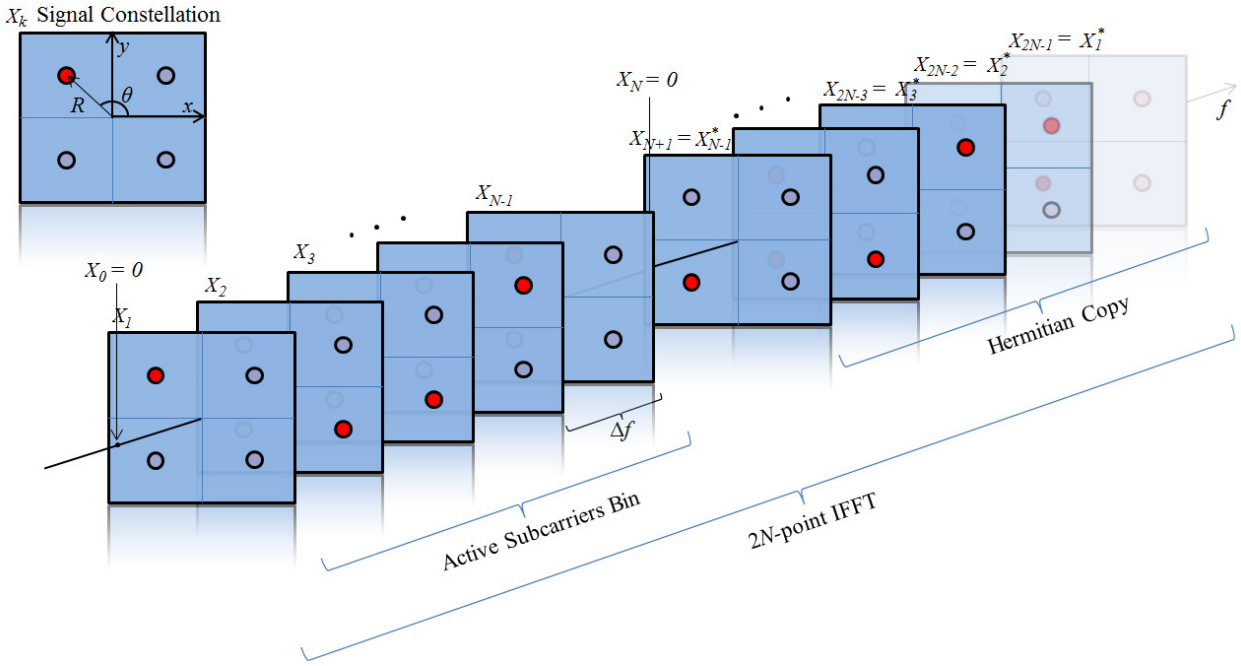

Figure 27. Schematic of an OFDM symbol generation in the frequency domain.

At the receiver, a fast Fourier transform (FFT) operation performs the conversion from the time to the frequency domain and each element of the FFT output Y_h is given by

$$Y_h = \sum_{m=0}^{2N-1} y_m e^{-\frac{j2\pi hm}{N}} \qquad \text{for } 0 \le h \le 2N-1 \qquad (29)$$

where y is vector consists of a set of amplitudes of the received time-domain signal of length $2N$.

In an additive white Gaussian noise (AWGN) channel, the transmitted and the received signal are given by

$$y = x + n_{AWGN} \tag{30}$$

where n is an AWGN noise component, and by substituting (30) in (29),

$$Y_h = \sum_{m=0}^{2N-1} x_m e^{-\frac{j2\pi hm}{N}} + \sum_{m=0}^{2N-1} n_{AWGN,m} e^{-\frac{j2\pi hm}{N}} \qquad \text{for } 0 \le h \le 2N-1 \tag{31}$$

where x_m and $n_{AWGN,m}$ are the signal and noise amplitude of the m-th point of the $2N$ point time-domain signal. $N_{AWGN,\mathrm{h}}$ is a Gaussian noise component of the h-th FFT output at the receiver is given by

$$N_{AWGN,h} = \sum_{m=0}^{2N-1} n_{AWGN,m} e^{-\frac{j2\pi hm}{N}} \qquad \text{for } 0 \le h \le 2N-1. \tag{32}$$

therefore, Equation (31) can be reduced to

$$Y_h = X_h + N_{AWGN,h}. \tag{33}$$

Signal transmission in multipath propagation introduces inter-symbol interference (ISI) which limits the transmission bit-rates. An advantage of OFDM transmission is that it can overcome this ISI problem by using a cyclic prefix, inserted at the beginning of the OFDM frame. The cyclic prefix is a cyclical copy of an end fraction of the OFDM frame. The prefix is longer than the estimated delay spread in the channel; this mitigates the detrimental effect caused by the dispersive channel by localising it in a non-information bearing prefix of the OFDM symbol which is later removed upon reception [77].

3.2.1 DCO-OFDM scheme

The time-domain optical OFDM symbol waveform is real and bipolar. To ensure a unipolar signal to meet IM/DD requirements, a DC-offset is added in the DC-coupled optical OFDM (DCO-OFDM) scheme.

The generation and recovery of the DCO-OFDM scheme is straightforward. A DC-offset (implemented in practice as a dc-bias current to drive the LED transmitter) is added to the generated time-domain waveform to lift the signal into a unipolar region and is then transmitted. The gross data rate for a DCO-OFDM transmission is

$$R_{DCO-OFDM} = \frac{B}{N}\sum_{k=1}^{N-1}\log_2 M_n \tag{34}$$

where B is the modulation bandwidth and $\log_2 M$ represents the number of bits per symbol of a carrier modulation scheme, which is typically M-QAM.

There are several other alternative schemes to create a unipolar signal to meet IM/DD requirements. One such scheme is asymmetrically clipped optical OFDM (ACO-OFDM), which generates a waveform in such a way that its positive and negative parts are symmetrical. Thus, the negative values are clipped and only the positive values are transmitted [54]. Further details on ACO-OFDM and alternative OFDM approaches are discussed in Chapter 5.

3.3 VLC OFDM communications overview

This section describes an OFDM communications experiment that is developed for this investigation. Figure 28 shows the OFDM communications system block diagram.

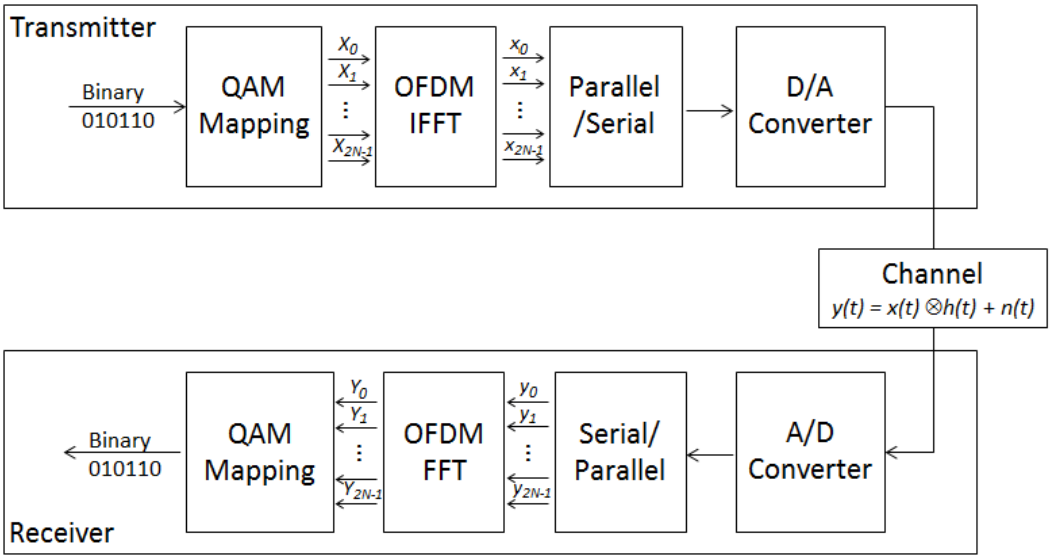

Figure 28. OFDM Communications block diagram.

The OFDM transmission is performed using the VLC system setup and configuration described in Section 2.3. For this transmission, the range is fixed at 1m and the corresponding illumination level is 460*lux*.

Signal generation and recovery is conducted offline using signal processing algorithms that are written using MATLAB software. A set of pseudo-random bit sequences (PRBS) is coded into a series of quadrature amplitude modulation (QAM) symbols. These symbols are then sent to the OFDM encoder to be loaded onto each OFDM subcarrier.

A 2*N*-point IFFT algorithm is used to transform frequency-domain symbols into a 2*N*-point time-domain waveform to form one OFDM frame. 2*N* is the IFFT size, which is typically 2*N* = 64, 256, 512, 1024. A large IFFT size results in a narrow bandwidth of each sub-carrier, which corresponds to a longer symbol period. This increases tolerance against inter-symbol interference (ISI) due to delay spread. Alternatively, a small IFFT size increases tolerance against inter-carrier interference (ICI) due to channel nonlinearity and frequency offset. This is because the influence of nonlinearity

grows with an increase in the symbol period [78]. The contribution of ISI in VLC systems is not as severe as an RF system, because the frequency response of VLC channel falls-off relatively slowly. N= 64 is selected for this experiment. For this experiment the subcarriers are assigned using the DCO-OFDM scheme.

A 10-point cyclical pre- and post-amble is added as a buffer to the 64-point IFFT output to ensure the receiver capacitances are fully charged before valid data is transmitted. This reduces the effect of the 'jump' from no signal to an OFDM waveform. This waveform is then oversampled by 10 points per sample and is sent to the AWG for transmission, where digital to analogue conversion takes place. This signal is then transmitted using the Luxeon Star-C LED across the VLC channel and detected at the receiver.

Upon detection at the receiver, the OFDM signal is captured by an oscilloscope where analogue to digital conversion takes place. MATLAB is used for subsequent processing. The waveform is then converted back to the frequency domain by the fast Fourier transform (FFT) algorithm. OFDM subcarrier symbols are recovered and QAM constellation quantisation process takes place to retrieve the information bits. Finally, the retrieved bits are sent for bit-error rate (BER) estimation.

3.4 OFDM equalisation

Key to the success of OFDM is equalisation. The aim of this section is to investigate the bit-rate versus BER performance of the OFDM communication system using a set of equalisation methods that work both in the time and frequency domains.

3.4.1 Time domain post-equalisation

From Equation (31), the communication signalling in AWGN channel can be represented by:

$$Y = XH_{CH}(f) + N_{AWGN} \tag{35}$$

where Y and X are the received and transmitted signal vectors in the frequency domain, $H_{CH}(f)$ is a complex number representing the EOE channel frequency response and N_{AWGN} is an additive white Gaussian noise component.

As described in Section 2.5, the overall data rate is limited by the low LED bandwidth. Several synchronisation methods have been applied in OFDM systems, including sine wave training sequences and pilot tones [50, 79-81]. However, due to this low-pass channel characteristic, synchronising the received frame-based time-domain OFDM symbol is difficult to perform because the high-frequency signal is highly attenuated. To counteract this, a discrete-time post-equalisation (Post-TDE) is performed before the synchronisation process.

In this investigation, a straightforward approach is investigated. A Post-TDE of the received OFDM signal is performed, and an autocorrelation synchronisation technique is then used. This allows the starting point of the received OFDM symbol frame to be detected [14]. The autocorrelation is conducted between the transmitted and received OFDM training symbol using a MATLAB-based cross-correlation algorithm. Figure 29 shows a system schematic showing the post-equalisation processing module.

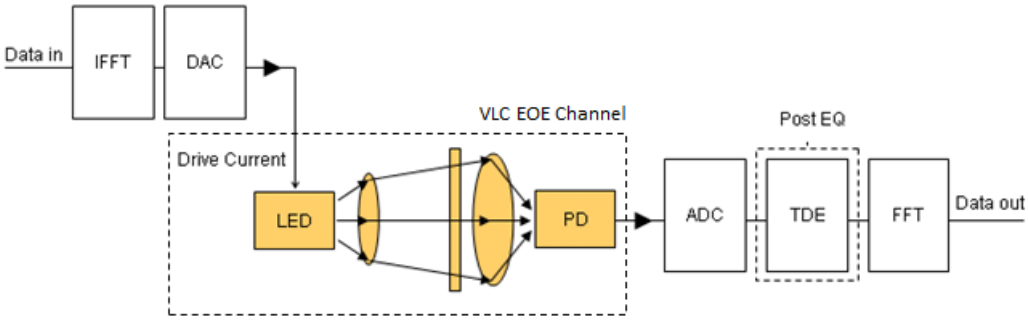

Figure 29. VLC OFDM system schematic showing the Post-TDE equaliser processing modules.

The Post-TDE response used is the inverse of the response of the channel, where

$$H_{TDE}(f) = \frac{1}{H_{CH}(f)} \tag{36}$$

thus giving the estimated received symbol

$$\hat{X}_{TDE} = YH_{TDE}(f) = X + N_{AWGN}H_{TDE}(f). \tag{37}$$

For processing simplicity, a first order high-pass filter is selected as the estimated channel response, using the measured -3dB bandwidth of the full channel as the bandwidth. The equaliser first order high-pass filter response is given by

$$\hat{H}_{TDE}(f) = 1 + j\left(\frac{f}{f_c}\right) \tag{38}$$

where f_c, is the -3dB bandwidth of the LED.

The time-domain post-equalisation bit-rate versus BER experiment was conducted using the following procedure:

1. A set of 500 64-point DCO-OFDM frames was sent at a bit-rate of 10Mbps to 350Mbps. Each frame transmits 16-QAM symbols on each 31 active subcarriers. The received time

domain signal is post processed without equalisation and the BER versus bit-rate plot is obtained.

2. Next, time domain equalisation was applied to the same received signal for comparison. The discrete received time-domain signal was equalised using a direct form II transposed digital filter function in MATLAB [14] in which f_c = 4.5MHz. The BER versus bit-rate plot for the equalised transmission is obtained.

Figure 30 shows the bit-rate versus BER from 10Mbps to 350Mbps for both cases. The Post-TDE signal achieved a bit-rate of up to ~130Mbp/s before exceeding a BER of $2x10^{-3}$. A BER of $2x10^{-3}$ is taken as the target BER because this level can be further reduced with a forward error correction (FEC) coding algorithm [82]. However, the BER for the signal without Post-TDE was above $2x10^{-3}$ for all transmission bit-rates. Hence, it is demonstrated that Post-TDE greatly improves the bit-rate performance for this transmission. It can be seen from Figure 30 that BER is degraded at lower data rate. This is due to the limitation of the equipment that is the Bias-T used has a high-pass characteristic at low frequency. This effect can be removed by deactivating low-frequency subcarriers to avoid operating within this frequency band, with a penalty of a reduction in the overall bit-rate. However, in order to maintain consistency in the experimental procedures, all subcarriers are active.

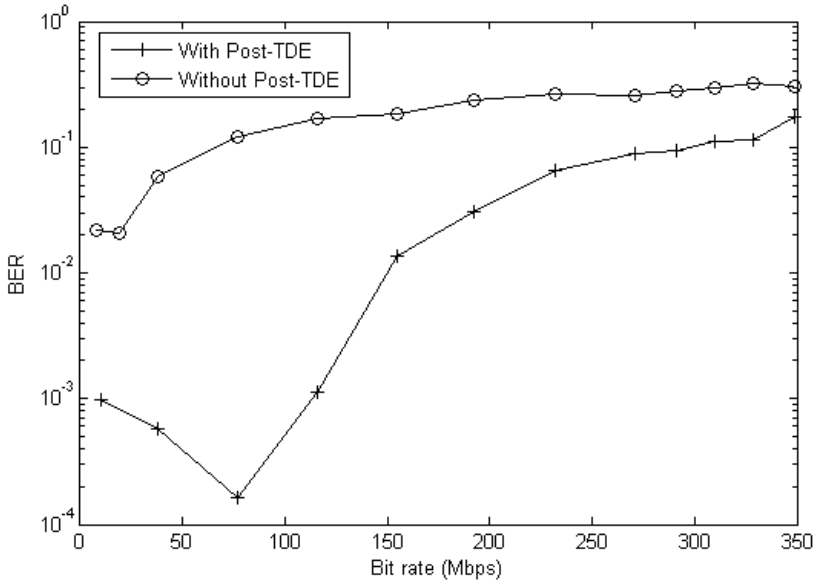

Figure 30. BER versus bit-rate for 16-QAM DCO-OFDM transmission with and without Post- TDE for this particular experimental setup.

Figure 31 shows a comparison between transmitted and received time-domain waveforms, with and without Post-TDE. The time domain waveforms are shown at bit-rates of ~100Mbps and ~360Mbps, which correspond to a modulation bandwidth of 25MHz and 90MHz respectively. As the modulation bandwidth increases from 25MHz to 90MHz, it can be seen that the waveform is less well-matched with the actual transmitted signal. This is due to the low-pass channel. Post-TDE boosts the high frequency components (both signal and noise) and improves the received waveform allowing signal synchronisation. The Post-TDE process is therefore used prior to the FFT algorithm to enable subsequent processing in the frequency domain.

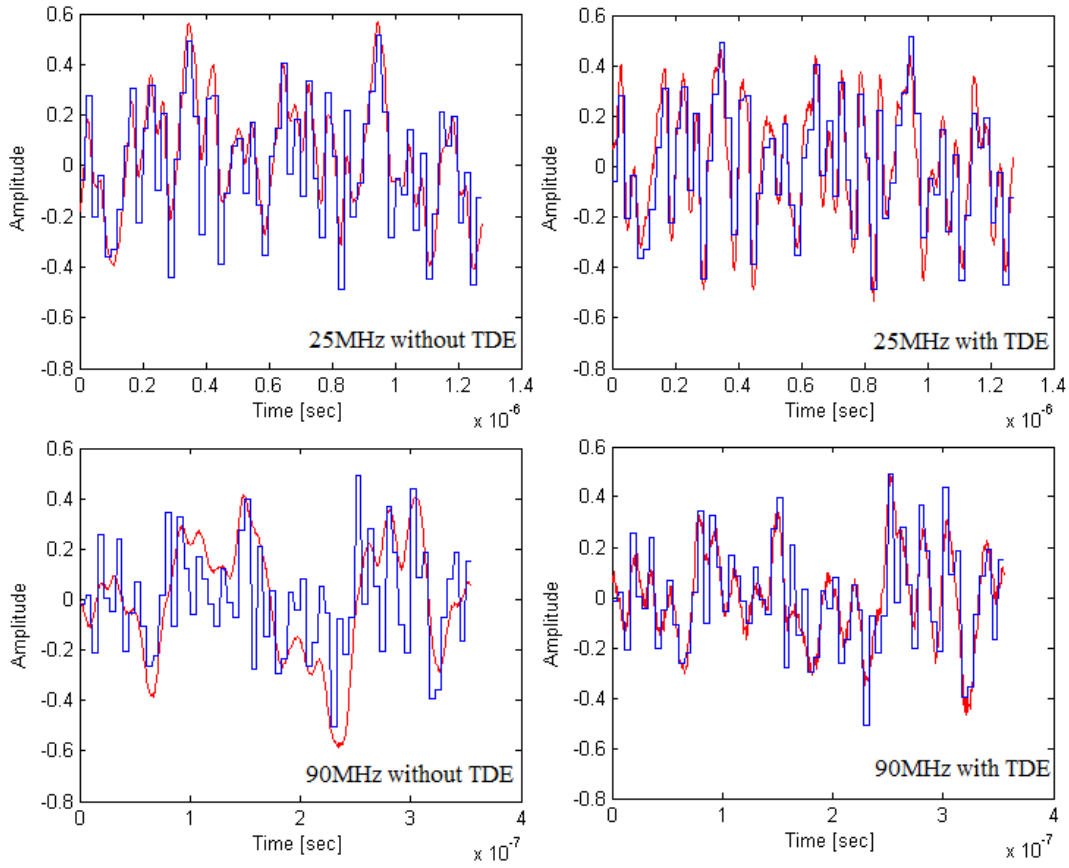

Figure 31. Transmitted (blue) and received (red) OFDM time-domain waveforms without Post-TDE (left) and with Post-TDE (right) for a modulation bandwidth of 25MHz and 90MHz.

However, for the case of the Post-TDE signal, it is observed that the received constellation has a severe subcarrier phase error. This results in a rotation of the received symbol constellation which significantly contributes to the bit error count. This effect is explained by imperfect estimation of the Post-TDE response, $\hat{H}_{TDE}(f)$ as an inverse of the VLC channel response, $\frac{1}{H_{CH}(f)}$. The solution to mitigate this effect is reported in the following section using a frequency domain equalisation (Post-FDE) that is incorporated with the Post-TDE operation.

3.4.2 Frequency domain post-equalisation

As mentioned, the Post-TDE operation is required for signal synchronisation but an imperfect match between the Post-TDE frequency response and the VLC EOE channel frequency response results in rotated symbol constellations that increase the BER. To counter this, a frequency-domain post-equalisation (Post-FDE) is introduced. This method adds another layer of equalisation to further 'fine-tune' the frequency response of the equaliser to better match the frequency response of the channel.

In an imperfect $\hat{H}_{TDE}$ estimation case where $H_{TDE} \neq \frac{1}{H_{CH}}$, Equation (37) can be rearranged to represent the Post-TDE signal as

$$Y_{TDE} = XH_{CH}(f)H_{TDE}(f) + NH_{TDE}(f). \qquad (39)$$

Figure 32 shows an OFDM system schematic showing the Post-TDE and Post-FDE modules.

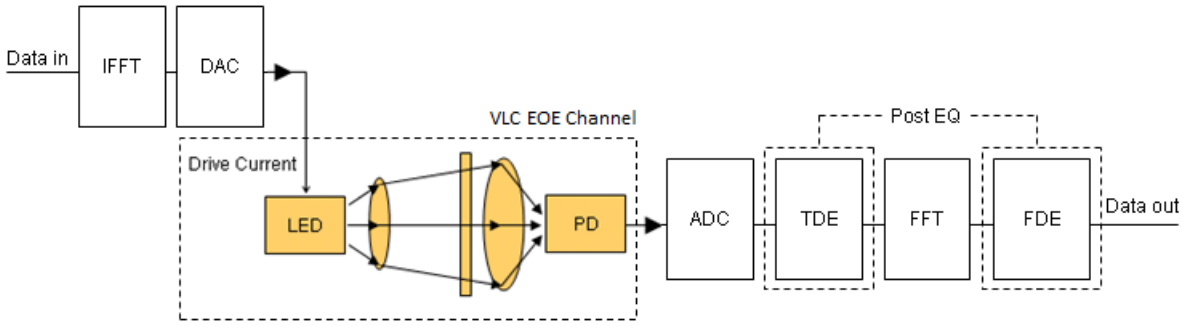

Figure 32. VLC OFDM system schematic showing the post-equalisation process (Post EQ) consisting Post-TDE and Post-FDE modules.

This equalisation is in the frequency domain for each subcarrier symbol. The Post-FDE response is

$$H_{PostFDE}(f) = \frac{1}{H_{CH}(f)\hat{H}_{TDE}(f)} \tag{40}$$

and the estimated Post-FDE symbol is given by

$$\hat{X}_{FDE} = Y_{TDE} H_{PostFDE}(f) = X + \frac{N_{AWGN}}{H_{CH}(f)} \tag{41}$$

The Post-FDE response can be estimated from a training operation. A known sample, X is transmitted and this sequence is repeated to allow averaging and noise reduction. For a large averaged sample of $Y_{TDE,}$ the AWGN noise component is averaged to zero, thus Equation (41) can be reduced to

$$Y_{TDE} = XH_{PostFDE}(f) \tag{42}$$

and the estimated Post-FDE frequency response is given by

$$\hat{H}_{PostFDE}(f) = \frac{X}{Y_{TDE}}. \tag{43}$$

where X and Y_{TDE} are set of vectors of transmitted and received OFDM symbol in frequency-domain, in which each element in X and Y_{TDE} represents the transmitted and received complex symbol on each subcarrier.

As each OFDM subcarrier is available separately in the OFDM domain, a specific Post-FDE response for each subcarrier symbol can be obtained. Referring to Equation (24) in Section 3.2, Equation (43) can be rearranged to give

$$\hat{H}_{PostFDE,k} = \frac{R_{X,k}}{R_{Y,k}} e^{j(\theta_{X,k} - \theta_{Y,k})} \quad (44)$$

$$= R_{FDE,k} e^{j\theta_{FDE,k}} \quad (45)$$

where $R_{X,k}$, $R_{Y,k}$ and $\theta_{X,k}$, $\theta_{Y,k}$ are the respective magnitudes and phases of the transmitted and received symbols for the k^{th} subcarrier; and $R_{FDE,k}$ and $\theta_{FDE,k}$ are the magnitude and phase response of the Post-FDE for the k^{th} subcarrier.

The frequency-domain post-equalisation bit-rate versus BER experiment was conducted using the following procedure:

1. First, a training run was conducted to obtain the frequency response of the Post-FDE equaliser by sending a sequence of 500 64-point DCO-OFDM frames. Each OFDM frame consists of 31 subcarriers, with each carrying a known 4-QAM symbol. These are transmitted and the frames were retrieved at the receiver end. The phase and normalised magnitude were averaged for each of the 31 subcarriers across 500 frame samples. The Post-FDE frequency response is obtained using Equation (44).

2. The experiment was conducted for bit-rates between 10Mbps to 350Mbps. Based on the measured Post-FDE response, received symbols are equalised by derotating the phase and normalising the magnitude of the constellation. The BER is calculated and recorded.

Figure 33 shows the magnitude and phase response of the Post-FDE equalizer measured for 31 subcarriers across a 90MHz modulation bandwidth corresponding to a bit-rate of ~350Mbps.

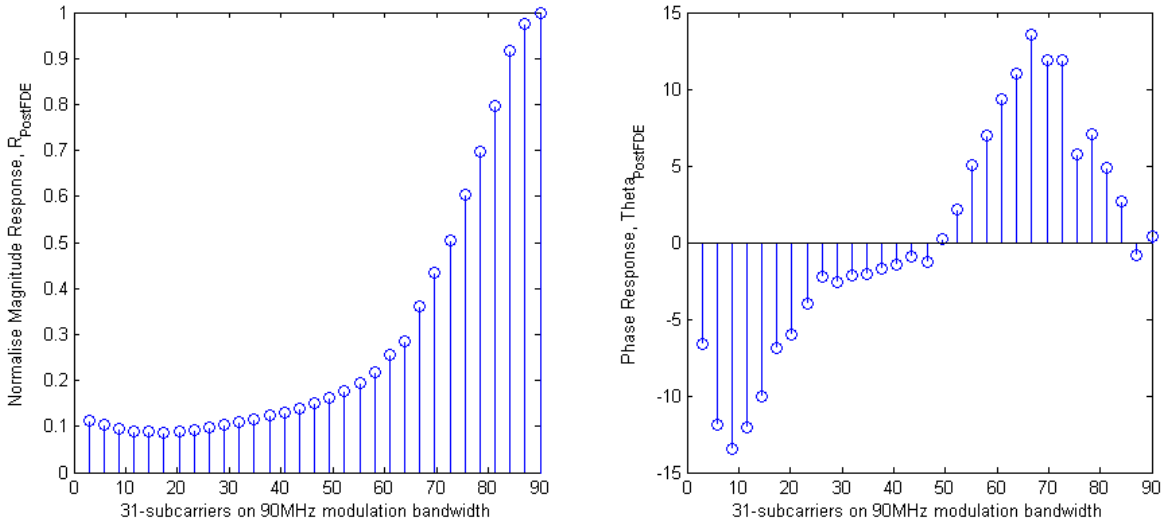

Figure 33. Magnitude, R_{FDE} and phase, θ_{FDE} response of the Post-FDE for individual subcarrier index across a 90MHz modulation bandwidth.

Figure 34 shows the signal constellation of all Post-TDE recovered 31 training subcarrier symbols in 500 OFDM frames before and after the Post-FDE process.

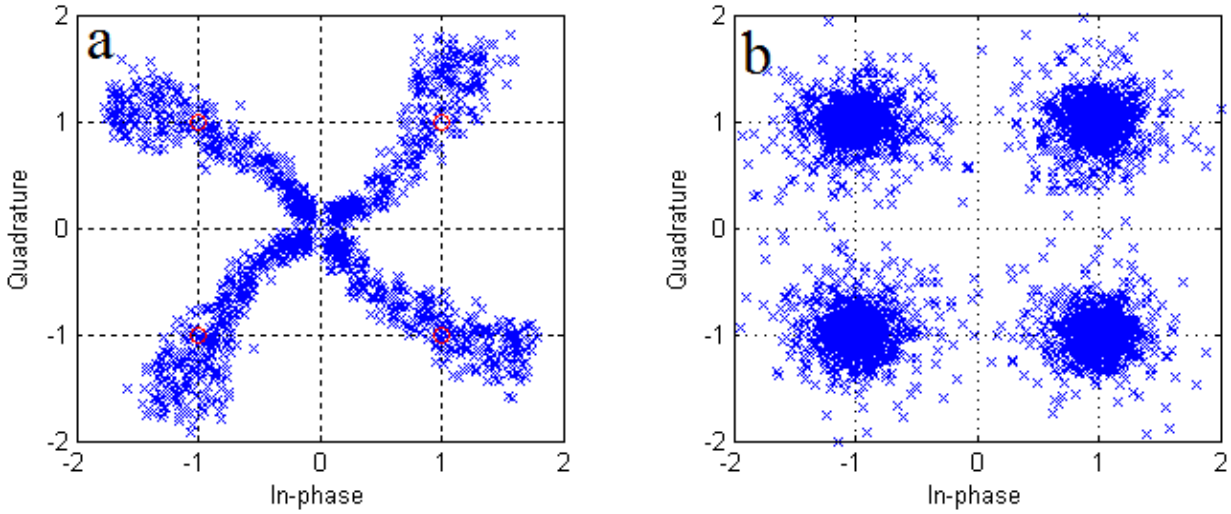

Figure 34. Signal constellation of all 31 training subcarriers symbols of 500 OFDM frames before (left) and after (right) Post-FDE at modulation bandwidth of 90MHz.

Figure 35 shows the BER versus bit-rate from 10Mbps to 350Mbps for transmission without equalisation, with Post-TDE equalisation alone, and with Post-TDE and Post-FDE. The Post-FDE equalisation alone without the Post-TDE is not feasible as this is used for synchronisation which is required before the IFFT processing.

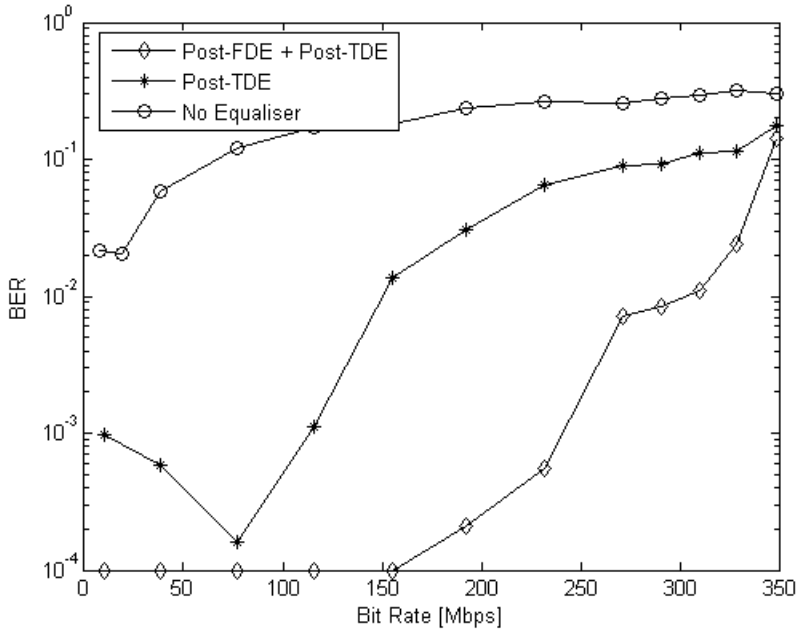

Figure 35. BER versus bit-rate for 16-QAM DCO-OFDM transmission with and without Post- FDE.

The Post-FDE transmission achieves a bit-rate of up to ~250Mbps before exceeding a BER of $2x10^{-3}$. In comparison with the cases of only Post-TDE or no equalisation applied, the Post-FDE equaliser greatly improves the performance.

Referring to Equation (37) and (41), the Post-TDE and Post-FDE processes are conducted at the receiver when the detected signal is already impaired with noise, thus by boosting high frequency components of the channel response increases the noise as well as the signal. Therefore, the

respective signal-to-noise ratios (SNR) for the individual subcarriers remain the same before and after post-equalisation.

To overcome this, a frequency-domain pre-equalisation (Pre-FDE) method is introduced. This method equalises the power distribution to each subcarrier at the transmitter so that the received SNR for each subcarrier at the receiver is similar. To enable this, the subcarrier SNR at the receiver is required. In the following section, an error-vector magnitude (EVM) measurement is introduced to estimate the subcarrier SNR at the receiver. This method measures the error-vector *i.e.* the aggregate departure of the received symbol from its actual expected point on the constellation.

3.4.3 Error-vector magnitude measurements

EVM is a common figure of merit for system linearity in wireless communications standards. It can be related to the channel SNR, under assumptions that the noise distribution is AWGN and the *M*-QAM constellation is quadratic [83]. The quality of received symbols is measured from the root-mean-squared (RMS) difference between received and the expected symbol. This value is often shown as a percentage of the average power per symbol. Figure 36 shows a typical error vector of a normalised measured symbol.

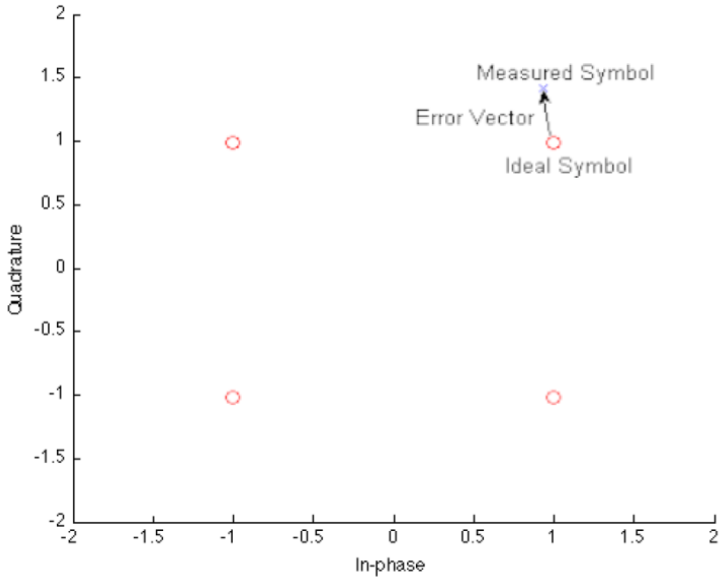

Figure 36. Error vector; a scalar departure length of a measured symbol from the ideal symbol.

For the OFDM transmission case, the EVM is calculated for each subcarrier, and from the EVM the subcarrier SNR can be estimated. The averaged mean-squared EVM can be related to SNR by [84]:

$$SNR_{dB} = 10\log\frac{1}{EVM^2} \tag{46}$$

A channel EVM measurement is conducted to obtain the SNR estimation for each subcarrier channel across a specific modulation bandwidth. The channel EVM measurement was conducted using the following procedure:

1. A set of 100 64-point DCO-OFDM frames was sent at ~100Mbps, which corresponds to a 25MHz modulation bandwidth. Each frame transmits known 4-QAM symbols on each of the 31 active subcarriers.

2. After Post-TDE and Post-FDE equalisation the EVM for each sub-carrier is measured. The SNR for each subcarrier was estimated from the measured EVM. The measurement is

repeated across a modulation bandwidth of 50MHz, 75MHz and 90MHz, which corresponds to bit-rates of ~200Mbps, 300Mbps and 360Mbps respectively.

Figure 37 shows the estimated SNR for each subcarrier across a modulation bandwidth of 25MHz, 50MHz, 75MHz and 90MHz. It can be seen that as the modulation frequency increases, the SNR for high frequency subcarriers decreases, due to the frequency response of the LED transmitter (beyond 4.5MHz), and the receiver (beyond 40MHz). In the next section, an iterative pre-equalisation module is introduced which uses the subcarrier SNR information to equalise each subcarrier symbol at the transmitter.

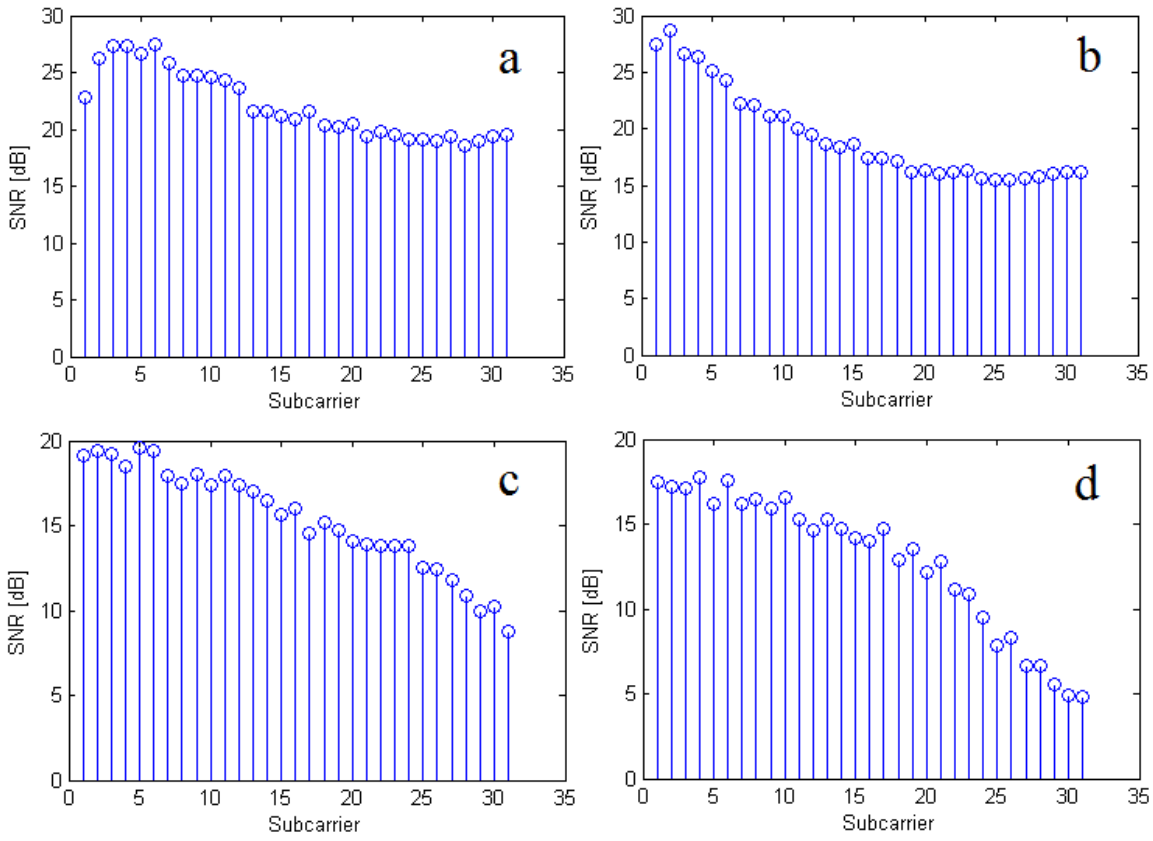

Figure 37. Subcarrier SNR estimation based on EVM measurement for DCO-OFDM transmission with modulations bandwidth of (a) 25MHz (b) 50MHz (c) 75MHz and (d) 90MHz.

3.4.4 Iterative frequency domain pre-equalisation

In this section, an iterative Pre-FDE method for maximising transmission performance is presented. As discussed, a post-equalisation method equalises the received signal which has been corrupted with noise. The pre-equalisation method on the other hand, equalises the transmitted signal prior to transmission by adjusting the power to each subcarrier at the transmitter.

The Pre-FDE transmitted signal can described as

$$X_{PreFDE} = XH_{PreFDE}(f) \tag{47}$$

where H_{PreFDE} is the Pre-FDE frequency response. The Pre-FDE frequency response is estimated from a training process, which will be explained in the following pages. This allows the power to each subcarrier is allocated based on the subcarrier SNR estimation. The power is distributed from the high SNR subcarrier to the low SNR subcarrier via means of an iterative process.

Substituting X_{PreFDE} in Equation (47) with the transmitted signal, X in Equation (35) gives

$$Y = XH_{PreFDE}(f)H_{CH}(f) + N_{AWGN}. \tag{48}$$

The received set of symbols, Y is sent through the post-equalisation blocks, and Equation (48) becomes

$$\hat{X}_{PreFDE} = XH_{PreFDE}(f) + \frac{N_{AWGN}}{H_{CH}(f)} \tag{49}$$

where $\hat{X}_{PreFDE}$ is the new estimate of the pre-equalised signal. It can be seen from Equation (49) that the noise components are not affected by the frequency response of the Pre-FDE, thus the signal can be adjusted independently of the noise.

The Pre-FDE response adjusts the power to each subcarrier based on the subcarrier SNR estimation. The power is distributed from the high SNR subcarrier to the low SNR subcarrier via means of an iterative process.

At high frequencies, SNR decreases due to the low-pass characteristic of the channel. The high SNR that is available at low frequencies is constrained by the dynamic range of the receiver. Figure 38 shows a simplified schematic of the channel constraints. Therefore, channel SNR per modulation bandwidth is optimised by 'packing' the SNR within these two constraints, which is obtained by flattening the SNR across a particular modulation bandwidth.

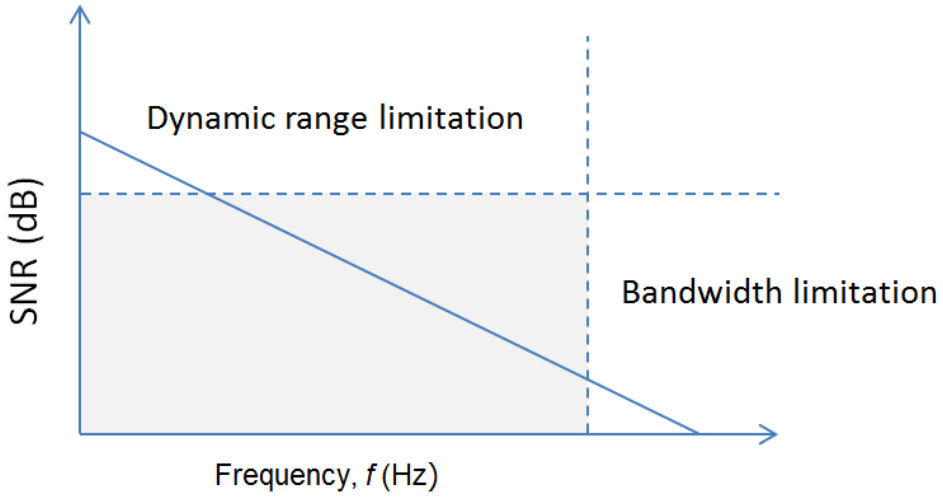

Figure 38. A simplified schematic of channel constrains.

A training run of the Pre-FDE equaliser is conducted using an iterative process as a form of a frequency-domain decision feedback equaliser. This is a nonlinear equalisation method that uses a previous detection decision to correct any nonlinear offset in the channel. The decision feedback equaliser is needed as the phase offset and SNR profile changes nonlinearly (with each iteration). This is because a change in the subcarrier load power results in a change in the statistical property of

the OFDM waveform, thus an iterative training run is conducted where the phase offset for each subcarrier is calculated and compensate for each run. This process continues until the variation of subcarrier SNR differences at the receiver converges to the lowest value *i.e.* the SNR for each subcarrier at the receiving end is the same within a pre-determined tolerance.

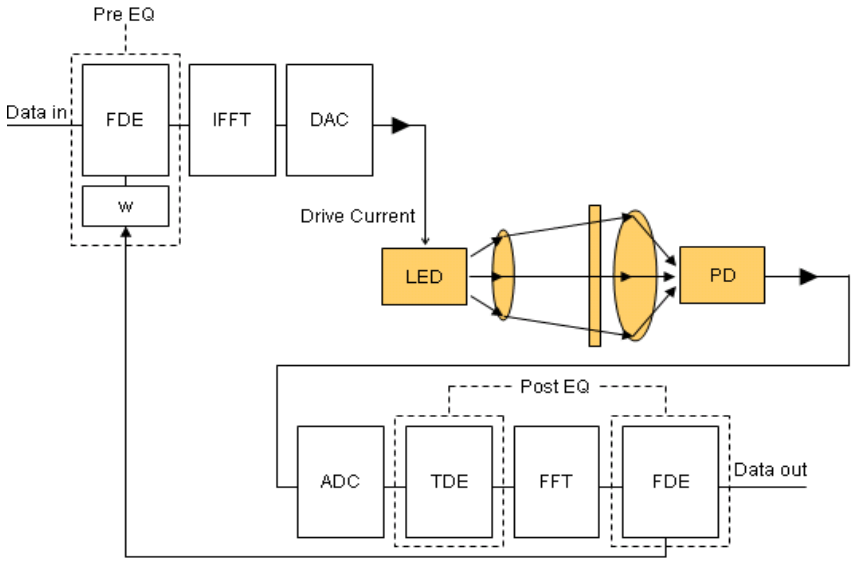

Figure 39. VLC OFDM system schematic including the complete end-to-end iterative equalisation modules.

Figure 39 shows a VLC OFDM system schematic including the complete end-to-end iterative equalisation modules. An initial training run is conducted and the received signal is equalized using the Post-TDE and transformed back to the frequency domain for the Post-FDE module. At this stage, the EVM is measured and from the EVM, the SNR for each sub-carrier and the average SNR of all the sub-carriers are obtained [18]. This SNR information is passed back to the transmitter for pre-equalisation. The Pre-FDE uses a weight multiplier w_n (where n is the subcarrier number) to change the amplitude and phase of each carrier before transmission. The optimisation proceeds by setting the Pre-FDE weights to an initial value, which can be unity, or a value based on previous

experiments. For each iteration, the weight multiplier is increased/decreased by a step-level coefficient, Δ if the SNR is less/more than the average SNR value.This iteration stops when the equilibrium condition of

$$\textit{subcarrier } SNR_n = \textit{average OFDM symbol } SNR_n \pm \textit{tolerance;}$$
$$\textit{for } n = 1, 2, \ldots N$$

is met.

A set of experimental measurements are conducted with the aim of investigating the convergence rate, which is the number of iterations required for the SNR equalisation to converge from an initial value of the weight multiplier $w_n = 1$. The experiment was conducted using the following method:

1. A set of 100 64-point DCO-OFDM frames was sent at ~200Mbps which corresponds to a 50MHz modulation bandwidth. Each frame transmits 4-QAM symbols on each of the 31 active subcarriers.
2. The EVM for each subcarrier was measured after Post-TDE and Post-FDE equalisation. The SNR for each subcarrier was estimated from the measured EVM.
3. Using Δ = 0.1, the Pre-FDE weight was adjusted from the initial value based on this SNR information.
4. The process was repeated and the weight is iteratively adjusted until the stop condition is met when the SNR for each subcarrier is equalised. The tolerance variance is set to 1dB.
5. The experiment was repeated using Δ = 0.5 and 0.01.

Figure 40 shows the gap between the highest and lowest SNR of the 31 subcarriers versus the number of iterations. The higher the step-coefficient, the faster the convergence rate; 10 iterations for Δ = 0.1, 35 iterations for Δ = 0.05, and 200 iterations (not shown in the figure) for Δ = 0.01. However, it can be seen that as a trade-off the higher step coefficient results in a higher SNR

variance at equilibrium. A step coefficient of 0.05 is selected for the rest of the pre-equalisation experiments, giving a reasonable compromise between convergence rate and SNR variance of the equalised subcarriers.

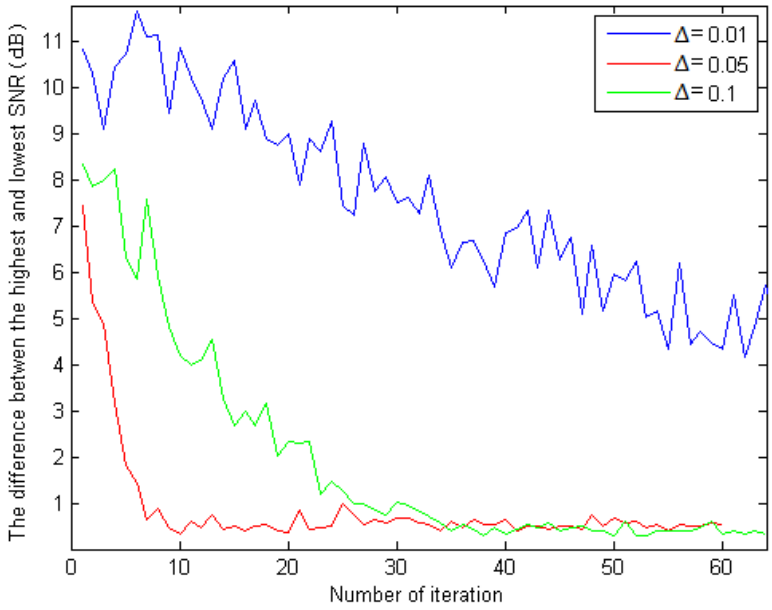

Figure 40. The difference between highest and lowest SNR versus number of iterations. Δ values = 0.01, 0.05 and 0.1.

An experiment was then conducted to obtain the subcarrier SNR for the VLC channel after the full end-to-end equalisation was applied. The experiment was conducted using the following procedure:

1. A set of 100 64-point DCO-OFDM frames was sent at ~100Mbps which corresponds to a 25MHz modulation bandwidth. Each frame transmits 4-QAM symbols on each of the 31 active subcarriers.
2. Using Δ = 0.05 the training run was conducted until the subcarrier SNR is equalised. The stop condition tolerance is set to 1dB.

3. The experiment was repeated with a modulation bandwidth of 50MHz, 75MHz and 90MHz.

Figure 41 shows the experimental estimated SNR for each subcarrier across a modulation bandwidth of 25MHz, 50MHz, 75MHz and 90MHz after the equalisation.

Table 8 summarises the results.

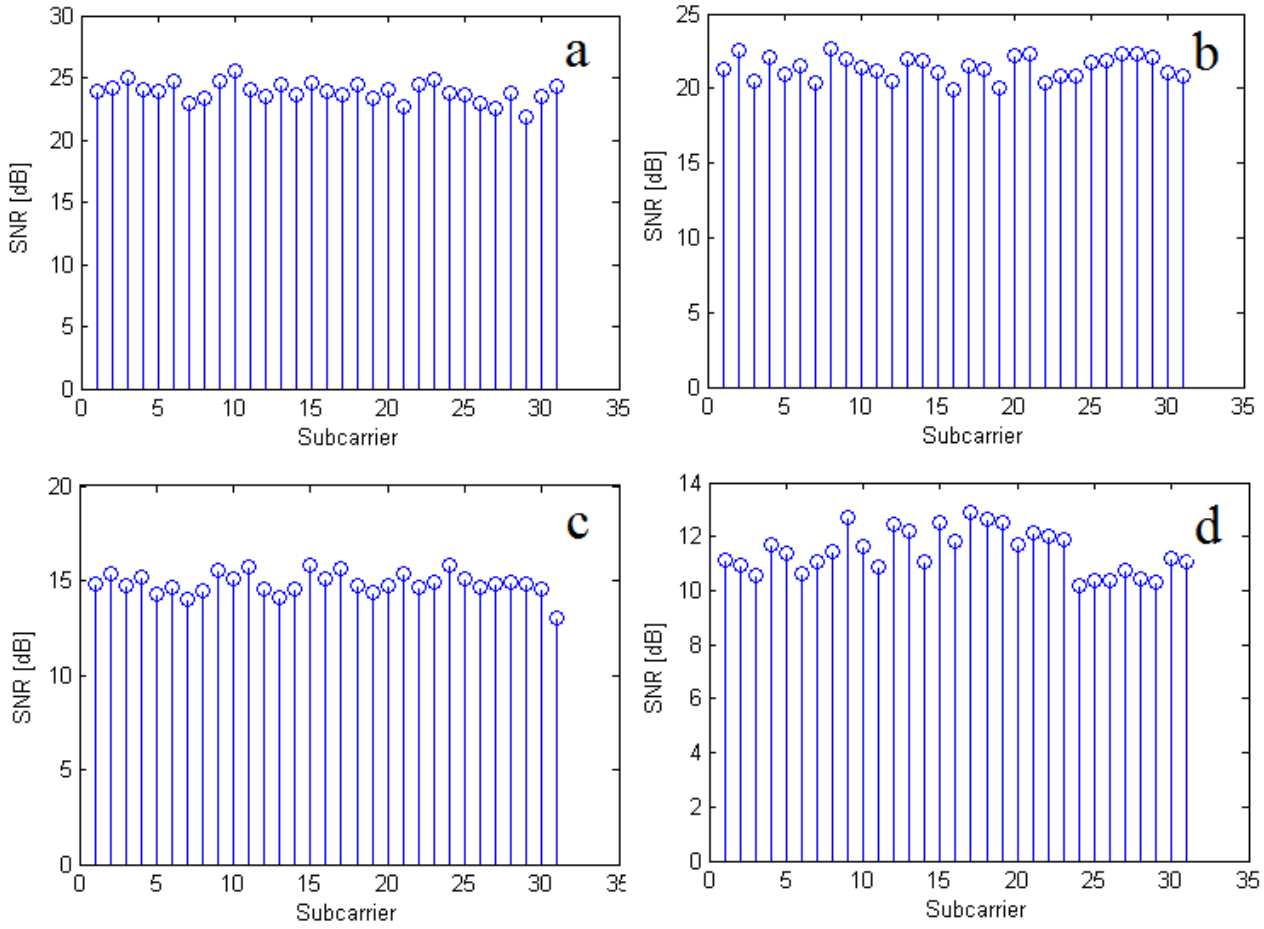

Figure 41. Subcarrier SNR estimation for DCO-OFDM transmission with modulation bandwidths of (a) 25MHz (b) 50MHz (c) 75MHz and (d) 90MHz.

Table 8. Modulation bandwidth versus average SNR

Modulation Bandwidth	25 MHz	50 MHz	75 MHz	90 MHz
Average SNR	*23dB*	*20dB*	*15dB*	*11dB*

It can be seen from this experiment that the method can be used to distribute the transmitted power to equalise the frequency response of the channel. With a flat SNR profile across the modulation bandwidth, the QAM modulation level can be adjusted accordingly to give the target BER.

It was also observed that the statistical properties of the OFDM waveform change when the equalisation method is applied. The following experiment was conducted to investigate this.

1. A set of 100 64-point DCO-OFDM frames was generated with a uniform load power for all subcarriers. Each frame transmits 16-QAM symbols on each of the 31-active subcarriers at a 50MHz modulation bandwidth.
2. The received time domain signal amplitude for each point in one OFDM frame is recorded and a probability density function of all amplitude points for 100 OFDM frames is derived.
3. The experiment was repeated using a load power based on weight parameters from the Pre-FDE training.

Figure 42 shows the probability density plots of the amplitudes of transmissions with and without pre-equalisation. It can be seen that the pre-equalised signal has a standard deviation of 0.0108 wheres the OFDM signal without pre-equalisation has a standard deviation of 0.0168. In a system with a limited dynamic range, the Gaussian distributed signal suffers from clipping noise due to signal clipping at the peak amplitudes *i.e.* the tail ends of the distribution. Thus, a higher OFDM signal standard deviation results in a greater probability that the signal is clipped due to the limited dynamic range, thus increasing the clipping noise incurred. Therefore, the pre-equalised signal is more robust towards clipping noise because it has a lower standard deviation.

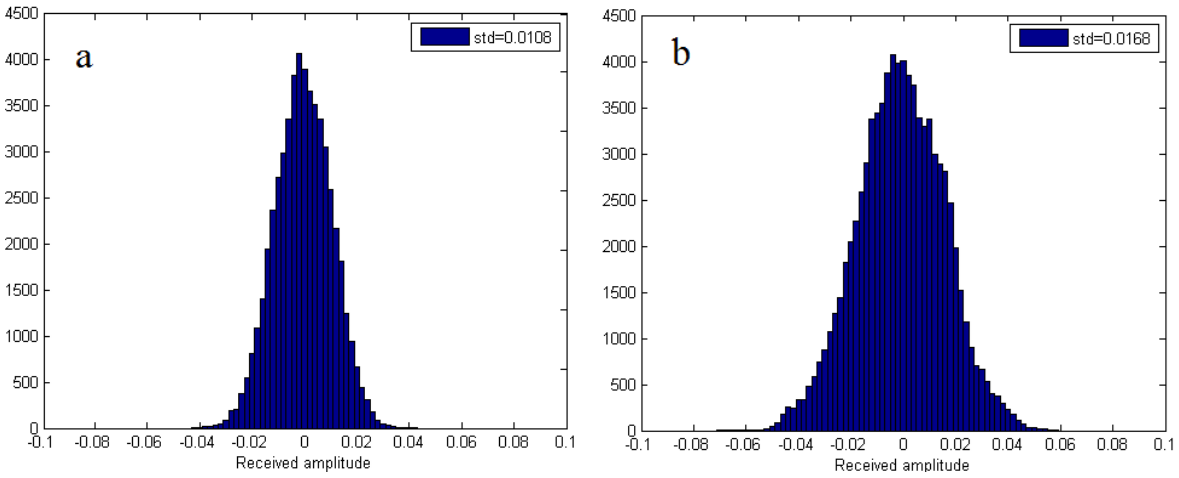

Figure 42. Probability density of the received random amplitude of the OFDM signal (a) with pre-equaliser and (b) without pre-equaliser.

3.4.5 Iterative equalisation bit-rate versus BER experiment

A bit-rate versus BER experiment is conducted with the aim of evaluating the performance of the end-to-end equalisation process. The experiment was conducted using the following procedure:

1. A set of 16-QAM DCO-OFDM frames was sent and the BER versus bit-rate was examined from 10Mbps to 350Mbps. 16-QAM is selected based on the available SNR from EVM measurement. The illumination level at the receiver was fixed at 460*lux*.
2. At each bit-rate point, a binary stream of 30,000 bits was tested. Transmission of 30,000 bits with zero error is represented as a BER of $1x10^{-4}$ on the graph.

The BER versus bit-rate curve is plotted and this is compared with the previous transmission without Pre-FDE equalisation. Figure 43 shows the BER versus bit-rate for transmission with full end-to-end equalisation and transmission without Pre-FDE equalisation.

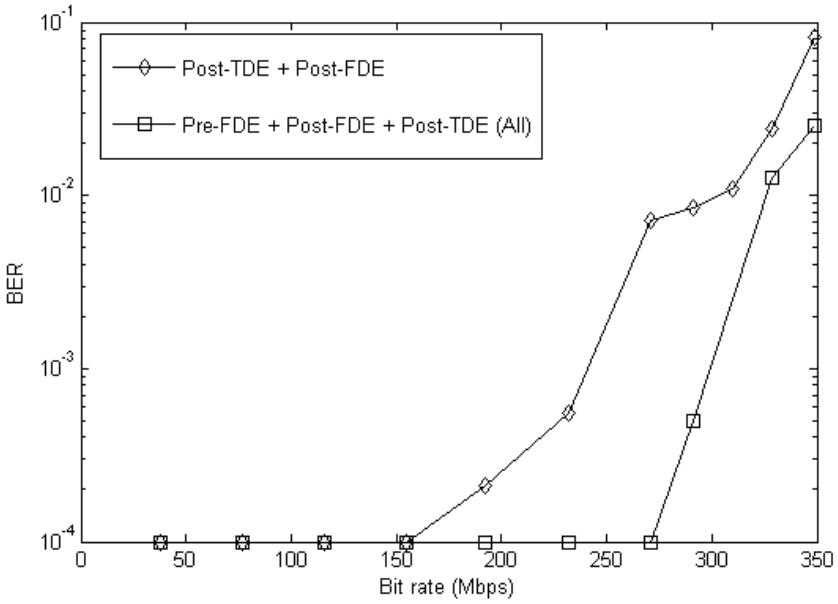

Figure 43. BER versus bit-rate for equalisation modules.

In comparison to the transmission without pre-equalisation, it can be seen that a bit-rate of ~310Mbps can be achieved using the additional pre-equalisation without exceeding the target BER. This corresponds to using a modulation bandwidth up to B = 85MHz. Based on this parameters, the theoretical maximum calculated using Shannon's capacity, $C = B\log_2(1+\mathrm{SNR})$ gives a bit-rate of 424Mbps, which gives the overall transmission ~75% bit-rates efficiency to the theoretical maximum.

The main constraint for bit-rate is the combined bandwidth of the LED and equipment used: the LED has a bandwidth of ~4.5MHz, the receiver has a bandwidth of ~40MHz, and the arbitrary waveform generator has a maximum bandwidht of 120MHz. The usage of a higher order modulation (64-QAM for example) to reduce bandwidh requirements is constrained by the dynamic range of the receiver, which results in a limited channel SNR. Figure 44 shows the comparison

between the received constellation for the case of a fully equalised (pre and post) and time-domain equalised transmission at ~310Mbps.

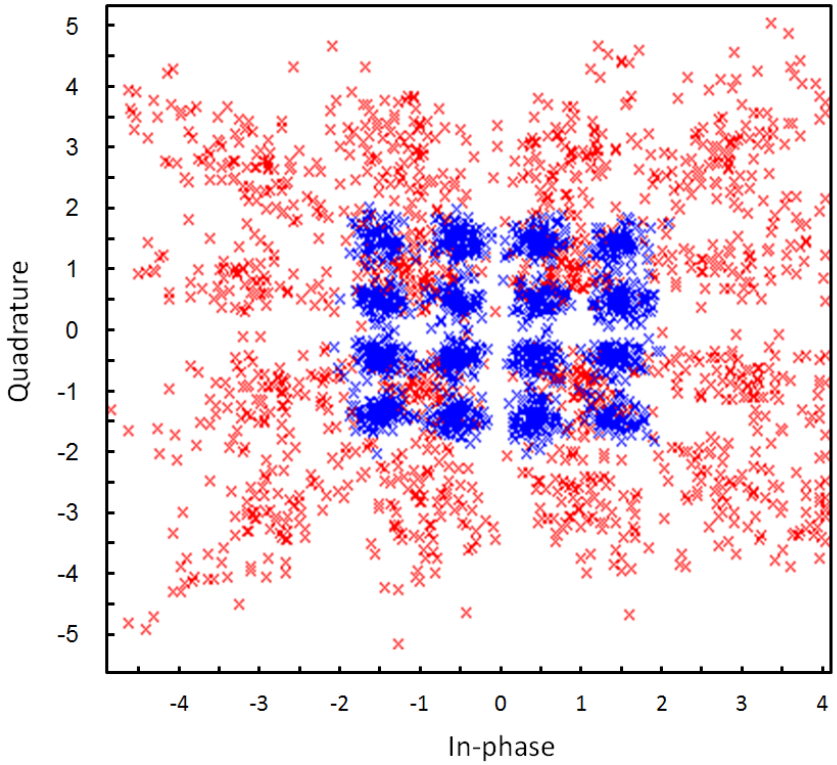

Figure 44. A comparison between fully equalised constellation (blue) and only time-domain equalised (red).

3.4.6 OFDM equalisation summary

In this section, an OFDM equalisation method is presented as a potential solution in optimising transmission rates by using the available SNR to compensate the limited channel bandwidth and dynamic range. A set of experimental transmissions are conducted to investigate characteristics of the VLC channel and the transmission performance, and the main components of the equaliser are summarised as follows:

1. Post-TDE equalisation mitigates signal synchronisation problems, which exist because the high frequency component of the received signal is highly attenuated due to the channel frequency response.
2. Post-FDE equalises the deterministic subcarrier phase offset and normalises the subcarrier magnitude. From this, a Gaussian distributed constellation is achieved and an EVM measurement is performed to estimate the subcarrier SNR.
3. Pre-FDE adjusts the power allocated to each subcarrier based on subcarrier SNR information. This adjustment is done iteratively until the SNR for all subcarriers are equalised.

A transmission bit-rate of up to ~310Mbps is achieved under the target BER of $2x10^{-3}$. This corresponds to a modulation bandwidth of ~85MHz, which shows the outstanding performance of the OFDM system in transmitting high-speed data far beyond the channel bandwidth of ~4.5MHz. Next, an investigation into signal clipping due to limited dynamic range is presented.

3.5 Systematic clipping as a method to increase performance

Signal clipping is a form of nonlinear effect that exists in VLC links and several studies have been conducted to characterise this effect [57, 85, 86]. The random Gaussian-distributed nature of OFDM signals exhibit high peak-average power ratio (PAPR) with randomly-occurring large peaks. Therefore, normalising the peak-to-peak amplitude to fit the dynamic range of a VLC system results in a reduction in the average transmitted power due to this high PAPR. Systematic clipping of the large peaks at signal generation has been applied as a method to improve power efficiency [26].

Clipping at the tail ends of Gaussian-distributed OFDM signal amplitude introduces additional clipping noise to the received signal [59]. However, experiments conducted in [26] demonstrated that signal clipping is beneficial as a compression method that allows a higher signal power to be transmitted which outweighs the effect of the clipping noise.

In this section, a clipping experiment is designed using clipping parameters similar to the work conducted in [26]. A set of time domain OFDM signal frames are collected and from this sample the standard deviation and variance are averaged. The variance of a single frame is obtained by

$$\left\langle x^2 \right\rangle = 2\sum_{n=1}^{2N} \left\langle X_n^2 \right\rangle = 2P \tag{50}$$

where X_n is the amplitude of the n^{th} point of the 64-point IFFT output, and P is the transmitted power. The clipping level (CL) is defined by

$$CL = 20\log\left(\frac{|x_c|}{\left\langle x^2 \right\rangle}\right) \tag{51}$$

where x_c is the clipping limits. A pseudo-unclipped case is obtained using $x_c = 6.3\sqrt{2P}$ which corresponds to CL = 16dB.

A bit-rate versus BER experiment was conducted to evaluate systematic clipping as a method to improve the BER of DCO-OFDM transmission. The experiment was conducted by sending a set of 16-QAM DCO-OFDM frames at 300Mbps. The BER versus CL is examined for CL = 2dB to 16dB. At each CL point, a binary stream of 30,000 bits is tested. Figure 45 shows the systematic clipping level versus BER. The transmission is optimised by applying the equalisation method at each clipping level.

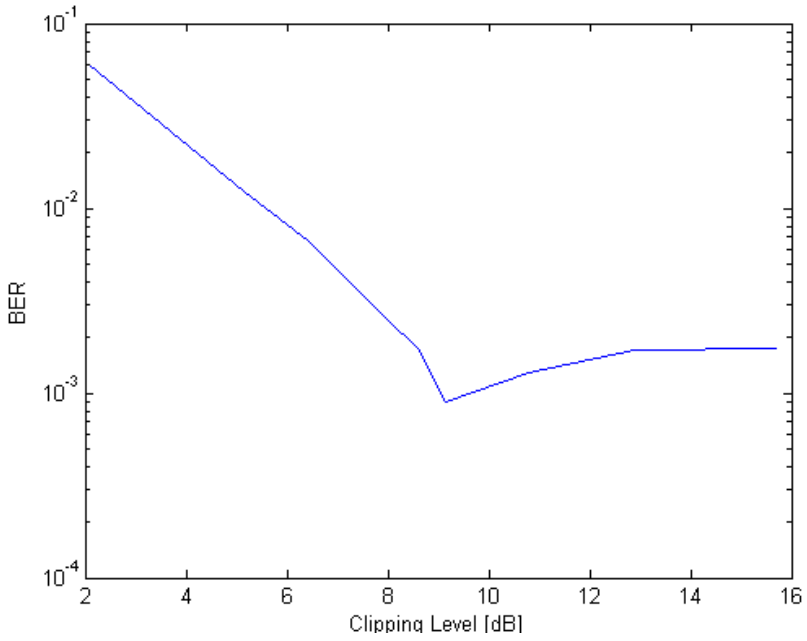

Figure 45. Systematic clipping level versus BER for 16-QAM DCO-OFDM at transmission bit-rates of 300Mbps.

At a clipping level = 2dB (a high amount of clipping), the received signal is dominated by clipping noise which results in a high BER. As the clipping level increases (less of peak amplitudes are clipped), the BER improves to an optimum clipping level of 9dB where a BER = $1x10^{-3}$ is recorded. For clipping levels higher than 9dB, the BER starts to degrade slightly.

It can be seen from these results that systematic clipping demonstrates a slight improvement in practice. This result matches with the clipping experimental result conducted in [26], for which only a marginal increase in BER/bit rates improvement in the experimental measurements as compared with a higher SNR gain in a clipping simulation conducted in the same investigation. This is because the clipping noise in the conducted simulation is assumed to be lower than the actual clipping noise that occurred in a practical bandwidth-limited system.

It can be concluded that systematic clipping in a practical bandwidth-limited system only results in marginal improvements in SNR because the gain in power efficiency is counteracted by the clipping noise. Therefore, in the following experiments, systematic clipping is not applied in the OFDM signal transmission.

Further increase in the transmission bit-rates can be achieved by increasing the overall signal power, which corresponds to the available illumination level in the room. In the following experiment, an investigation into the relationship between indoor illumination level and transmission bit-rates is presented.

3.6 Illumination level versus bit rate

The transmission bit-rates optimisation of a single channel VLC OFDM transmission at a fixed illumination level has been presented and discussed. In this section, an investigation is conducted on improving bit-rates by increasing the illuminations level.

The experiment is conducted by sending a set of 16-QAM DCO-OFDM symbols at illumination levels from 10*lux* to 2000*lux*. The illumination level is varied by changing the distance between the transmitter and receiver. At each illumination level point, a binary stream of 30,000 bits is sent and the bit-rate at the target BER of $2x10^{-3}$ is recorded.

Figure 46 shows illumination level versus bit-rate for a 16-QAM DCO-OFDM transmission at the target BER of $2x10^{-3}$. The level of illumination is proportional to the level of optical received signal power for a fixed transmission power, thus it can be seen that the bit-rate rises as the illumination level (and signal power) increases from 20*lux* to 500*lux* and peaks at ~310Mbps. The bit-rate then

decreases as the illumination increases beyond this level. This is because the transmission is constrained by the receiver's dynamic range which results in clipping of the OFDM waveform peak amplitudes.

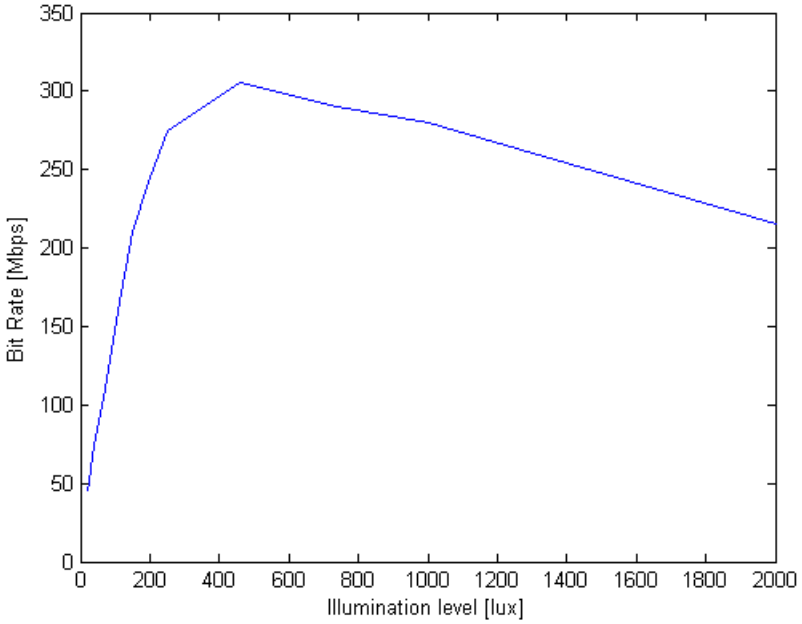

Figure 46. Illumination level versus bit rate for 16-QAM DCO-OFDM at BER of 2×10^{-3}.

This experiment shows the relationship between the illumination levels of a single transmitter and the achievable bit rates for the OFDM transmission. At low illumination levels, the transmission rates are constrained by the available signal power. High illumination levels result in the saturation of the receiver, which shows a drop in the overall transmission rates due to the increasing clipping noise.

3.7 Conclusions

This chapter presented an investigation into higher-order modulation schemes using OFDM as a method to overcome channel limitations and improve VLC transmission bit rates. A practical

demonstration of high-speed VLC transmission is presented and a development of an OFDM equalisation method to optimise transmission bit-rates is discussed.

The equalisation method combining frequency and time-domain equalisation maximises bandwidth efficiency by equalising the subcarrier SNR, as well as reducing bit-error rate by correcting phase offsets. In the experiments conducted, transmission bit-rates of up to ~310Mbps are demonstrated at a 1m range and 460*lux* illumination level for a single channel link. This particular transmission corresponds to a modulation bandwidth of 85MHz, which shows the outstanding performance of the OFDM system in transmitting high-speed data beyond the channel -3dB bandwidth of 4.6MHz.

Systematic clipping demonstrated an improvement in reducing the BER for the OFDM transmission conducted. In the experiments conducted an increase in power efficiency only results in a marginal increase in transmission bit-rates/BER performance, which shows that increasing transmission bit-rates of this system is limited by the available bandwidth.

The transmission bit-rate increases as the illumination level increases. This is however limited at a point where the signal is clipped due to dynamic range, which causes the bit error-rate to increase due to the additional clipping noise.

Chapter 4

Alternative Optical OFDM Approaches

4.1 Introduction

Previous chapters have presented investigations of OFDM VLC in single-channel using the DCO-OFDM modulation scheme. In this chapter, several alternatives to DCO-OFDM are investigated as a potential modulation scheme in VLC system.

As described in Chapter 1.4.3, the bipolar OFDM signal can be made unipolar by several ways. The DCO-OFDM scheme operates by adding a DC-bias to the bipolar signal to make it positive to fulfil the IM/DD requirement. However, this incurs an additional power requirement due to the dc-bias current applied. Several methods have been introduced as a power-efficient alternative to the DCO-OFDM approach at a cost of reduced bandwidth efficiency.

One such method, ACO-OFDM is a well-known alternative to the DCO-OFDM scheme, in which the bipolar OFDM signal is made unipolar by clipping the signal at zero *i.e.* removing negative parts of the signal. Only the positive real parts of ACO-OFDM waveform are sent for transmission. This offers higher signal power efficiency. Theoretical comparison with DCO-OFDM has demonstrated that except for extremely large constellations, ACO-OFDM requires lower optical power for a given BER and data rate than DCO-OFDM [87].

Several other variants of asymmetrical OFDM scheme have also been developed to improve the efficiency of ACO-OFDM [88-90]. An advanced receiver ACO-OFDM design in [65] shows an

improvement, by approximately halving the noise variance by using maximum likelihood detection at the receiver. Unipolar OFDM (U-OFDM) [66] transmits the positive and negative halves of the DCO-OFDM signal in two separate parts in series, and uses a similar receiver design as the advanced receiver ACO-OFDM scheme to reduce noise variance.

Nevertheless, the experimental performance of ACO-OFDM and other variants of the asymmetrical power-efficient schemes have never been reported, to the best of the author's knowledge. This chapter presents an investigation into transmission of these schemes using the VLC system under consideration.

4.2 Asymmetrical OFDM signal generation

A general characteristic of the asymmetrical scheme is that the waveform is generated in such a way that the negative part is omitted without losing any information. The signal generation of some of the asymmetrical schemes are described in the following sections.

4.2.1 ACO-OFDM scheme

The ACO-OFDM scheme loads the useful information bit on the even subcarriers while leaving the odd subcarriers unmodulated. Therefore, only $N/2$ subcarriers carry data symbols out of the $2N$-IFFT points in one OFDM frame. Figure 66 shows a schematic of ACO-OFDM signal generation. Figure 66(a) shows an example of an ACO-OFDM subcarrier assignment in the frequency domain and Figure 66(b) shows the corresponding time-domain IFFT output. The resulting IFFT time-domain output waveform has a negative part that is a symmetrical copy of its positive part. This

negative part is then omitted by clipping the signal at zero as shown in Figure 64(c), thus only transmitting the positive part.

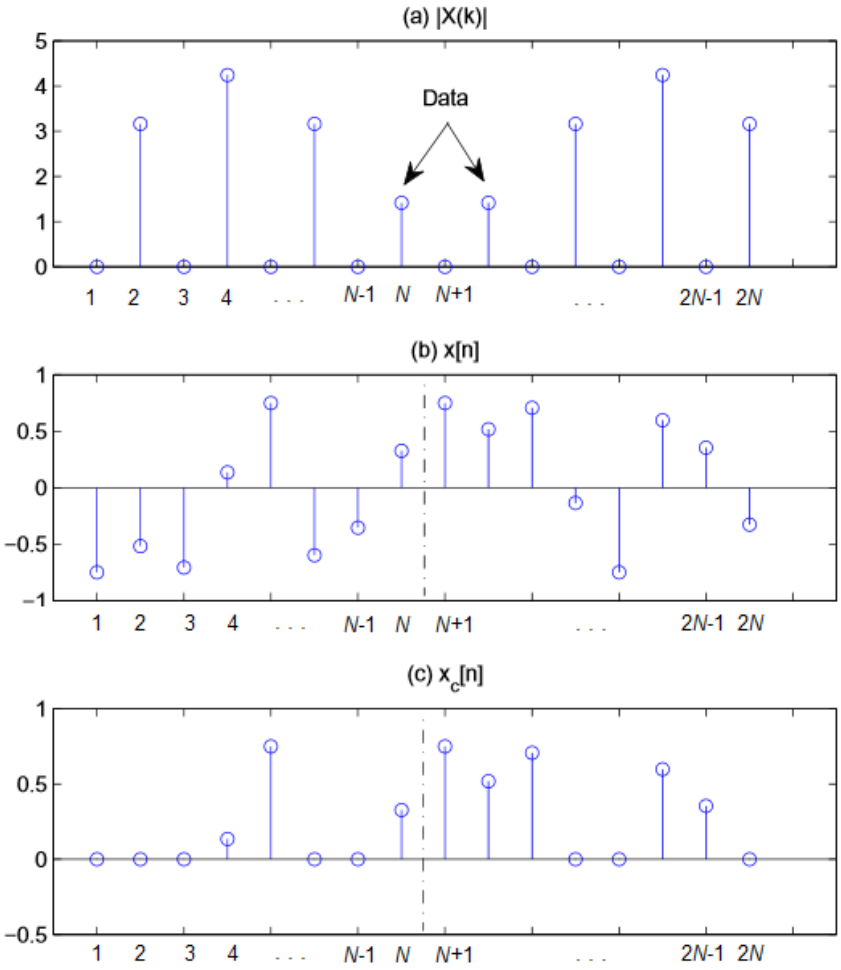

Figure 47. ACO-OFDM signal generation: (a) data is loaded onto even subcarriers in the frequency domain, (b) the resulting time-domain output of the IFFT has a positive part that is an anti-symmetrical copy of the negative part and (c) the negative signal is clipped at zero.

At the receiver, the time-domain waveform is sent to the FFT algorithm, and only even subcarrier symbol outputs are passed for symbol detection and odd subcarriers symbol outputs are omitted. The gross data rate for an ACO-OFDM transmission is

$$R_{ACO-OFDM} = \frac{B}{N}\sum_{k=1}^{N/2}\log_2 M_n. \quad (52)$$

4.2.2 Advanced Receiver ACO-OFDM scheme

It can be seen from Figure 66(c) that each clipped point has a corresponding amplitude pair that carries data signal *i.e.* point n and point $N+n$ form a signal pair, for n = 1, 2, …, N. At the receiver, both clipped point and its corresponding amplitude pair are corrupted by additive white Gaussian noise (AGWN).

Using an advanced receiver design demonstrated in [65], the received ACO-OFDM noise variance is reduced by fixing the clipped point of the received waveform to zero. This is done using a simple pairwise maximum likelihood (ML) detector that detects a point with a lower amplitude in the signal pair and this point is fixed to zero. The ML decision of subcarrier number, n is described using the following algorithm:

for n = 1, 2, 3... N
if $n > N+n$
$N+n = 0;$
else
$n = 0;$

This process is repeated for every point in the time-domain OFDM symbol before the FFT process.

4.2.3 Unipolar OFDM (U-OFDM) scheme

The U-OFDM method uses the DCO-OFDM signal generation scheme, in which all subcarriers are loaded with complex data symbols. However, the positive and negative parts of the IFFT output are sent in two separate frames, thus this method requires double the time-period of a single DCO-

OFDM frame. Therefore, this method exhibits half the bandwidth efficiency of DCO-OFDM which is the same as the bandwidth efficiency of the ACO-OFDM.

Similar to the advanced- receiver ACO-OFDM, each point on the positive part has a corresponding point on the negative part. A pairwise ML detection and correction is performed at the U-OFDM receiver to reduce the noise variance.

4.3 BER versus bit-rate experiment

In this section, a BER versus bit-rate experiment for ACO-OFDM, advanced receiver ACO-OFDM and U-OFDM scheme is reported. First, a single-channel transmission experiment is conducted using the transmission system setup as described in Section 3.3.

Signal clipping of the asymmetrical waveform is conducted digitally. The clipped asymmetrical waveform is then sent to the AWG for digital-to-analogue conversion. The AWG operates in such a way that the output waveform is bipolar with a zero mean value. This is to allow full usage of the AWG modulation amplitude dynamic range. Because of this, a 135mA dc-bias current is added to ensure that the waveform is positive.

An experiment was conducted to evaluate the BER versus bit-rate performance for the various OFDM approaches. For each case, the BER is collected from 30,000 bits that are transmitted using 16-QAM symbols, at bit rates between 20Mbps to 350Mbps. For all cases, the OFDM signal occupies the same modulation amplitude range. The illumination level at the receiver plane is measured.

4.3.1 Baseline wander

From the experiment, it is observed that the ACO-OFDM signal suffers from baseline wander. This is caused by the asymmetry of the clipped ACO-OFDM signal. Figure 67 shows two instances of time domain waveform of ACO-OFDM signal, at a modulation bandwidth of 10MHz and 90MHz. It can be seen that the axis of the received and transmitted ACO-OFDM signal is not aligned due to baseline wander. Further to this, it was observed that the other two cases of asymmetric OFDM signal *i.e.* the Advanced Receiver ACO-OFDM and U-OFDM suffer from the same effect. This is caused by the changing average of the asymmetric signal. It is an open question whether this baseline wander is related of the number of subcarriers. Although based on central limit theorem that a higher number of subcarriers reduce the moving average, the length of the time-domain signal frame is however increases due to lower subcarrier frequency spacing. The investigation into this area is beyond the scope of this work, and will be included in future studies.

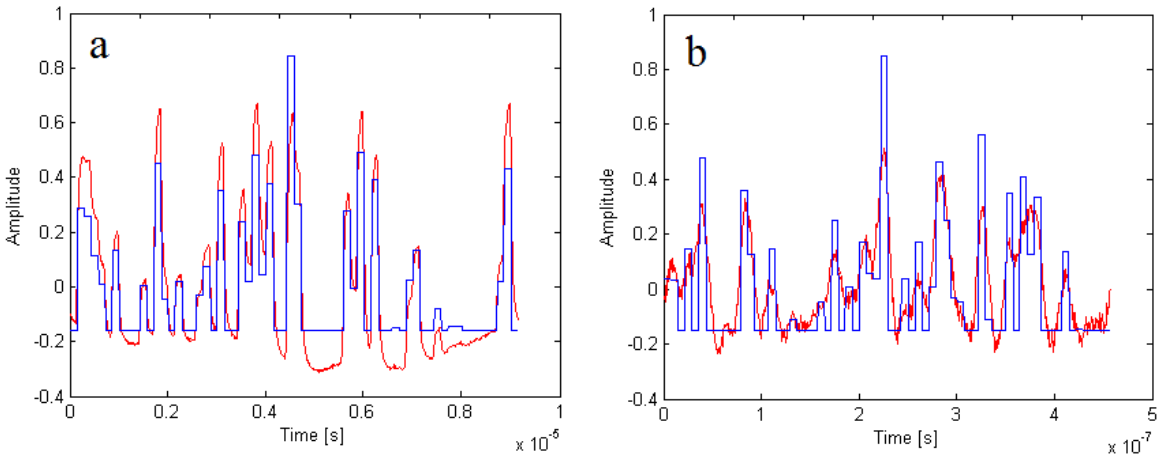

Figure 48. Received (post-equalised) time-domain waveform of ACO-OFDM modulation (red) is plotted onto the generated time-domain waveform (blue) at (a) 10MHz and (b) 90MHz modulation bandwidth. The figure retains the axis of the generated waveform that is normalised to a zero-mean amplitude value, which explains the negative amplitudes.

To counteract the effect of baseline wander due to the asymmetrical waveform, a modified ACO-OFDM scheme is introduced where instead of clipping the waveform at zero; an unclipped ACO-OFDM signal is transmitted. This scheme is termed dc-biased ACO-ODFM. Figure 68 shows a schematic of a dc-biased ACO-OFDM waveform generated based on the ACO-OFDM signal in Figure 66(b). The signal is generated using the same method as described in Section 5.2.1, but instead of clipping the negative part (see Figure 66(c)), a dc-bias current is added to the unclipped ACO-OFDM waveform to make it positive.

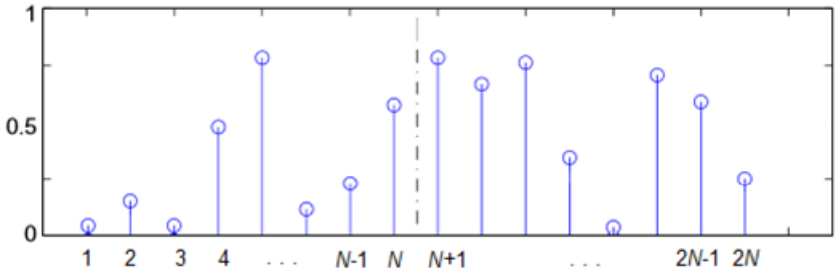

Figure 49. A unipolar signal is achieved by adding a dc-bias to the waveform in Fig. 3(b) instead of signal clipping at zero.

Although a dc-bias is added, this scheme gains a 3dB power advantage over DCO-OFDM by sending the signal twice: by transmitting both halves of the anti-symmetrical signal (positive and negative parts) in one frame. The signal follows a Gaussian distributed amplitude. The bandwidth efficiency of this method remains the same as the conventional ACO-OFDM.

4.3.2 BER versus bit-rate results

The BER versus bit-rate curves for all five cases are plotted for comparison and these are shown in Figure 69. The Illumination level is measured at ~250*lux*. As a comparison, the BER versus bit-rate result for the DCO-OFDM scheme is also included. It can be seen from Figure 69 that the

bandwidth-efficient DCO-OFDM scheme performs better than the rest of the power-efficient schemes, achieving ~305Mbps at the target BER. On the other hand, the U-OFDM and Advanced Receiver ACO-OFDM (AR-ACO on diagram) cases perform worst. In theory these should deliver higher bit-rates than the conventional ACO-OFDM scheme because of the noise improvement achieved using the ML detection in the receiver design. However, the base axis of the received signal is not flat due to baseline wander and the ML detection sets the base axis of the signal to zero (as described in Section 4.2.2). This causes additional distortion to the signal waveform, which result in a transmission with high BER.

The dc-biased ACO-OFDM scheme (dc-ACO on diagram) performs better than the rest of the power-efficient cases. This shows that this scheme is robust to baseline wander due to the symmetry of its waveform. A bit rate of ~180Mbps is achieved for the dc-biased ACO-ODFM case while the conventional ACO-OFDM scheme achieves a bit rate of ~150Mbps.

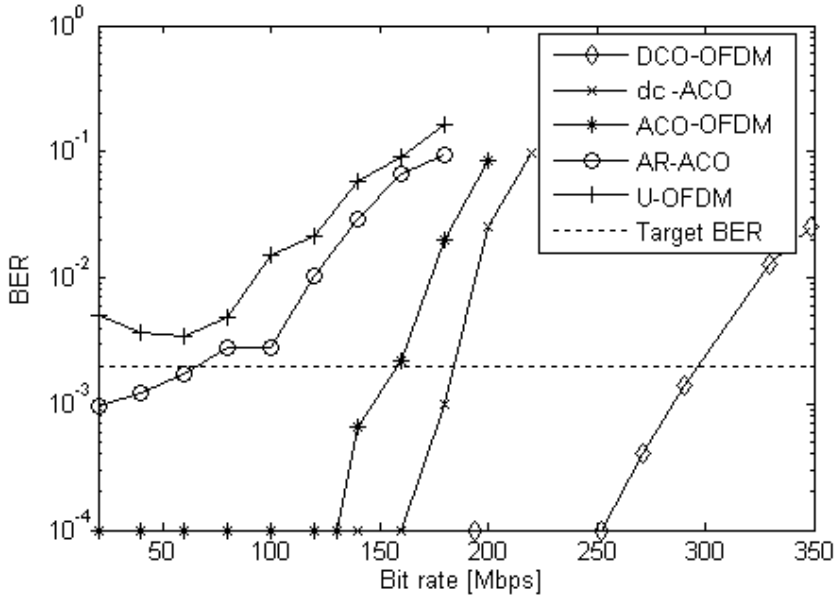

Figure 50. Experimental BER versus bit-rate curves for different optical OFDM schemes.

4.3.3 Power-efficient versus bandwidth-efficient scheme

For a fair comparison between the power-efficient and bandwidth-efficient schemes, without taking account the effect of baseline wander, this discussion focuses on dc-biased ACO-OFDM and DCO-OFDM.

Figure 70 shows the estimated post-equalised subcarrier SNR obtained from EVM measurements for both schemes at a modulation bandwidth of 50MHz. Figure 71 shows the corresponding signal constellation for both cases.

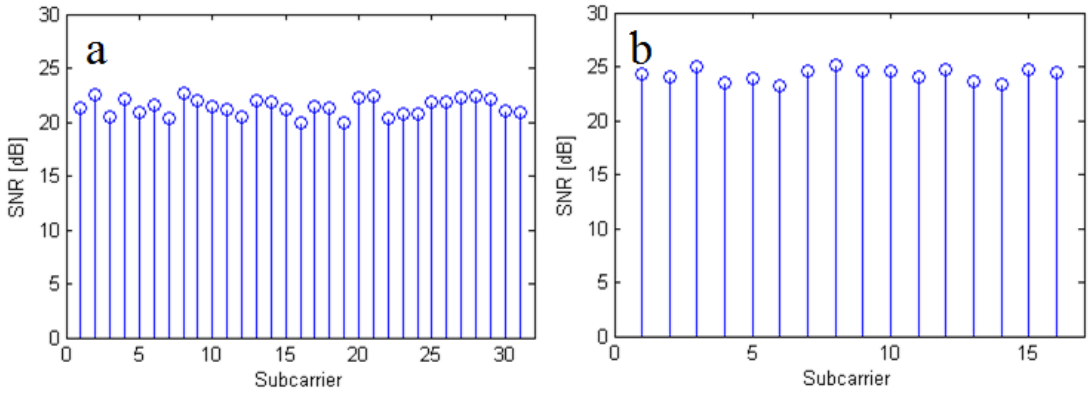

Figure 51. Estimated subcarrier SNR from EVM measuremens for (a) DCO-OFDM and (b) dc-biased ACO-OFDM schemes.

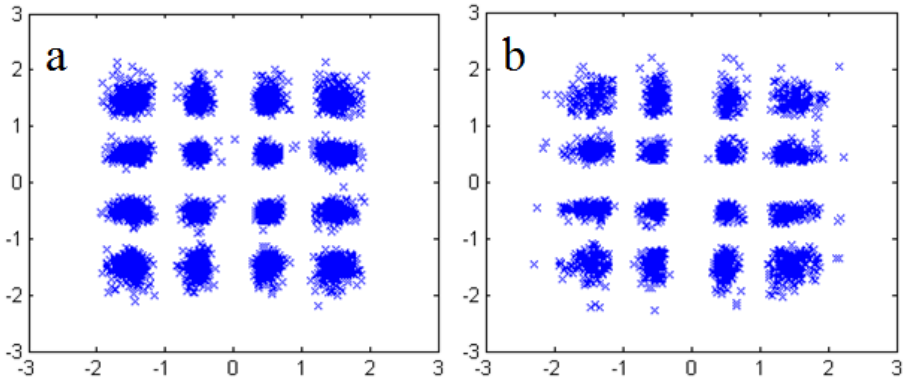

Figure 52. QAM constellations for DCO-OFDM (a) and ACO-OFDM (b) at 50MHz.

It can be seen from Figure 70 that the dc-biased ACO-OFDM has an average subcarrier SNR of ~24dB, whereas the DCO-OFDM has an average of ~21dB. This ~3dB increase in SNR is because the dc-biased ACO-OFDM signal is sent twice in one frame. Figure 72 shows the modulation bandwidth used to achieve the bit-rates shown in Figure 69 for the DCO-OFDM and dc-biased ACO-OFDM schemes. It can be seen that because of the higher SNR, dc-biased ACO-OFDM occupies modulation bandwidths of up to ~90MHz before exceeding the target BER, whereas the DCO-OFDM exceeds the target BER at ~75MHz. This result shows dc-biased ACO-OFDM scheme has more than half of transmission bit-rate of the DCO-OFDM scheme despite only having approximately half the bandwidth efficiency. However, for transmission in a bandwidth-limited system, the bandwidth efficiency advantage of DCO-OFDM outweighs the power-efficiency of dc-biased ACO-OFDM to give a higher overall bit-rate.

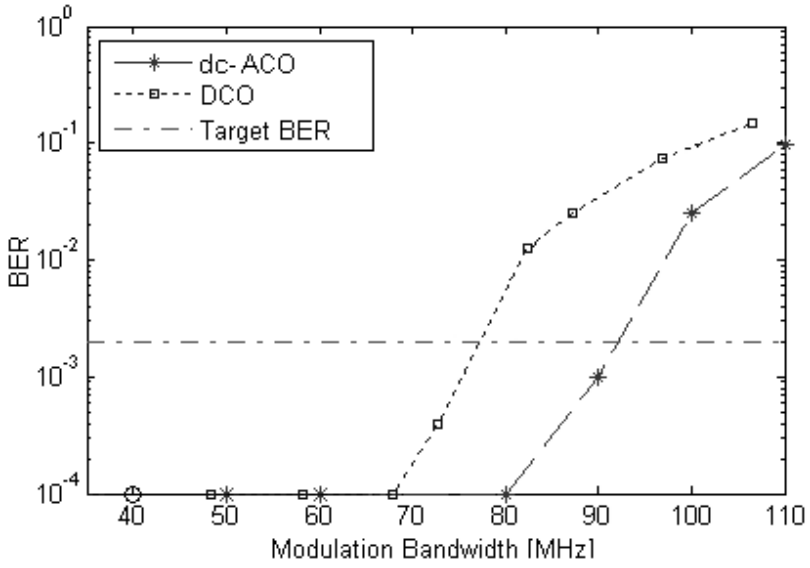

Figure 53. BER versus modulation bandwidth used to achieve the bit-rates shown in Figure 69 for the DCO-OFDM and dc-biased ACO-OFDM schemes.

4.4 Conclusions

This section presents an experimental comparison of the performance of bandwidth-efficient DCO-OFDM scheme and several power-efficient asymmetrical OFDM schemes.

In practical transmission cases, asymmetrical OFDM schemes suffer from the effect of baseline wander, which results in severe bit-rate degradation. To our knowledge, this is the first time that this has been reported. This result introduces a severe constraint on the asymmetrical OFDM approach.

To counteract, dc-biased ACO-OFDM is introduced to evaluate this effect in a symmetrical transmission. This is not a novel communication scheme, rather to provide a condition that is robust to baseline wander to demonstrate the performance of ACO-OFDM as an alternative power-efficient approach. A single-channel transmission using this scheme achieves transmission rates of up to ~180Mbps.

Although dc-biased ACO-OFDM has approximately half of the bandwidth efficiency of DCO-OFDM, this scheme offers 3dB gain in signal power. However, for signal transmissions in a bandwidth-limited system, the bandwidth efficiency advantage of DCO-OFDM outweighs the power advantage of dc-biased ACO-OFDM giving a higher overall bit-rate.

Nevertheless, the primary function of VLC communications system to provide the required room illumination requires a constant level of illumination. The dc level is necessary to ensure the illumination level is fixed despite no data is transmitted. For this, the integration of dc level has to be considered in selecting or designing the suitable modulation scheme for VLC systems.

Chapter 5

VLC Systems using Imaging MIMO-OFDM

5.1 Introduction

In the previous chapters, the constraints of single-channel VLC transmission are examined and the performance of an optimised single channel transmission using the ACO-OFDM and DCO-OFDM modulation schemes at a specific illumination level is discussed.

The DCO-OFDM scheme is demonstrated to be effective in combating the effect of limited bandwidth by using time- and frequency-domain equalisation methods to optimise the transmission bit-rates. However, from the single-channel transmission it can be seen that ultimately the dynamic range of a system limits the overall achievable transmission rates.

The inherent availability of multiple transmitter sources in typical VLC configurations offers the potential of implementing a multi-input multi-output (MIMO) transmission system. MIMO transmission offers a linear capacity gain with the increase in the number of channels in an ideal crosstalk-free configuration. In such a system, the optical power from multiple sources is directed onto multiple detectors, creating an independent, crosstalk-free channel for each transmitter-detector pair. In this case, power is divided between multiple channels, thus mitigating the dynamic range problem.

Several MIMO transmission systems have been discussed in Section 1.4.4. One such system, the imaging diversity MIMO uses an imaging lens to create a full rank channel matrix. For this, the

optical power at the receiver plane is separated using an imaging lens and directed onto multiple detectors. Figure 47 shows a schematic of such a system.

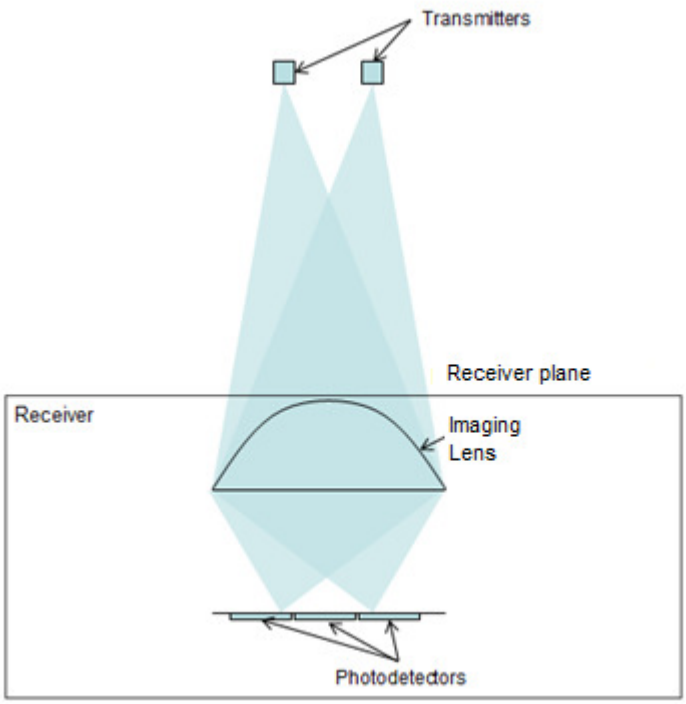

Figure 54. Schematic showing an imaging MIMO system.

This chapter presents an investigation into using an imaging MIMO system as a method to further increase bit-rates. An imaging-diversity MIMO-OFDM VLC prototype is built, and configurations of the system are described. Experimental analysis is conducted to investigate the performance of the system.

5.2 VLC MIMO-OFDM system overview

The imaging MIMO-OFDM system developed is a 4x9 MIMO system, which consists of 4 transmitter (Tx) units, an imaging lens and a 9-detector MIMO receiver. The 4-channel transmitter is deemed adequate for this MIMO analysis. Increasing the number of Tx unit will require additional signal processing equipment that is beyond the budget and scope of this work.

Each Tx unit represents an independent channel which transmits OFDM signals. This is detected by the MIMO receiver. Figure 55 shows a block diagram of the system.

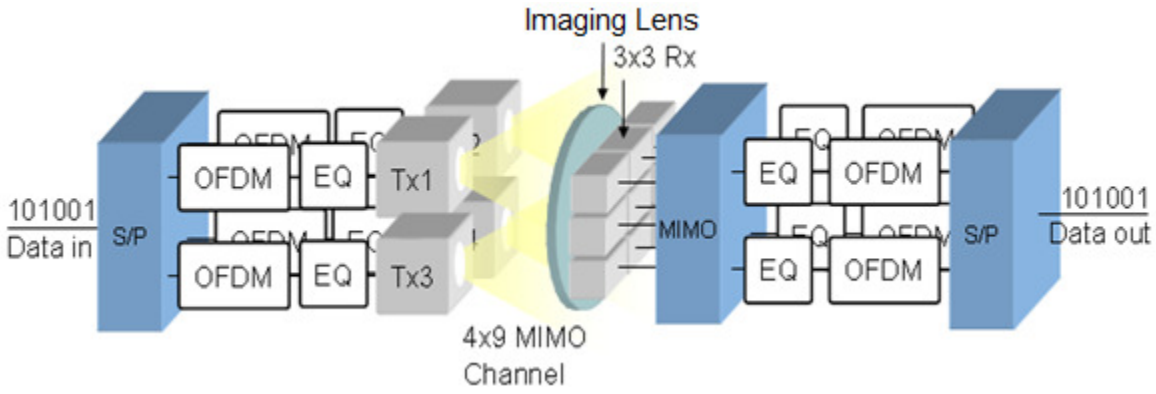

Figure 55. MIMO-OFDM system block diagram.

The system is based on the single-channel transmission system described in Section 3.2. The single-channel transmission system is replicated, forming four channels. Each channel consists of a Luxeon Star-C LED LXHL-MW1B fitted with an optical diffuser FRAEN FHS-HMB1-LL01-z. The optical diffuser has a 5° half-power semi-angle, $\Phi_{1/2}$, which is selected to provide high illumination level at the receiver plane at the cost of a narrow field-of-view. The Tx unit is arranged in a 2x2 grid. The separation between transmitter channels is varied. Figure 49 shows the MIMO transmitter setup.

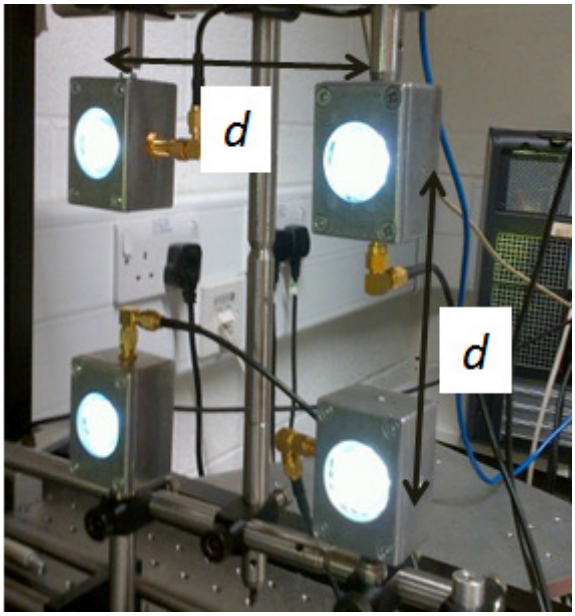

Figure 56. MIMO transmitter setup consists of 4 Tx units.

Data signal generation and processing is done offline using MATLAB software. A binary data signal is generated and encoded digitally into OFDM symbols. This is then split into four Tx channels. For each Tx channel, signal generation and encoding is the same as the previous OFDM system described in Section 3.2.

For this MIMO system, two Agilent 81150A two-channel waveform generators are used. For each Tx channel, the OFDM symbols are routed from a computer to each AWG input for digital-to-analogue conversion. Each LED is driven by a 135mA DC-bias current and for each Tx channel the bias current is combined with an electrical output of the respective AWG outputs using a bias-T. This signal is then transmitted using the Luxeon Star-C LED across the VLC channel and detected at the receiver. The data signal travel across the LOS channel to the optical receiver (Rx). Figure 57 shows the receiver setup.

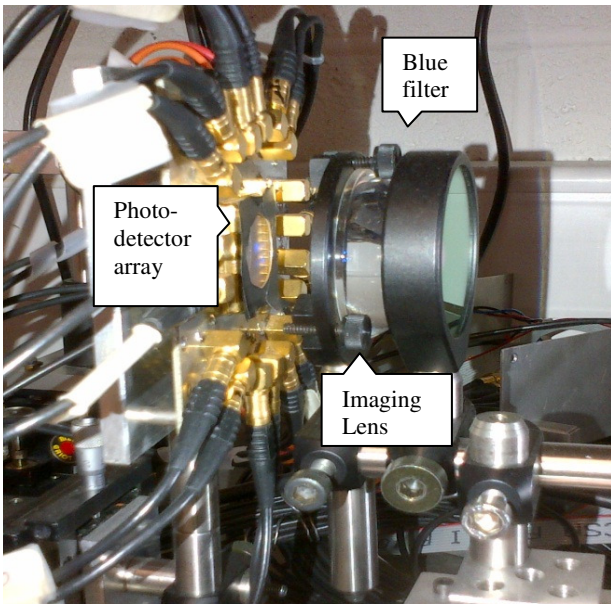

Figure 57. MIMO receiver setup.

The Rx consists of nine photo-detectors arranged in a 3x3 grid. It is fitted with a Melles-Griot MG 520-A blue filter and the aspherical concentrator as previously described in Section 2.3 is used as an imaging lens to form images of the Tx beams onto the detectors. The geometry of the imaging optics is described in the following sections.

Received signals from each of the nine channels are routed to an oscilloscope, and transferred to a control computer for MIMO processing, equalisation and subsequent OFDM processing.

5.2.1 Imaging optics geometry

This section describes the design of the geometry of the MIMO system considered. A thin lens approximation is used to obtain the required transmitter separation, *d,* which best aligns the transmitter and receiver. The thin lens equation is given by

$$\frac{1}{u}+\frac{1}{v}=\frac{1}{f} \tag{53}$$

where f is the lens focal length, u is the object size and v is the image size. Figure 51 shows the schematic of the geometrical arrangement of the MIMO optics.

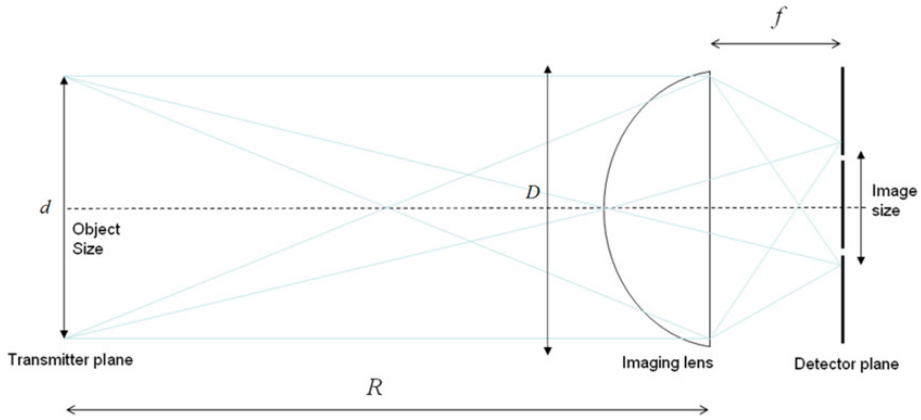

Figure 58. The geometrical arrangement of the MIMO optics based on thin lens equation.

The linear magnification approximation of a thin lens is given by

$$M=\frac{h_v}{h_u}\approx\frac{f}{R} \tag{54}$$

The ratio of the object size, h_u *i.e.* the separation d between Tx units, to the image size, h_v *i.e.* the separation between incident beams on the photodetectors is equivalent to the ratio of the range, R to the focal length, f. For a MIMO system to work all Tx beams must fall on the receiver, hence parameter d is constrained by

$$d<2R\tan(\Phi_{1/2})+D \tag{55}$$

where $\Phi_{1/2}$ is the half-power semi-angle of the transmitter, and D is the imaging lens diameter.

The lower limit of d is governed by the separation between detectors to ensure that no two beams fall onto the same detector

$$d > \frac{l}{M} - 2r \tag{56}$$

where l is the detector spacing, and r is the radius of the transmitter source.

5.2.2 Full-room MIMO configuration model

Based on the geometry described in Section 5.2.1, this section presents a model of MIMO transmitter-receiver design geometry to operate in a full-room VLC configuration as described in Section 2.4.3. For simplification, the model operates with assumptions that the transmitter is a point source, optical power is evenly distributed within the half-power semi-angle and the receiver has the same FOV as the transmitter. Table 11 shows the calculation parameters

Table 9. Calculation parameters.

Parameter	Description
Tx spacing, d	4m/30 LEDs = 13.33cm
Range, R	2m
LED half-power semi-angle, $\Phi_{1/2}$	5°
Imaging lens diameter, D	4.5cm

Figure 59 shows a schematic of a cross-section of the overlapping area of illumination from multiple Tx units based on the geometrical calculation of the VLC configuration considered. Figure 60 shows the corresponding receiver FOV, based on Figure 59. It can be seen from the calculation that there are a maximum of 3 Tx units that can be detected on a single axis, which gives a maximum total of 9 Tx units that can be detected at the receiver.

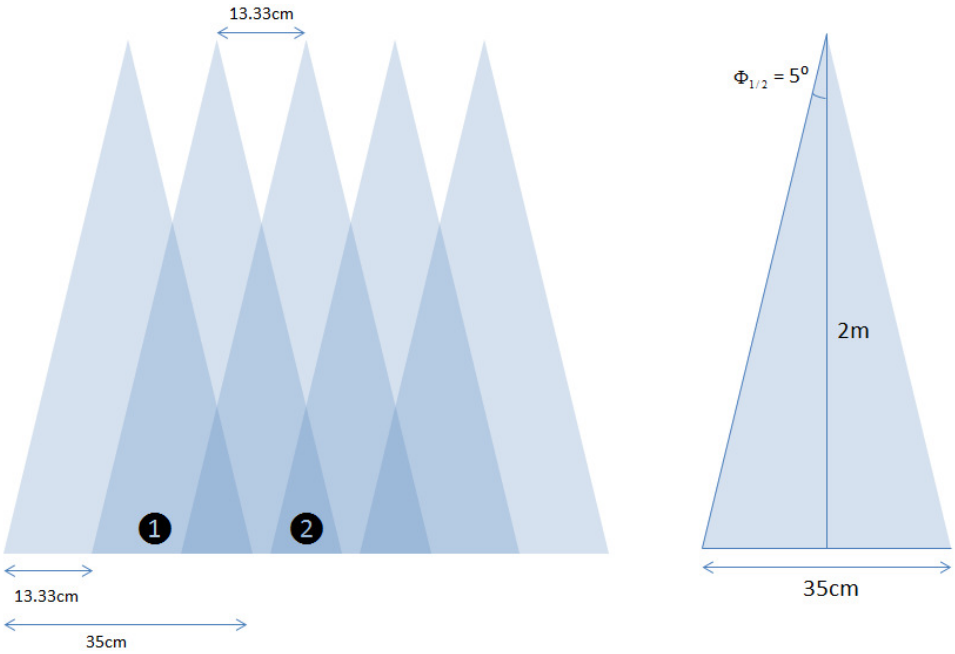

Figure 59. Schematic of a cross-section of the overlapping areas of illumination from multiple Tx unit based on the geometry of the VLC system described in Section 2.4.3, showing two cases of receiver FOV (1) and (2).

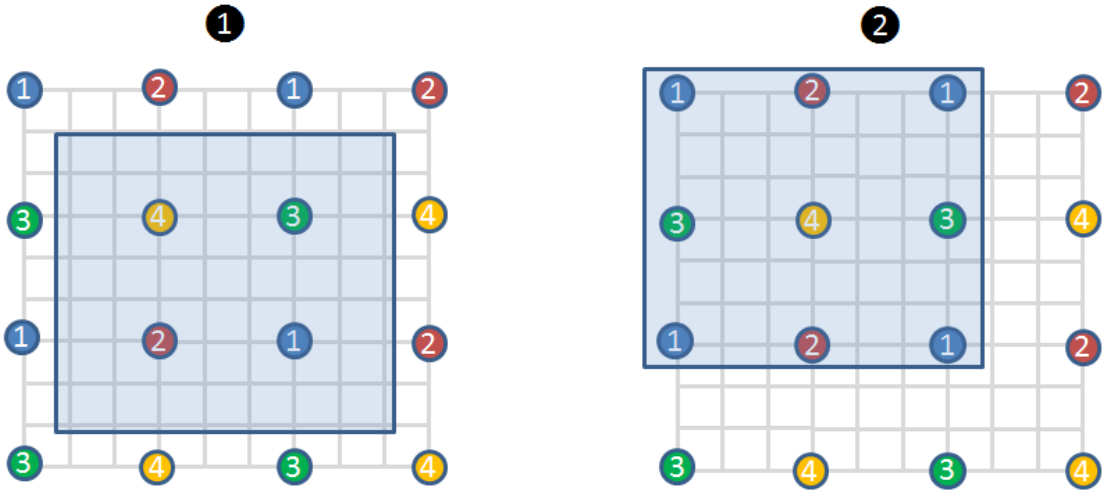

Figure 60. Schematic of the corresponding receiver FOV based on case (1) and (2) of the illumination overlapped as shown in Figure 61.

Given that the transmitter geometrical configuration is fixed based on the illumination level requirement described in Section 2.4.3, the MIMO receiver parameters are varied to ensure that the beam formation on the detector plane is designed to provide a full-rank matrix. Figure 63 shows magnification versus detector separation based on Equation (55). A magnification can be selected to ensure that the MIMO constraint that no two beams fall solely on the same detector is met. Two examples of receiver design are shown in Figure 63. a) The imaging lens magnification is reduced to 0.021 to allow the usage of the same MIMO receiver with detector spacing, l = 2.7mm and b) The receiver detector spacing is increased to l = 6mm to allow the use of the same imaging lens magnification, M=0.045.

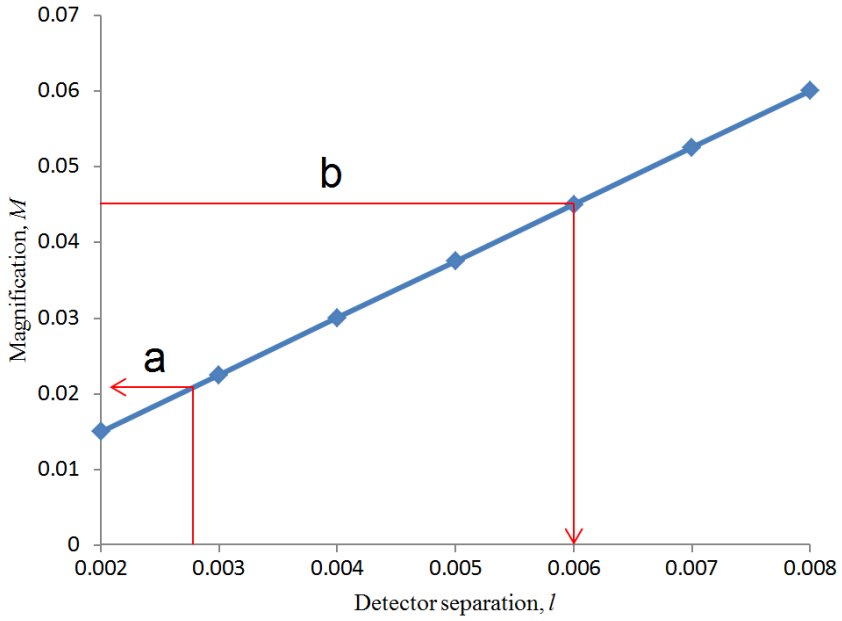

Figure 61. Magnification, M versus detector separation, l curve for Tx separation d=13.33cm plotted based on Equation (55) described in Section 4.2.1. Two designs are shown in a) the imaging lens magnification is reduced to 0.021 to allow the usage of the same MIMO receiver with detector spacing, l = 2.7mm and b) the receiver detector spacing is increased to l = 6mm to allow the usage of the same imaging lens magnification, M=0.045.

Full room coverage can be obtained by increasing the number of cells. It can be seen from calculation that this system can be scaled to give full-room coverage operation while maintaining the required illumination level. The practical demonstration of full room coverage and illumination is however beyond the scope of this work.

5.3 MIMO algorithm

The MIMO channel can be modelled as;

$$Y = HX + N \tag{57}$$

where Y is a 9-by-1 received signal vector; H is the 9-by-4 channel matrix; X is a 4-by-1 transmitted signal vector; and N is a 9-by-1 channel additive white Gaussian noise (AWGN) vector.

A technique to measure the channel matrix and to recover the signal has been reported in [84]. This experimental work was undertaken jointly with **Tran Tuan-Anh**, another DPhil candidate from the same research group.

The transmission begins by sending a set of training signals to estimate the channel matrix. This process is conducted by sending low frequency sinusoidal signals from a single Tx unit and the averaged amplitude of received sinusoids for each detector is recorded, while the rest of the Tx units are switched on (dc-biased) but not transmitting any signal. This process is repeated for each Tx unit, to obtain a series of scalar amplitudes, y_{ij} for the j-th Tx and the i-th detector. Each element of H is obtained by

$$h_{ij} = \sqrt{y_{ij}^2 - \sigma_i^2} \tag{58}$$

where σ_i^2 is the noise variance corresponding to the *i*-th detector. The noise variance is obtained from the statistics of the receiver noise y_i. This is measured when all the Tx units are switched on, but no signal is sent.

At the receiver, an estimate of X is given by

$$\overline{X} = GY \tag{59}$$

where G is a pseudo-inverse of the channel matrix H obtained using a minimum mean squared error (MMSE) algorithm [85]. Assuming that the Tx units are independent of each other, and have equal average transmission power ρ, the matrix G thus takes the form

$$G = H^{\dagger}(HH^{\dagger} + \frac{C_N}{\rho})^{-1} \tag{60}$$

where $H^{\dagger}$ is the Hermitian transpose of H and C_N is the covariance matrix of N.

5.4 BER versus bit-rate experiment

A bit-rate versus BER experiment is conducted with the aim of evaluating the performance of the best case of the MIMO-OFDM system. For this, the imaging lens is arranged in such a way that the Tx beams fall onto separate detectors to ensure a full rank channel matrix.

Figure 62 shows the experimental configuration, in which the transmitter is placed perpendicular to the receiver on the optical axis of the system. The range between the transmitter and receiver is set at 1m and the distance d between Tx units is set at 15cm. The total combined illumination level from all Tx units measured at the receiver plane is ~1000*lux* and each Tx unit contributes ~250*lux*.

The experiment is conducted using the following procedure:

1. A MIMO channel training run described in Section 4.3 is conducted to obtain the channel matrix, $\boldsymbol{H}$ and the pseudo-inverse channel matrix, $\boldsymbol{G}$.
2. A set of 16-QAM DCO-OFDM frames is sent from 10Mbps to 350Mbps per channel, corresponding to an overall transmission bit-rate of 40Mbps to 1.4Gbps. 16-QAM scheme is selected based on the available SNR for each channel. A total of 30,000 bits per channel is sent
3. At the receiver, the received signal vector is multiplied by $\boldsymbol{G}$ to obtain the estimate of the sent signal vector $\boldsymbol{X}$. The output of this process is four parallel streams, and each stream is further processed independently.
4. At each bit-rate, iterative channel equalisation is conducted for each stream. OFDM symbol recovery is conducted and the BER is recorded. A transmission with zero error is represented as a BER of $1x10^{-4}$ on the graph. A BER of $2x10^{-3}$ is taken as the target BER.

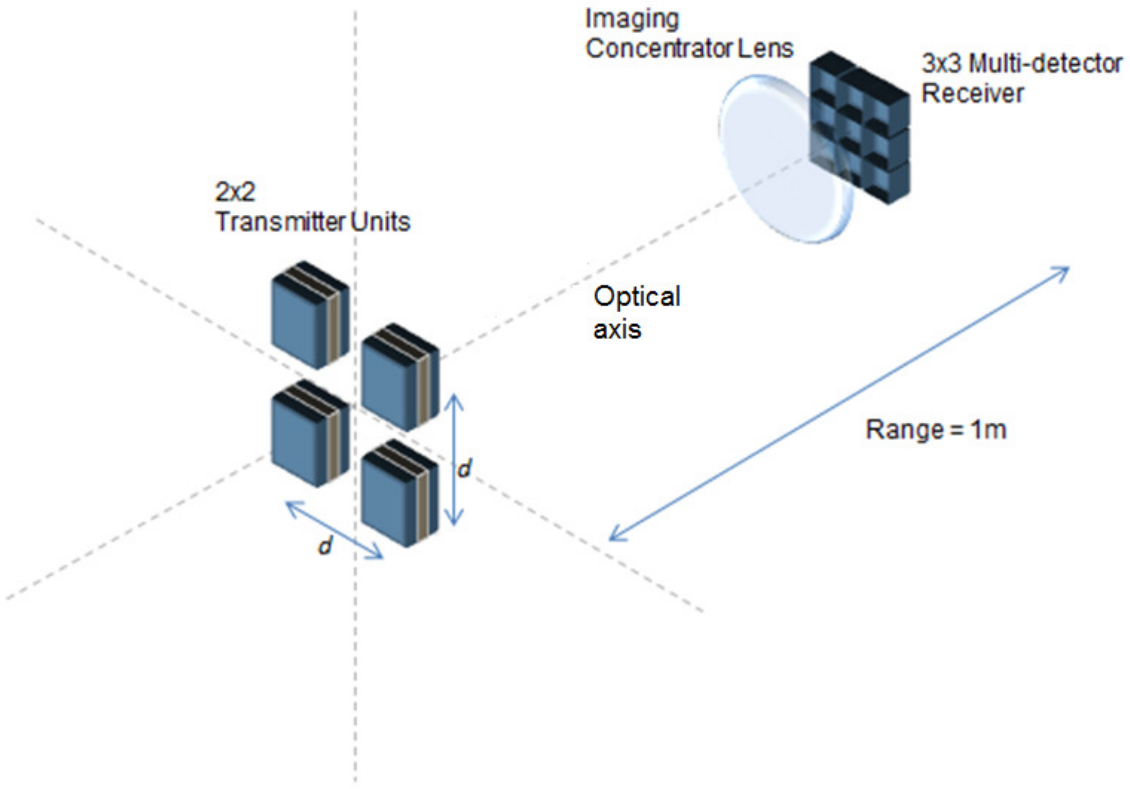

Figure 62. Experimental configuration for imaging MIMO transmission.

Figure 63 shows the BER versus bit-rate for 4-channel MIMO-OFDM transmission. A bit-rate of ~1.1Gbps can be achieved before exceeding the target BER. This uses a modulation bandwidth of ~65MHz per channel.

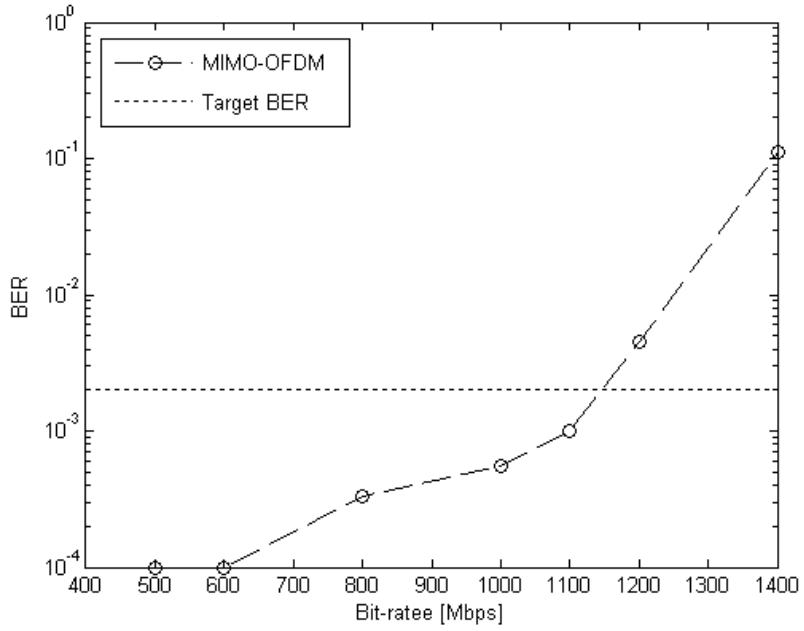

Figure 63. BER versus bit-rate for MIMO-OFDM transmission.

As a comparison, the experiment is repeated using a single channel of the system. This is to represent an ideal case for a single channel in a parallel communication system. For this transmission, the configuration used in the previous experiment remains the same but only a single Tx unit is active and transmitting data. The other three Tx units are switched on but inactive (no signal transmitted) to provide the required level of illumination.

Figure 64 shows BER versus bit-rate for SISO-OFDM and 'per channel' MIMO-OFDM. The SISO-OFDM and MIMO-OFDM per channel cases achieved transmission bit-rates of up to ~290Mbps and ~280Mbps at the target BER respectively, and error-free transmissions of ~250Mbps and ~150Mbps respectively. It can be seen that the SISO channel outperformed the MIMO system on a per channel basis, and the SISO channel also exhibits a lower BER floor. This is due to the additional penalty introduced by crosstalk between detectors when more than one detector of the multi-channel receiver is used for the MIMO system. An ideal multi-channel

communication system is a number of isolated parallel channels where there is no crosstalk between them, and the SISO example represents one such channel. However, such a system requires precise optical alignment between sources and detectors.

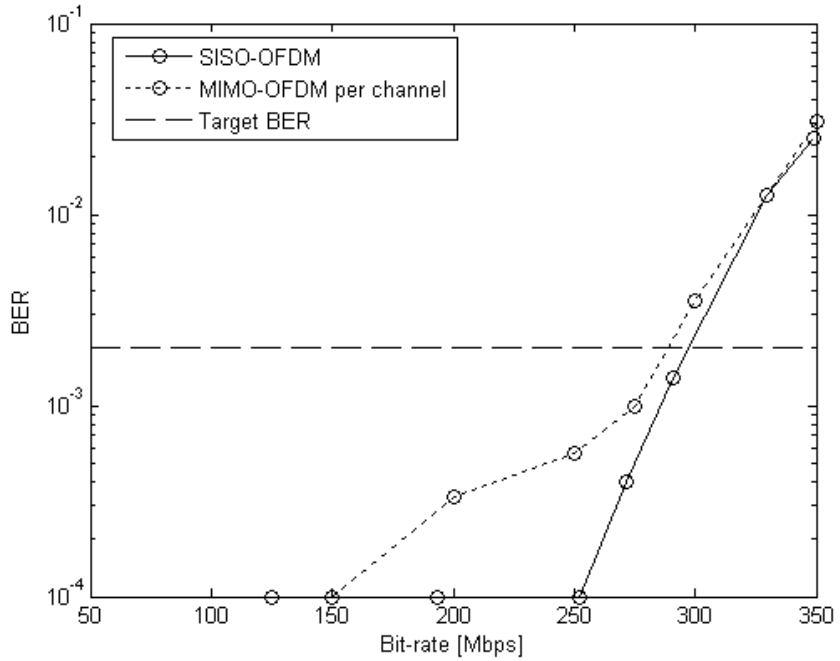

Figure 64. BER versus bit-rate for SISO-OFDM and per channel MIMO-OFDM.

This experiment demonstrated a static MIMO-OFDM transmission configuration, of which the formation of an aligned MIMO-OFDM channel is straightforward. However, in order to provide mobility and coverage, maintaining such precisely-aligned configuration is difficult because of dynamic positions between the transmitter and receiver. This results in the received light shifting away from a dedicated detector, which reduces received signal power and increases crosstalk/ spillover to adjacent detectors. In the extreme case, no signal can be detected and a realignment of the optical system is required. In the following section, the MIMO performance for a wide range of transmitter and receiver positions of the system is evaluated in the following section.

5.5 Comparison between DCO-OFDM and ACO-OFDM

This section presents an investigation into the overall the BER versus bit-rate performance for ACO-OFDM and dc-biased ACO-OFDM in MIMO transmission. The experiment is conducted using the MIMO transmission setup and experiment procedures as described in Section 5.4.

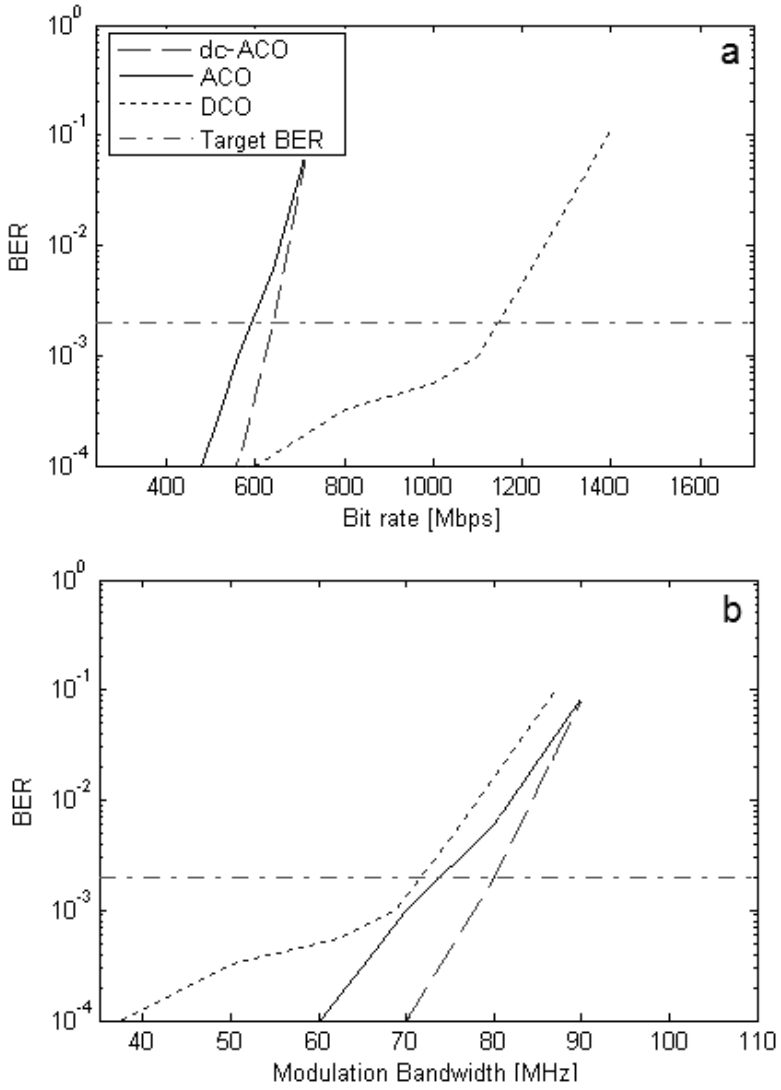

Figure 65. (a) BER versus bit-rate curves for ACO-OFDM, dc-biased ACO-OFDM and DCO-OFDM schemes and (b) the corresponding BER versus modulation bandwidth for each case.

Figure 73(a) shows the BER versus total transmission bit-rates and Figure 73(b) shows the corresponding BER versus per-channel modulation bandwidth for MIMO transmission using DCO-OFDM and dc-biased ACO-OFDM schemes. The bit-rate for ACO-OFDM MIMO parallel transmission is also included for comparison. Dc-biased ACO-OFDM achieved bit-rates of up to ~600Mbps and ACO-OFDM achieved bit-rates of up to ~560Mbps. It can be seen that DCO-OFDM outperforms both the power-efficient schemes with bit-rates of up to ~1.1Gbps.

5.6 Coverage experiment

In this section, the robustness of the imaging MIMO-OFDM transmission in providing coverage is investigated. Two sets of experiments are conducted to investigate the horizontal and vertical coverage limit of the system under consideration. Figure 66 shows the configurations for the experiments. The horizontal coverage is a combination of the range and horizontal displacement, while the vertical coverage is a combination of the horizontal displacement and vertical displacement.

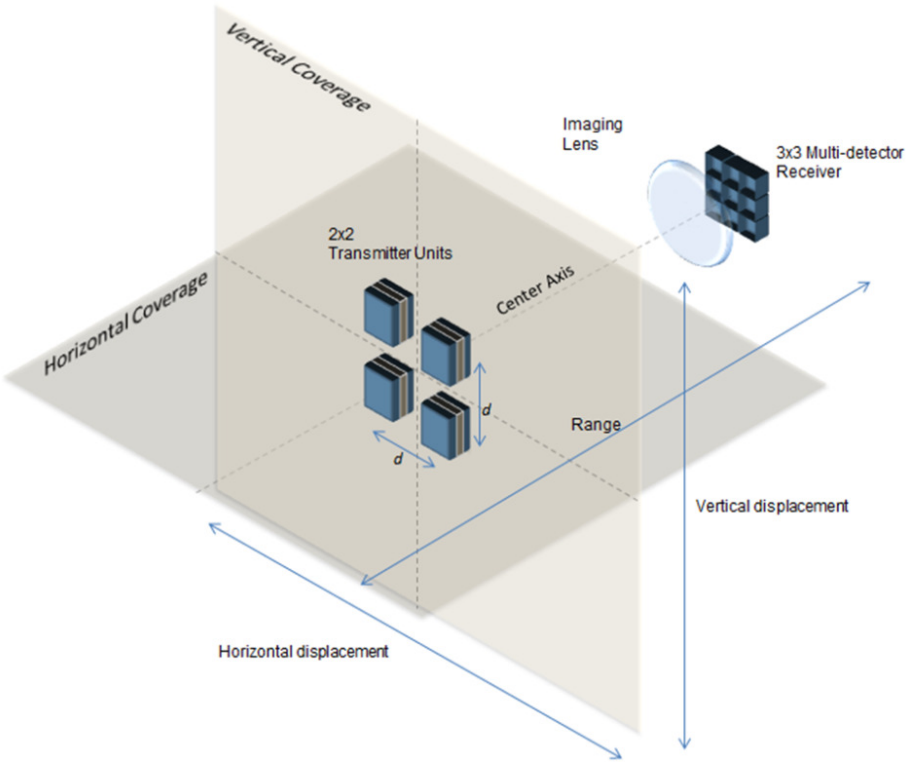

Figure 66. Configuration for vertical and horizontal coverage experiment.

5.6.1 Vertical coverage experiment

In this experiment, two configurations with d = 9.5cm and d = 15cm are selected to give different levels of illumination level at the receiver surface. The closer the separation d, the higher the combined illumination at the receiver plane.

In this experiment, the receiver is fixed and coverage is measured by moving the transmitter. The transmitter is initially placed perpendicular to the receiver at a 1m range, and the receiver is positioned in the centre of the illumination pattern as shown in Figure 66. The imaging lens is adjusted before the start of the experiment to ensure Tx beams fall on the detector for a full rank channel matrix. The experiment is conducted using the following procedure:

1. The separation, *d* between Tx units is set to 15cm. The combined illumination level at the receiver plane is measured.
2. The BER versus bit-rate experiment is taken on 7 x 7 points across horizontal and vertical displacements from this center point to form a surface plot.
3. At each displacement point, MIMO channel training is conducted to obtain the channel matrix.
4. This is then followed by transmission of a set of 16-QAM DCO-OFDM frames at ~250Mbps per channel, corresponding to an overall transmission bit-rate of ~1Gbps (1007Mbps). At each transmission, channel equalisation is conducted and a binary stream of 30,000 bits per channel is sent. A raw BER of $2x10^{-3}$ is taken as the target BER. The measured BER is represented by $\log_{10}$(BER) on the BER plot..
5. Step 1-4 is repeated using a configuration in which the transmitter spacing, *d* is reduced to 9.5cm. The combined illumination level at the receiver plane is measured.

Figure 67 shows the BER versus vertical and horizontal displacements for the 15cm spacing configuration. The vertical coverage within the target BER of $2x10^{-3}$ is measured to be ~4cm x ~4cm = ~16cm^2. The combined illumination level at the centre axis of the receiver *i.e.* on the imaging lens plane is measured at ~1000*lux*.

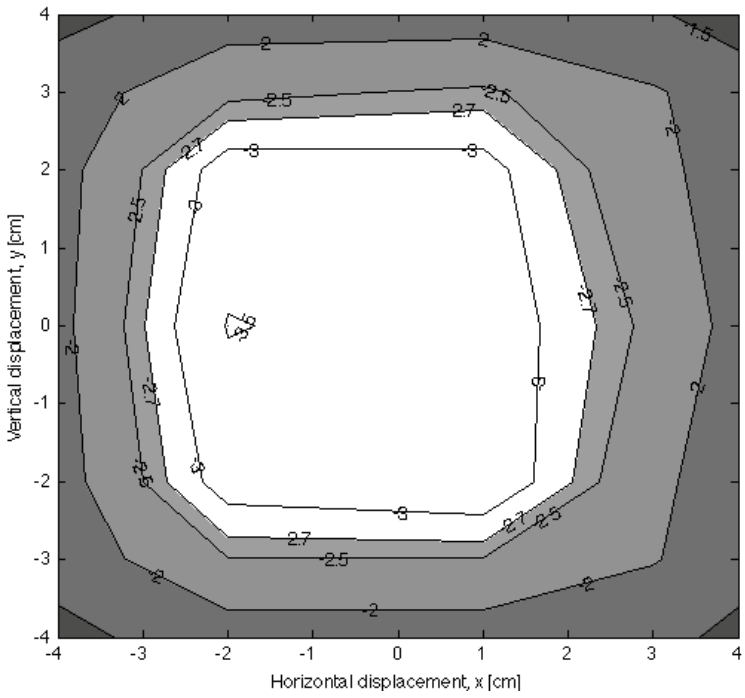

Figure 67. Vertical coverage for *d*=15cm. The white region shows the coverage within the BER of $2x10^{-3}$.

Figure 68 shows the BER versus vertical and horizontal displacements for the 9.5cm spacing configuration. The vertical coverage within the target BER of $2x10^{-3}$ is measured to be ~10cm x ~10cm = ~$100cm^2$. The combined illumination level at the centre axis of the receiver plane is measured at ~1500*lux*.

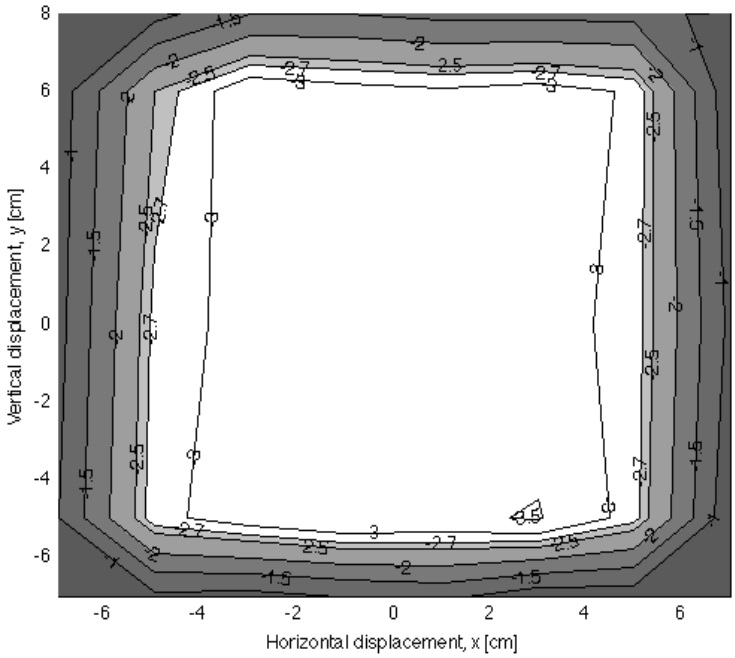

Figure 68. Vertical coverage for *d*=9.5cm. The white region shows the coverage within the BER of $2x10^{-3}$.

It can be seen from both results that there is 1Gbps transmission at the target BER within the white area. This shows that crosstalk between Tx units is mitigated without the need to realign the imaging lens. BER performance degrades away from the center of the coverage area due to lower illumination intensity, and falls off rapidly as the beam images do not fall on the receiver.

Based on these results, the coverage measured is compared with the calculation of beam displacement on the receiver surface using the thin lens equation given in Section 4.2.1. The parameters used in the calculation are summarised in Table 9.

It can be seen from Figure 53 that transmission at 1Gbps rate achieves a BER of $5x10^{-4}$. Thus, to achieve the target BER of $2x10^{-3}$ at this transmission rate, there is a BER margin. This allows some portion of the beam images to fall out of the detector which increases coverage. Therefore, for a

simplified approximation, the calculation is conducted with an assumption that to achieve a transmission below the target BER, at least half of all the beam images must fall onto a detector.

Table 10. Geometry calculation parameters.

Parameter	Description
Focal length, *f*	4.5cm
Magnification, *M*	0.045
Detector size	2.70mm (with 0.10mm spacing between detectors)
Tx source diameter (object)	30.50mm
Beam diameter (image)	1.37mm

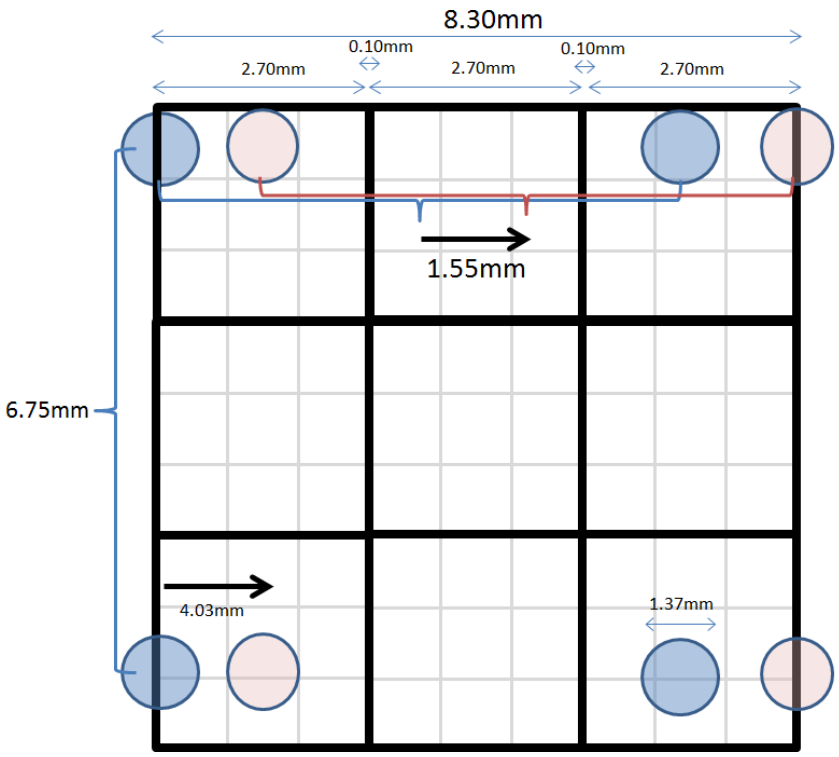

Figure 69. Schematic showing the beam displacement (blue to red) on the detector surface for *d* =15cm.

For the first case of d = 15cm, the separation between beams is calculated to be 3.75mm. Figure 58 shows a simplified schematic to show the beam (image) formation on the detector plane. For this

arrangement, the maximum calculated horizontal displacement from one end to another is 1.55mm before the beam moves out of the detector plane, which corresponds to 3.4cm calculated horizontal displacement of Tx units (object). For a square arrangement, this gives a total calculated horizontal and vertical displacements (coverage) area of 3.4cm x 3.4cm = 11.55cm^2.

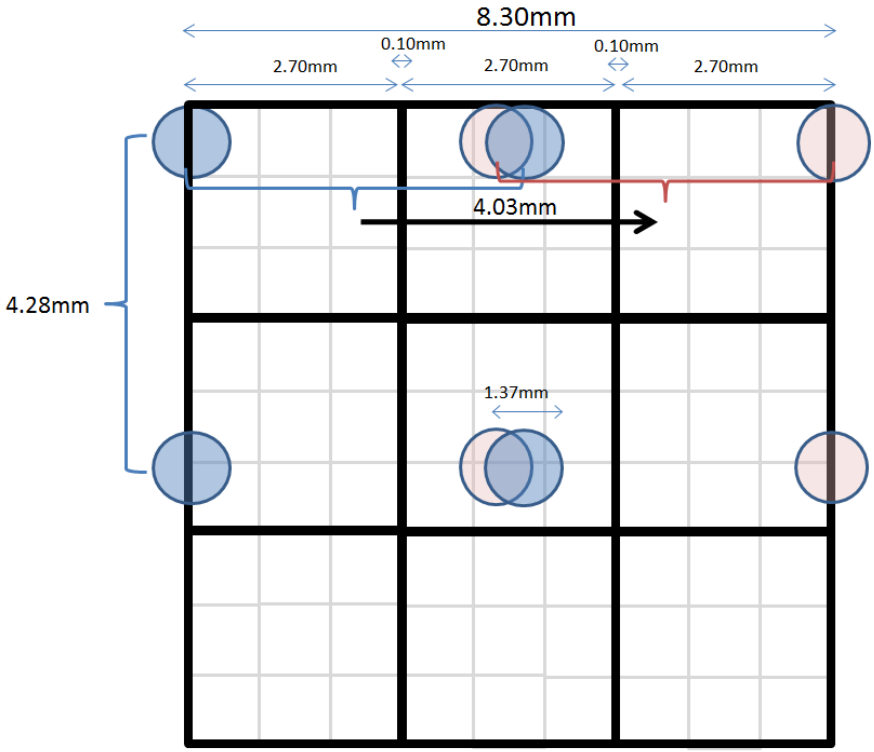

Figure 70. Schematic showing the beam displacement (blue to red) on the detector surface for *d* = 9.5cm.

For the second case of *d* = 9.5cm, the separation between beams is calculated to be 2.37mm. Figure 59 shows a simplified schematic to show the beam (image) formation on the detector plane. For this arrangement, the maximum calculated horizontal displacement from one end to another is 4.03mm before the beam moves out of the detector plane, which corresponds to 9cm calculated horizontal displacement of Tx units (object). For a square arrangement, this gives a total calculated horizontal and vertical displacements (coverage) area of 9cm x 9cm = 81cm^2.

Table 10 shows calculated parameters for each Tx separation cases. The measured coverage for both cases is close to the geometry calculation, with a disparity that is likely due from misalignments of the manually-positioned imaging lens. As the separation *d* decreases, a bigger area of overlapping illumination exists allowing a greater displacement on the detector surface thus providing a greater coverage. This is also results in an increased of the combined illumination level at the receiver plane.

Table 11. Parameters obtained from the geometry model, and also included are the measured results.

Parameter	Description	
Tx spacing, *d* (object)	9.5cm	15.0cm
Beam spacing (image)	4.28mm	6.75mm
Calculated maximum beam displacement (image)	4.03mm	1.55mm
Calculated maximum source displacement (object)	9.0cm	3.4cm
Calculated coverage	81cm^2	11.55cm^2
Measured maximum displacement within target BER	~10cm	~4cm
Measured coverage	100cm^2	16cm^2

Ultimately, coverage is limited by the number of transmitter and detector sources. Nevertheless, in typical VLC systems, a larger number of transmitter sources are inherently used to provide the required illumination for full room coverage. This system under consideration is an example of a single MIMO unit that can be scaled to give room-wide coverage and the required illumination level by adding more cells. The 4-channel MIMO unit under consideration is a part of a bigger full-room configuration as explained in Section 2.4.3. With adjacent cells placed next to each other, the MIMO algorithm can detect the contribution of a particular Tx from the adjacent cells. Figure 60 shows an example of an operation of such configuration. The blue box represents the field-of-view (FOV) of the receiver and the coloured circles represent Tx channels; a set of four channels for each cell. As

the receiver moves out of a specific cell (case A to case B), a retraining of the MIMO matrix is conducted to take account channel from the adjacent cells. The following section presents a model of MIMO configuration to provide full-room coverage.

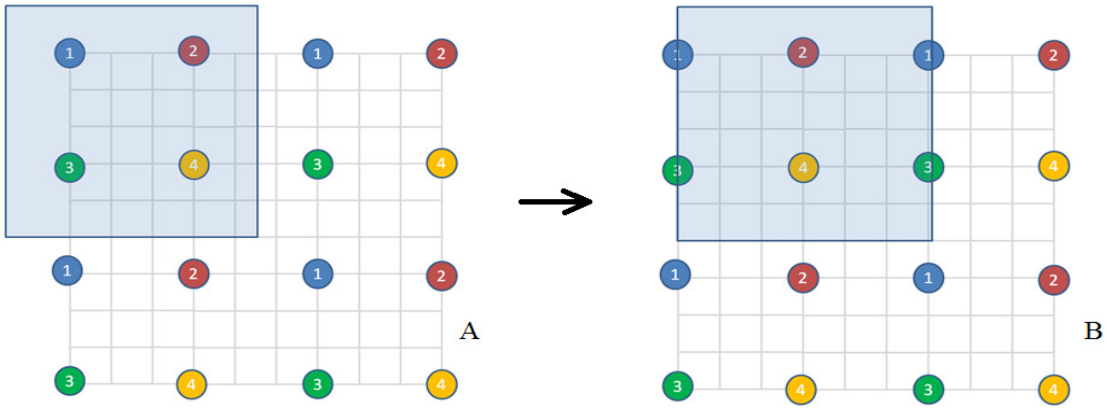

Figure 71. Schematic of an example of cellular arrangements for the MIMO system to provide full room coverage. MIMO channel training is conducted after moving the receiver from case A to case B, which will take account of sources from the adjacent cells.

5.6.2 Horizontal coverage experiment

Next, an experiment is conducted using the same apparatus and configuration to investigate the horizontal coverage, which is a combination of the range and horizontal displacement. Experimental setup is as shown in Figure 55. The separation, *d* between Tx units is set to 9cm. The imaging lens is adjusted once before the start of the experiment to ensure Tx beams fall on the detector for a full rank channel matrix. The experiment is conducted using the following procedure:

1. The range is set at 70cm and the BER for 16-QAM DCO-OFDM at 1Gbps transmission is recorded.

2. The experiment is conducted for 7 points across a ±7cm horizontal displacement from the centre. At each displacement point, MIMO channel training is conducted to obtain the channel matrix, and 30,000 bits per channel is sent.
3. Step 2. is repeated at 7 points between the range of 70cm and 130cm, giving an overall 7x7 points of horizontal surface coverage. At each range, the illumination level at the receiver *i*.e. the imaging lens plane is measured.
4. A raw BER of $2x10^{-3}$ is taken as the target BER. The measured BER is represented by $\log_{10}$(BER) on the BER plot.

Figure 72 shows the BER at points across the range and horizontal displacement at 1Gbps and Figure 73 shows measured illumination level versus range. It can be seen that as the range is decreased/increased from 1m *i.e.* initial position where the optical alignment is optimised, the BER falls rapidly.

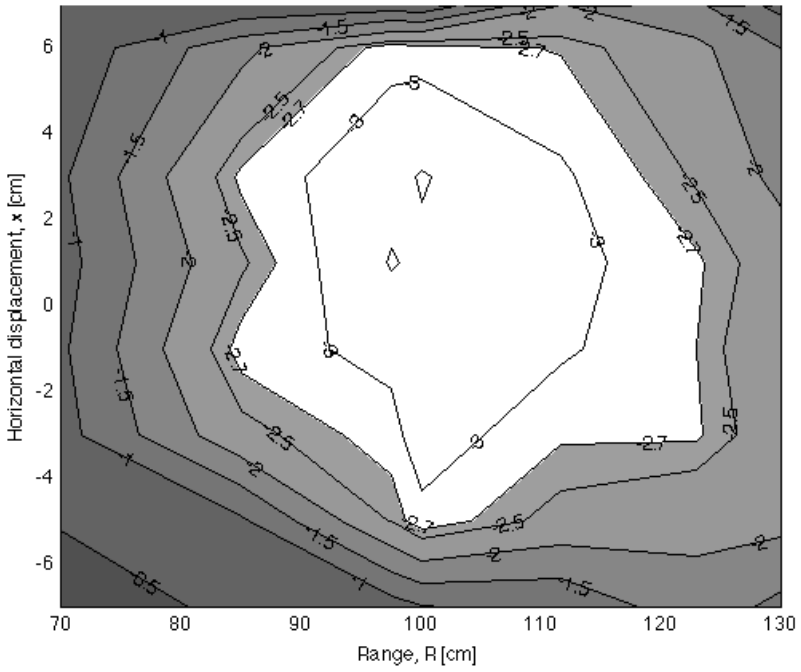

Figure 72. Horizontal coverage for *d*=9cm. The white region shows the coverage within the BER of $2x10^{-3}$.

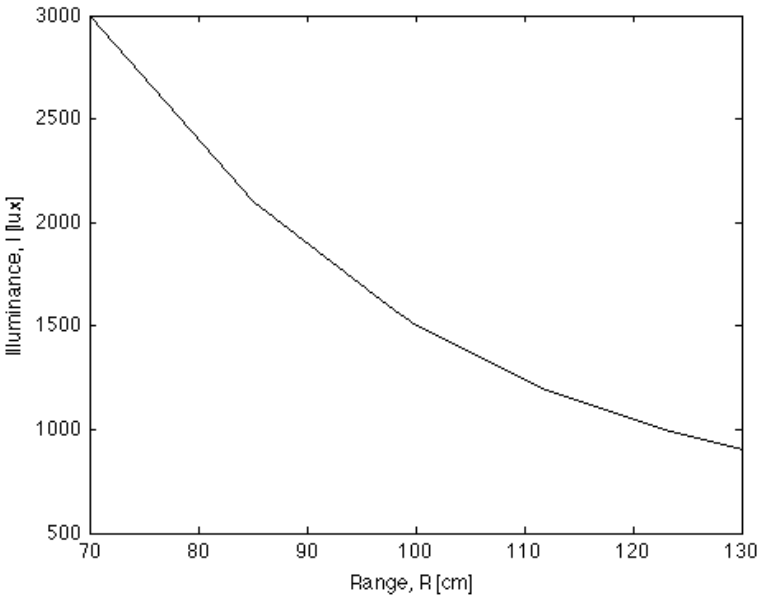

Figure 73. Measured illumination level versus range for the MIMO transmitter with d = 9cm.

This is caused by two factors. First, as the range decreases, the incident power at the receiver increases which results in BER degradation due to receiver saturation as discussed in Chapter 3. As the range increases, the available signal power for communications decreases, resulting in BER degradation. Second, BER degradation is also caused by beam images on the detectors being defocussed as the range is decreased/increased. This results in an increase in the image beam size, which increases the level of crosstalk that the channel matrix has. In turn, this leads to lower performance.

Nevertheless, it can be seen that a Gigabit/s transmission at the target BER can still be achieved within the range of 85cm to 125cm. This shows that the MIMO system is robust to the effect of crosstalk from a defocussed image, given that the channel matrix is maintained at full rank.

5.7 Conclusions

In this chapter, a MIMO communications method is introduced and a prototype imaging-diversity MIMO-OFDM system is built. A 4-channel MIMO transmission experiment is conducted at an illumination level of 1000*lux*.

The experiment has demonstrated that the MIMO transmission system overcomes the dynamic range limitation of a single-channel transmission. Transmission bit-rates of up to ~1.1Gbps are achieved. This would not be possible for a single-channel transmission as receiver saturation and signal clipping occur beyond a 500*lux* illumination level due to the limited dynamic range.

Nevertheless, a comparison between the best case of per channel MIMO transmission and an ideal isolated channel case shows that there is penalty introduced by the MIMO system due to crosstalk between channels. However, establishing such an ideal channel is difficult and requires precise and complex mechanical optical alignment.

The imaging MIMO system provides a straightforward and simple configuration, and the MIMO processing algorithm mitigates inter-channel crosstalk and removes the requirement of mechanical realignment by shifting channel realignment from optical to electrical domain. In the coverage experiment, the imaging MIMO system has demonstrated to be robust to changes in receiver-transmitter positions in providing coverage, as long as the channel matrix is maintained at full rank. Coverage is limited for the system under consideration due to the limited transmitter sources. Nevertheless, this system can be scaled to provide room-wide coverage by replicating more MIMO cellular units.

Chapter 6

Conclusions and Future Directions

The main aim of this research is to address the challenge of increasing data rate for indoor wireless communications using VLC. The thesis presents an investigation into practical challenges and potential methods in increasing data rates for indoor VLC systems.

The main contribution from these investigations is a novel imaging diversity MIMO-OFDM system as method to achieve high data rates. This system optimises channel spectral efficiency using the OFDM modulation scheme, and increases the overall channel capacity using multi-channel MIMO transmission. This allows transmission at data rates of up to ~1.1Gbps at a target BER of $2x10^{-3}$. The main conclusions from the thesis are summarised as follows:

1) The thesis begins by reporting the characteristics and constraints of the VLC channel and components of the VLC system, which is analysed using theoretical simulation and experimental investigation. A simulation of the illumination level from the experimental Luxeon Star-C LED in providing room-wide coverage is reported.

   The VLC channel exhibits a high SNR under a standard room illumination level. However, increasing the VLC transmission bit-rate faces several constraints; particularly LED bandwidth and the limited dynamic range of system components. Several methods of increasing transmission rate are introduced.

2) One such method is using a blue filter to block slow phosphor component of the LED to increase the bandwidth of the LED frequency response. Analytical and experimental measurements show that the blue filter method improves the bandwidth of the channel. However there is a trade-off between bandwidth and power and the blue filter response has to be selected taking into considerations of competing factors including the frequency response and the available signal power of the light that passes through the filter.

3) OFDM is introduced as a key approach to improving data rates in bandwidth-limited VLC systems by increasing the spectral efficiency of signal transmission.

   To investigate this, a VLC OFDM system is built and the performance and constraints of this system are specified. It is shown experimentally that the OFDM scheme is sensitive to frequency/phase offsets in the system. This is due to the low-pass characteristics of the channel frequency response, which results in the rotation of subcarrier signal constellations. This increases bit-error and limits transmission bit-rates.

   One of the advantages of OFDM is a straightforward implementation of frequency domain equalisation using the IFFT algorithm to compensate the low-pass characteristics of the channel frequency response. An equalisation method is introduced that incorporates pre- and post-equalisation in frequency and time domain. This method corrects constellation rotations and equalises SNR on each subcarrier.

4) Using this approach, transmission bit-rates of up to ~310Mbps at 460*lux* illumination level on a single channel link are reported. This corresponds to a modulation bandwidth of ~85MHz, which shows the outstanding performance of the OFDM system in transmitting

high data rates at frequencies beyond the channel bandwidth of 4.6MHz. Further increase in data rates for this transmission is constrained by the dynamic range available at the receiver.

5) The thesis presents an extended investigation on several other OFDM approaches. In practical transmission cases, asymmetrical OFDM schemes suffer from the effect of baseline wander, which results in severe bit-rate degradation. To our knowledge, this is the first time that this has been reported. This result introduces a severe constraint on the asymmetrical OFDM approach. Dc-biased ACO-OFDM is introduced as an alternative power-efficient approach that is robust to baseline wander. A single-channel transmission using this scheme achieves transmission rates of up to ~180Mbps. This scheme has shown to offer 3dB gain in signal power over DCO-OFDM. However, for signal transmissions in a bandwidth-limited system, the bandwidth efficiency advantage of DCO-OFDM outweighs the power advantage of dc-biased ACO-OFDM giving a higher overall bit-rate.

6) A MIMO system offers a linear capacity gain with the number of transmission channels in an ideal configuration. This system is a potential solution to mitigate the dynamic range limitation, as power is divided between multiple channels. To investigate this, an imaging MIMO transmission experiment is conducted under the same dynamic range constraint. A 4-channel MIMO transmitter is built using four sets of transmitter components of the single-channel link, giving a combined illumination of 1000*lux* at the MIMO receiver plane. An imaging system is used to separate the optical power at the receiver plane onto multiple detectors, and MIMO processing relaxes the requirements for precise mechanical alignments. This allows data rates of up to ~1.1Gigabit/s at a BER of $2\text{x}10^{-3}$. To the author's knowledge, this reported data rates is the highest recorded for an indoor VLC MIMO-

OFDM transmission. The first practical implementation of MIMO-OFDM transmission in visible light communications was reported in [91] by the author and co-writers.

7) An investigation into MIMO system scalability to provide room-wide coverage is presented. In a coverage experiment conducted, the imaging MIMO system was demonstrated to be robust to changes in receiver-transmitter positions in providing coverage, as long as the channel matrix is maintained at full rank. However, coverage is limited for the system in consideration due to the limited number of transmitters and detectors.

6.1 Future work

To further increase data rates and to provide the required coverage, the possible areas into which this work may usefully be extended are set out as follows.

6.1.1 Further increase in data rates

Further increase in transmission rates can be realised by two means: 1) Increase the data rates of per channel transmission and 2) Increase the number of parallel transmission channel. From a system point-of-view, data rates per channel can be possibly increased using advanced transmitter and receiver components. For example, a micro-LED (μLED) array as demonstrated in [92] can be potentially used. Work reported in [92] shows transmission bit-rates of up to 1.5Gbps are achieved using a CMOS-controlled MIMO approach, but range and coverage is limited due to low signal power of these LED emission. An investigation into the possibilities and limitations of an imaging MIMO-OFDM system design using multiple of these μLEDs to provide the required room-wide illumination would be an interesting area of further studies.

More complex transmitter and receiver components also offer the potential for higher data rates. RGB LEDs offer the potential of wavelength-division multiplexing, and transmission bit-rates of up to ~3.4Gbps are achieved using a single RGB LED [63]. The application of RGB LED in MIMO systems is also attractive. However, this system requires a complex receiver design with an added diversity: to separate signals from multiple sources, as well as multiple colours.

At the receiver end, data rates per channel can be improved by increasing per channel SNR using receivers with a higher sensitivity. For example, an advanced avalanche photodiode (APD) receiver as demonstrated in [61] shows that bit-rates of ~600Mbps per channel can be obtained at a very low illumination level of 10*lux*.Again, this is at the cost of complexity.

6.1.2 Improving coverage

In section 4.5, a proof-of-concept model on MIMO system scalability has been presented. Work to improve coverage is required. This should include the effects such as shadowing, and the configuration of the mobile receiver. There is also a possibility of integrating the imaging MIMO system with beam-steering methods to further increase MIMO performance under these constraints.

References

[1] T. M. Siep, I. C. Gifford, R. C. Braley, and R. F. Heile, "Paving the way for personal area network standards: an overview of the IEEE P802.15 Working Group for Wireless Personal Area Networks," *IEEE Personal Communications,* vol. 7, pp. 37-43, Feb 2000

[2] W. H. L. John M. Chapin, "Mobile Broadband Growth, Spectrum Scarcity, and Sustainable Competition," *39th Research Conference on Communications Information and Internet Policy,* September 23-25 2011.

[3] H. Haas, "The Visible Light Communications Motivation," *http://visiblelightcomm.com*, pp. http://visiblelightcomm.com/the-visible-light-communications-motivation/ December 12 2011.

[4] J. M. Kahn and J. R. Barry, "Wireless infrared communications," *Proceedings of the IEEE,* vol. 85, pp. 265-298, 1997.

[5] S. Arnon, "Underwater optical wireless communication network," *Optical Engineering,* vol. 49, January 2010.

[6] H. Elgala, "PhD Thesis - Non-Linearity in OFDM," 2010.

[7] *Technologies for the Wireless Future* vol. 2: Wireless World World Research Forum, WILEY, 2006.

[8] J. Grubor, S. Randel, K. D. Langer, and J. W. Walewski, "Broadband Information Broadcasting Using LED-Based Interior Lighting," *Journal of Lightwave Technology,* vol. 26, pp. 3883-3892, 2008.

[9] Y. Tanaka, T. Komine, S. Haruyama, and M. Nakagawa, "Indoor visible communication utilizing plural white LEDs as lighting," in *2001 12th IEEE International Symposium on Personal, Indoor and Mobile Radio Communications,* 2001, pp. F-81-F-85 vol.2.

[10] K. Fan, T. Komine, Y. Tanaka, and M. Nakagawa, "The effect of reflection on indoor visible-light communication system utilizing white LEDs," in *The 5th International Symposium on Wireless Personal Multimedia Communications, 2002.*2002, pp. 611-615 vol.2.

[11] T. Komine and M. Nakagawa, "Performance evaluation of visible-light wireless communication system using white LED lightings," in *Ninth International Symposium on Computers and Communications, 2004. Proceedings. ISCC 2004.*2004, pp. 258-263 Vol.1.

[12] D. C. O'Brien, L. Zeng, H. Le-Minh, G. Faulkner, J. W. Walewski, and S. Randel, "Visible light communications: Challenges and possibilities," in *IEEE 19th International Symposium on Personal, Indoor and Mobile Radio Communications, 2008. PIMRC 2008.* 2008, pp. 1-5.

[13] P. Lumiled, "LUXEON STAR Technical Datasheet DS23."

[14] L. Zeng, "PhD Thesis - Indoor Optical Wireless Communications Using White Light LEDs," 2009.

[15] Z. Lubin, M. Hoa Le, D. O'Brien, G. Faulkner, L. Kyungwoo, J. Daekwang, and O. YunJe, "Equalisation for high-speed Visible Light Communications using white-LEDs,"

in *CNSDSP 2008. 6th International Symposium on Communication Systems, Networks and Digital Signal Processing, 2008.* 2008, pp. 170-173.

[16] T. Komine and M. Nakagawa, "A study of shadowing on indoor visible-light wireless communication utilizing plural white LED lightings," in *1st International Symposium on Wireless Communication Systems, 2004.* 2004, pp. 36-40.

[17] A. Polzer, W. Gaberl, M. Davidovic, and H. Zimmermann, "Integrated filter-less BiCMOS sensor for RGB-LED color determination," in *2011 IEEE Sensors,* 2011, pp. 1937-1940.

[18] S. Muralidharan and P. S. Dutta, "Color quality control in dual use solid state lighting and visible light communication systems using coded inverse multiplexing," in *2012 IEEE Photonics Society Summer Topical Meeting Series,* 2012, pp. 151-152.

[19] H. Le Minh, Z. Ghassemlooy, A. Burton, and P. A. Haigh, "Equalization for organic light emitting diodes in visible light communications," in *2011 IEEE GLOBECOM Workshops (GC Wkshps),* 2011, pp. 828-832.

[20] P. A. Haigh, Z. Ghassemlooy, and I. Papakonstantinou, "1.4-Mb/s White Organic LED Transmission System Using Discrete Multitone Modulation," *IEEE Photonics Technology Letters,* vol. 25, pp. 615-618, 2013.

[21] C. Hyunchae, C. Chien-Jung, and D. O'Brien, "Visible light communication using OLEDs: Illumination and channel modeling," in *2012 International Workshop on Optical Wireless Communications (IWOW),* 2012, pp. 1-3.

[22] EN12464-1Standard, "European standard of lighting for indoor workplaces," April 2003.

[23] Z. Lubin, D. O'Brien, H. Le-Minh, L. Kyungwoo, J. Daekwang, and O. Yunje, "Improvement of Date Rate by using Equalization in an Indoor Visible Light Communication System," in *ICCSC 2008. 4th IEEE International Conference on Circuits and Systems for Communications, 2008.*2008, pp. 678-682.

[24] M. N. Toshihiko Komine, "Fundamental Analysis for Visible-Light Communication System using LED Lights," *IEEE Transactions on Consumer Electronics,* vol. 50, p. 100, 2004.

[25] F. R. Gfeller and U. Bapst, "Wireless in-house data communication via diffuse infrared radiation," *Proceedings of the IEEE,* vol. 67, pp. 1474-1486, 1979.

[26] C. K. Jelena Vuˇcic´, Stefan Nerreter, Klaus-Dieter Langer, and Joachim W. Walewski, "513 Mbit/s Visible Light Communications Link Based on DMT-Modulation of a White LED," *JOURNAL OF LIGHTWAVE TECHNOLOGY,* vol. 28, pp. 3512-3518, 2010.

[27] M. Hoa Le, D. O'Brien, G. Faulkner, Z. Lubin, L. Kyungwoo, J. Daekwang, and O. YunJe, "High-Speed Visible Light Communications Using Multiple-Resonant Equalization," *IEEE Photonics Technology Letters,* vol. 20, pp. 1243-1245, 2008.

[28] M. Hoa Le, D. O'Brien, G. Faulkner, Z. Lubin, L. Kyungwoo, J. Daekwang, O. YunJe, and W. Eun Tae, "100-Mb/s NRZ Visible Light Communications Using a Postequalized White LED," *IEEE Photonics Technology Letters,* vol. 21, pp. 1063-1065, 2009.

[29] Y. A. Alqudah and M. Kavehrad, "Optimum order of angle diversity with equal-gain combining receivers for broad-band indoor optical wireless communications," *IEEE Transactions on Vehicular Technology,* vol. 53, pp. 94-105, 2004.

[30] G. Yun and M. Kavehrad, "Spot-diffusing and fly-eye receivers for indoor infrared wireless communications," in *1992 IEEE International Conference on Selected Topics in Wireless Communications, 1992. Conference Proceedings,* 1992, pp. 262-265.
[31] J. M. Kahn, R. You, P. Djahani, A. G. Weisbin, T. Beh Kian, and A. Tang, "Imaging diversity receivers for high-speed infrared wireless communication," *IEEE Communications Magazine,* vol. 36, pp. 88-94, 1998.
[32] VLCC. (2008). *Visible Light Communications Consortium*. Available: www.vlcc.net
[33] WWRF. *Wireless World World Research Forum*. Available: www.wireless-world-research.org
[34] IEEE. (2008). *IEEE 802.15.7 WPAN Visual Light Communication Study Group*. Available: http://www.ieee802.org/15/pub/IGvlc.html
[35] www.ted.com. (2012). *Harald Haas: Wireless data from every light bulb*.
[36] http://www.lificonsortium.org/.
[37] "IEEE Standard for Information technology-- Local and metropolitan area networks-- Specific requirements-- Part 11: Wireless LAN Medium Access Control (MAC)and Physical Layer (PHY) Specifications Amendment 5: Enhancements for Higher Throughput," *IEEE Std 802.11n-2009 (Amendment to IEEE Std 802.11-2007 as amended by IEEE Std 802.11k-2008, IEEE Std 802.11r-2008, IEEE Std 802.11y-2008, and IEEE Std 802.11w-2009),* pp. 1-565, 2009.
[38] B. Bellalta, J. Barcelo, D. Staehle, A. Vinel, and M. Oliver, "On the Performance of Packet Aggregation in IEEE 802.11ac MU-MIMO WLANs," *IEEE Communications Letters,* vol. 16, pp. 1588-1591, 2012.
[39] O. Bouchet, M. El Tabach, M. Wolf, D. C. O'Brien, G. E. Faulkner, J. W. Walewski, S. Randel, M. Franke, S. Nerreter, K. D. Langer, J. Grubor, and T. Kamalakis, "Hybrid wireless optics (HWO): Building the next-generation home network," in *6th International Symposium on Communication Systems, Networks and Digital Signal Processing, 2008. CNSDSP 2008.* 2008, pp. 283-287.
[40] S. Rajagopal, R. D. Roberts, and L. Sang-Kyu, "IEEE 802.15.7 visible light communication: modulation schemes and dimming support," *IEEE Communications Magazine,* vol. 50, pp. 72-82, 2012.
[41] W. Zixiong, Y. Changyuan, Z. Wen-De, C. Jian, and C. Wei, "Performance of variable M-QAM OFDM visible light communication system with dimming control," in *2012 17th Opto-Electronics and Communications Conference (OECC),* 2012, pp. 741-742.
[42] I. Stefan, H. Elgala, and H. Haas, "Study of dimming and LED nonlinearity for ACO-OFDM based VLC systems," in *2012 IEEE Wireless Communications and Networking Conference (WCNC),* 2012, pp. 990-994.
[43] G. Ntogari, T. Kamalakis, J. Walewski, and T. Sphicopoulos, "Combining Illumination Dimming Based on Pulse-Width Modulation With Visible-Light Communications Based on Discrete Multitone," *IEEE/OSA Journal of Optical Communications and Networking,* vol. 3, pp. 56-65, 2011.
[44] C. Joon-Ho, C. Eun-byeol, K. Tae-gyu, and L. Chung Ghiu, "Pulse width modulation based signal format for visible light communications," in *2010 15th OptoeElectronics and Communications Conference (OECC),* 2010, pp. 276-277.

[45] M. N. Dyble, Nadarajah; Bierman, Andrew; Klein, Terence, "Impact of dimming white LEDs: chromaticity shifts due to different dimming methods," *Fifth International Conference on Solid State Lighting,* vol. 5941, pp. 291-299, 2005.

[46] D. J. F. Barros, S. K. Wilson, and J. M. Kahn, "Comparison of Orthogonal Frequency-Division Multiplexing and Pulse-Amplitude Modulation in Indoor Optical Wireless Links," *IEEE Transactions on Communications,* vol. 60, pp. 153-163, 2012.

[47] W. Fang-Ming, L. Chun-Ting, W. Chia-Chien, C. Cheng-Wei, H. Hou-Tzu, and H. Chun-Hung, "1.1-Gb/s White-LED-Based Visible Light Communication Employing Carrier-Less Amplitude and Phase Modulation," *IEEE Photonics Technology Letters,* vol. 24, pp. 1730-1732, 2012.

[48] A. G. Lillie, A. P. Miguelez, A. R. Nix, and J. P. McGeehan, "A comparison of multi-carrier OFDM and single carrier iterative equalisation for future high performance wireless local area networks," in *2002 IEEE 56th Vehicular Technology Conference, 2002. Proceedings. VTC 2002-Fall.*2002, pp. 733-737 vol.2.

[49] M. Crussiere, J. Baudais, and J. F. Helard, "Robust and high-bit rate communications over PLC channels: a bit-loading multi-carrier spread-spectrum solution," in *2005 International Symposium on Power Line Communications and Its Applications,* 2005, pp. 37-41.

[50] T. M. Schmidl and D. C. Cox, "Robust frequency and timing synchronization for OFDM," *IEEE Transactions on Communications,* vol. 45, pp. 1613-1621, 1997.

[51] T. Komine, S. Haruyama, and M. Nakagawa, "Performance evaluation of narrowband OFDM on integrated system of power line communication and visible light wireless communication," in *2006 1st International Symposium on Wireless Pervasive Computing,* 2006, p. 6 pp.

[52] M. Z. Afgani, H. Haas, H. Elgala, and D. A. K. D. Knipp, "Visible light communication using OFDM," in *2nd International Conference on Testbeds and Research Infrastructures for the Development of Networks and Communities, 2006. TRIDENTCOM 2006.*2006, p. 6 pp.

[53] H. Elgala, R. Mesleh, and H. Haas, "Practical considerations for indoor wireless optical system implementation using OFDM," in *10th International Conference on Telecommunications, 2009. ConTEL 2009.*, 2009, pp. 25-29.

[54] J. Armstrong, "OFDM for Optical Communications," *JOURNAL OF LIGHTWAVE TECHNOLOGY,* vol. 27, pp. 189-204, 2009.

[55] J. Vucic, C. Kottke, S. Nerreter, A. Buttner, K. D. Langer, and J. W. Walewski, "White Light Wireless Transmission at 200+ Mb/s Net Data Rate by Use of Discrete-Multitone Modulation," *IEEE Photonics Technology Letters,* vol. 21, pp. 1511-1513, 2009.

[56] S. K. Wilson and J. Armstrong, "Digital Modulation Techniques for Optical Asymmetrically-Clipped OFDM," in *IEEE Wireless Communications and Networking Conference, 2008. WCNC 2008.* 2008, pp. 538-542.

[57] S. Dimitrov, S. Sinanovic, and H. Haas, "Clipping Noise in OFDM-Based Optical Wireless Communication Systems," *IEEE Transactions on Communications,* vol. 60, pp. 1072-1081, 2012.

[58] B. Inan, S. C. J. Lee, S. Randel, I. Neokosmidis, A. M. J. Koonen, and J. W. Walewski, "Impact of LED Nonlinearity on Discrete Multitone Modulation," *IEEE/OSA Journal of Optical Communications and Networking,* vol. 1, pp. 439-451, 2009.
[59] S. Dimitrov and H. Haas, "Optimum Signal Shaping in OFDM-Based Optical Wireless Communication Systems," in *2012 IEEE Vehicular Technology Conference (VTC Fall),* 2012, pp. 1-5.
[60] H. Elgala, R. Mesleh, and H. Haas, "Predistortion in Optical Wireless Transmission Using OFDM," in *Ninth International Conference on Hybrid Intelligent Systems, 2009. HIS '09.*2009, pp. 184-189.
[61] A. M. Khalid, G. Cossu, R. Corsini, P. Choudhury, and E. Ciaramella, "1-Gb/s Transmission Over a Phosphorescent White LED by Using Rate-Adaptive Discrete Multitone Modulation," *IEEE Photonics Journal,* vol. 4, pp. 1465-1473, 2012.
[62] D. Tsonev, H. Chun, S. Rajbhandari, J. McKendry, S. Videv, E. Gu, M. Haji, S. Watson, A. Kelly, G. Faulkner, M. Dawson, H. Haas, and D. O'Brien, "A 3-Gb/s Single-LED OFDM-based Wireless VLC Link Using a Gallium Nitride uLED," *IEEE Photonics Technology Letters,* vol. PP, pp. 1-1, 2014.
[63] A. M. K. G. Cossu, P. Choudhury, R. Corsini, and E. Ciaramella, "3.4 Gbit/s visible optical wireless transmission based on RGB LED," *Optics Express,* vol. 20, pp. B501-B506, 2012.
[64] J. Armstrong and B. J. C. Schmidt, "Comparison of Asymmetrically Clipped Optical OFDM and DC-Biased Optical OFDM in AWGN," *IEEE Communications Letters,* vol. 12, pp. 343-345, 2008.
[65] K. Asadzadeh, A. Dabbo, and S. Hranilovic, "Receiver design for asymmetrically clipped optical OFDM," in *2011 IEEE GLOBECOM Workshops (GC Wkshps),* 2011, pp. 777-781.
[66] D. Tsonev, S. Sinanovic, and H. Haas, "Novel Unipolar Orthogonal Frequency Division Multiplexing (U-OFDM) for Optical Wireless," in *2012 IEEE 75th Vehicular Technology Conference (VTC Spring),* 2012, pp. 1-5.
[67] C. Trout. (2010). *LVX System launches visible light communication in the US, finally*.
[68] T. Saito, S. Haruyama, and M. Nakagawa, "A New Tracking Method using Image Sensor and Photo Diode for Visible Light Road-to-Vehicle Communication," in *10th International Conference on Advanced Communication Technology, 2008. ICACT 2008.*2008, pp. 673-678.
[69] Z. Lubin, D. O'Brien, M. Hoa, G. Faulkner, L. Kyungwoo, J. Daekwang, O. YunJe, and W. Eun Tae, "High data rate multiple input multiple output (MIMO) optical wireless communications using white led lighting," *IEEE Journal on Selected Areas in Communications,* vol. 27, pp. 1654-1662, 2009.
[70] P. W. Wolniansky, G. J. Foschini, G. D. Golden, and R. Valenzuela, "V-BLAST: an architecture for realizing very high data rates over the rich-scattering wireless channel," in *1998 URSI International Symposium on Signals, Systems, and Electronics, 1998. ISSSE 98.*1998, pp. 295-300.
[71] M. E. D. Jafari, H. Najafi, and M. O. Damen, "Adaptive lattice reduction in MIMO systems," in *ISITA 2008. International Symposium on Information Theory and Its Applications, 2008.* 2008, pp. 1-5.

[72] R. Mesleh, H. Elgala, and H. Haas, "Optical Spatial Modulation," *IEEE/OSA Journal of Optical Communications and Networking,* vol. 3, pp. 234-244, 2011.
[73] C. I. C. o. Illumination, "Indoor Illumination Standard," ed: International Organization for Standardization, 2001.
[74] http://www.datasheetarchive.com/BPX-65-datasheet.html.
[75] F. Parand, G. E. Faulkner, and D. C. O'Brien, "Cellular tracked optical wireless demonstration link," *IEE Proceedings Optoelectronics,* vol. 150, pp. 490-6, 17 Oct. 2003.
[76] J. Grubor, S. Randel, K. D. Langer, and J. Walewski, "Bandwidth-efficient indoor optical wireless communications with white light-emitting diodes," in *CNSDSP 2008. 6th International Symposium on Communication Systems, Networks and Digital Signal Processing, 2008.*2008, pp. 165-169.
[77] I. Djokovic, "Cyclic prefix extension in DMT systems," in *Conference Record of the Thirty-Second Asilomar Conference on Signals, Systems & Computers, 1998.*1998, pp. 65-69 vol.1.
[78] I. Neokosmidis, T. Kamalakis, J. W. Walewski, B. Inan, and T. Sphicopoulos, "Impact of Nonlinear LED Transfer Function on Discrete Multitone Modulation: Analytical Approach," *Journal of Lightwave Technology,* vol. 27, pp. 4970-4978, 2009.
[79] Z. Mo, A. B. Awoseyila, and B. G. Evans, "Low complexity time-domain channel estimation for OFDM using training symbols," in *2010 5th Advanced satellite multimedia systems conference (asma) and the 11th signal processing for space communications workshop (spsc),* 2010, pp. 203-207.
[80] B. Ghimire, I. Stefan, H. Elgala, and H. Haas, "Time and frequency synchronisation in optical wireless OFDM networks," in *2011 IEEE 22nd International Symposium on Personal Indoor and Mobile Radio Communications (PIMRC),* 2011, pp. 819-823.
[81] H. Elgala, R. Mesleh, H. Haas, and B. Pricope, "OFDM Visible Light Wireless Communication Based on White LEDs," in *IEEE 65th Vehicular Technology Conference, 2007. VTC2007-Spring.*2007, pp. 2185-2189.
[82] "Forward error correction for high bit-rate DWDM submarine systems," *ITU-T Recommendation G.975.1,* 2004.
[83] B. Nebendahl, W. Freude, C. Koos, J. Leuthold, M. Huebner, R. Schmogrow, A. Josten, D. Hillerkuss, S. Koenig, M. Winter, J. Meyer, and M. Dreschmann, "EVM as new quality metric for optical modulation analysis," in *2013 Saudi International Electronics, Communications and Photonics Conference (SIECPC),* 2013, pp. 1-4.
[84] K. M. Gharaibeh, K. G. Gard, and M. B. Steer, "Accurate estimation of digital communication system metrics - SNR, EVM and ρ in a nonlinear amplifier environment," in *64th ARFTG Microwave Measurements Conference, Fall 2004.* 2004, pp. 41-44.
[85] L. Chen, B. Krongold, and J. Evans, "Theoretical Characterization of Nonlinear Clipping Effects in IM/DD Optical OFDM Systems," *IEEE Transactions on Communications,* vol. 60, pp. 2304-2312, 2012.
[86] D. Tsonev, S. Sinanovic, and H. Haas, "Complete Modeling of Nonlinear Distortion in OFDM-Based Optical Wireless Communication," *Journal of Lightwave Technology,* vol. 31, pp. 3064-3076, 2013.

[87] S. D. Dissanayake and J. Armstrong, "Comparison of ACO-OFDM, DCO-OFDM and ADO-OFDM in IM/DD Systems," *Journal of Lightwave Technology, v*ol. 31, pp. 1063-1072, 2013.

[88] S. D. Dissanayake, K. Panta, and J. Armstrong, "A novel technique to simultaneously transmit ACO-OFDM and DCO-OFDM in IM/DD systems," in *2011 IEEE GLOBECOM Workshops (GC Wkshps),* 2011, pp. 782-786.

[89] S. D. Dissanayake, J. Armstrong, and S. Hranilovic, "Performance analysis of noise cancellation in a diversity combined ACO-OFDM system," in *2012 14th International Conference on Transparent Optical Networks (ICTON),* 2012, pp. 1-4.

[90] N. Fernando, H. Yi, and E. Viterbo, "Flip-OFDM for optical wireless communications," in *2011 IEEE Information Theory Workshop (ITW),* 2011, pp. 5-9.

[91] A. H. Azhar, T. Tuan-Anh, and D. O'Brien, "Demonstration of high-speed data transmission using MIMO-OFDM visible light communications," in *2010 IEEE GLOBECOM Workshops (GC Wkshps),* 2010, pp. 1052-1056.

[92] Z. Shuailong, S. Watson, J. J. D. McKendry, D. Massoubre, A. Cogman, G. Erdan, R. K. Henderson, A. E. Kelly, and M. D. Dawson, "1.5 Gbit/s Multi-Channel Visible Light Communications Using CMOS-Controlled GaN-Based LEDs," *Journal of Lightwave Technology,* vol. 31, pp. 1211-1216, 2013.

[93] E. J. Tacconi and C. F. Christiansen, "A wide range and high speed automatic gain control," in *Proceedings of the 1993Particle Accelerator Conference, 1993.,* , 1993, pp. 2139-2141 vol.3.

[94] Y. Chen, L. Mao, S. Zhang, S. Xie, X. Xiao, Y. Tian, and C. Yang, "An optical receiver with automatic gain control for radio-over-fiber system," in *2011 International Conference of Electron Devices and Solid-State Circuits (EDSSC),* 2011, pp. 1-2.